1ST INTERNATIONAL CONFERENCE ON LWR FUEL PERFORMANCE, MODELLING AND EXPERIMENTAL SUPPORT

LWR
2025

Conference Proceedings

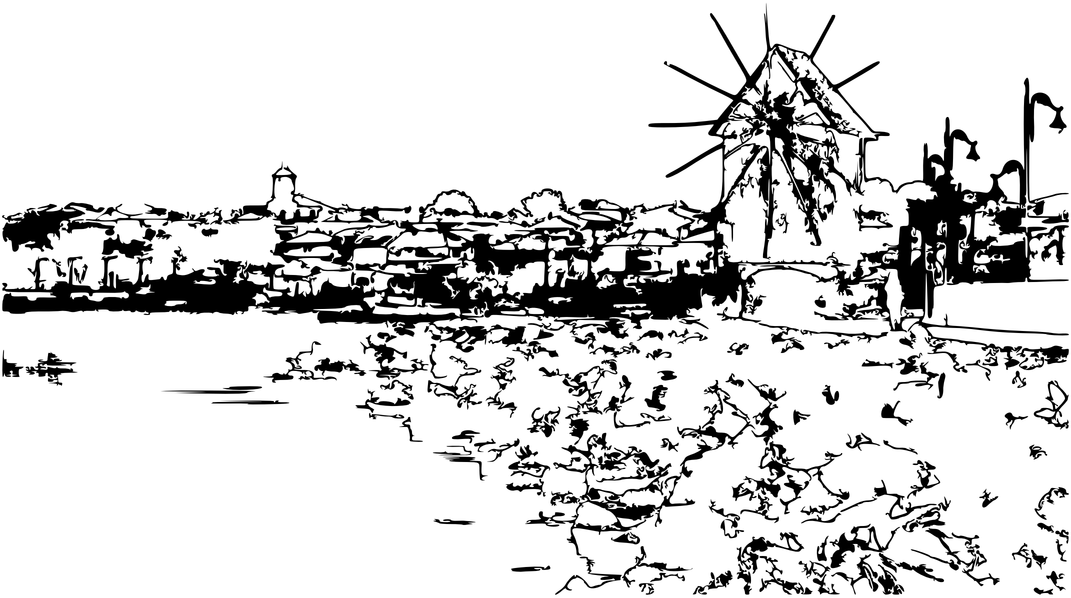

14-19 September 2025, Nessebar, Bulgaria

Proceedings of the 1st International Conference on LWR Fuel Performance, Modelling and Experimental Support

14-19 September 2025, Sol Nessebar Resort, Nessebar, Bulgaria

Published by the Institute for Nuclear Research and Nuclear Energy of the Bulgarian
Academy of Sciences, 72 Tsarigradsko Shosse Blvd., Sofia 1784, Bulgaria

1ST INTERNATIONAL CONFERENCE ON LWR FUEL PERFORMANCE, MODELLING AND EXPERIMENTAL SUPPORT

14-19 SEPTEMBER 2025, SOL NESSEBAR RESORT, NESSEBAR, BULGARIA
Hosted by the Institute for Nuclear Research and Nuclear Energy – BAS

CONTENTS

PREFACE

The present volume contains the submitted scientific contributions to the 1st International Conference on Light Water Reactor (LWR) Fuel Performance, Modelling and Experimental Support.

The meeting was held from 14 to 19 September 2025 at the Sol Nessebar Resort, Nessebar, Bulgaria.

The LWR 2025 conference was organized by the Institute for Nuclear Research and Nuclear Energy of Bulgarian Academy of Sciences.

This scientific forum continuous the legacy of the thirteen WWER Fuel conferences held from 1994 to 2019. More than ninety leading experts from 9 countries representatives of scientific institutes, nuclear power plant operators, nuclear industry companies, nuclear fuel producers, as well as organizations responsible for the development and safety of nuclear technologies and facilities participated the conference. The forum brought together world specialists on nuclear fuel issues - a key element for the operation of any nuclear power plant.

The official opening of the conference took place on 15 September with the participation of Assoc. Prof. Dr. Natalia Kiselova, Chair of the National Assembly of the Republic of Bulgaria; Mr. Lionel Gaiffe, Senior Executive Vice President, Operational Excellence and Fuel Business Unit, Framatome; and Ms. Kristina Ryttersson, Senior Director of Fuel Engineering for the Europe, Middle East and Africa at Westinghouse. Welcome addresses from the Minister of Energy, Mr. Zhecho Stankov, and the Executive Director of Kozloduy NPP, Mr. Ivan Andreev, were delivered on their behalf.

The main topics of the presentations were:

- Fuel performance and operational experience;
- Improvement of fuel design and operation;
- Fuel modelling and experimental support;
- Fuel safety and QA;
- Spent fuel performance and management;
- Specific issues of LWR fuel reliability.

We would like to thank all the participants, members of the advisory and local organizing committees for their contribution to the success of the 1st International Conference on Light Water Reactor Fuel Performance, Modelling and Experimental Support.

Finally, we would like to thank Framatome, Westinghouse, Studsvik, Kozloduy NPP, Bulgarian ministry of science and education for their financial and logistics support.

Dimitar Tonev, Maria Manolova
Chairs of the Organizing Committee
of the **1st International Conference on Light Water Reactor Fuel Performance, Modeling and Experimental Support**

VVER Water Chemistry Compatibility with Westinghouse Fuel

Luis Gonzalez[1*], Mathilde Gaillard[1], Lena Oliver[1] and Britta Helmersson[1]

[1] Westinghouse Electric Sweden, Bränslegatan 1, SE-72163 Västerås

[*]E-mail: luis.gonzalezfonseca@westinghouse.com

Abstract. The coolant chemistry can have a major impact on fuel performance and as such is important to keep within existing guidelines and experience. Significant experience exists for Westinghouse fuel and materials in Pressurized Water Reactors (PWR) but has also gained several operating years in Voda-Vodyanoi Energetichesky Reaktor (VVER) plants. VVERs are based on the same concept as PWRs. However, there are differences and similarities between VVER and PWR fuel operating chemistry conditions that must be evaluated to assess their impact on fuel performance, corrosion, and the risk of crud deposition.

Westinghouse has recently compiled and contrasted the differences between PWR and VVER chemistry control to assure the compatibility with Westinghouse fuels. The behavior of various control parameters in VVER-440 and VVER-1000 units has been compared with Westinghouse and EPRI guidelines in this study. As can be expected, a few minor differences exists in the guidance. Regardless, the data showed that most control parameters have been measured within the range of Westinghouse operational experience for all the plants to which Westinghouse supplies with fuel.

1. Introduction

Westinghouse has been producing nuclear fuel for a wide range of power plants worldwide. More recently, the company has secured 23 contracts with VVER reactors across Europe, with reload deliveries made to 16 of them. Westinghouse fuel has extensive operational experience in Pressurized Water Reactors (PWRs) and is rapidly gaining experience in Voda-Vodyanoi Energetichesky Reaktor (VVER) plants.

These two reactor types share many similarities, both in their thermohydraulic principles and in the fundamental role of coolant chemistry in maintaining fuel performance, minimizing corrosion, and ensuring the long-term safe operation of the plants. However, differences exist in the coolant chemistry strategies and the design of primary and auxiliary systems. For example, one key distinction is the use of potassium hydroxide (KOH) in VVERs, whereas lithium hydroxide (LiOH) is used in PWRs.

Both reactor types feature similar systems for primary water storage tanks, spent fuel pools, and boric acid tanks, allowing for direct comparison between the auxiliary systems supplying source waters. However, each design has sufficient differences that complicate the development of standardized requirements.

In this study, the coolant chemistry conditions have been used to assess the compatibility of VVER-440 and VVER-1000 water chemistry with Westinghouse fuel designs.

2. VVER and PWR coolant chemistry comparison

Coolant chemistry data from reactor vessels and various source waters have been evaluated across multiple VVER units and compared to EPRI [1] and Westinghouse supplemental PWR water chemistry recommendations. A summary of these comparisons is provided in the following sections.

The objective of this evaluation is to assess the water chemistry conditions observed in recent operating cycles and to compare VVER water chemistry guidelines with those of Western PWRs. The openly published Revision 4 of the EPRI PWR Primary Water Chemistry Guidelines [1] is used as a reference. This evaluation primarily focuses on the primary coolant during power operation. Key observations from the guidelines comparison are summarized in Table 1.

Table 1. *Westinghouse/EPRI PWR guidelines for the primary coolant during power operation compared with VVER-440 and VVER-1000 guidelines. Bold values represent control parameters in Westinghouse/EPRI guidelines.*

Parameter	Westinghouse/EPRI	VVER-440[(a)]	VVER-1000[(a)]
Silica, µg/kg	**≤ 3000** [(b)]	<1500	<2000
pH_T	**6.9 – 7.4**	7 - 7,4	7.0 - 7.2
Li, mg/kg	**≤ 3.5**	<1 - <1,5	<1
Hydrogen, cc/kg	**25-50, average ≤ 40**	20 - 60	20 - 50
Oxygen, µg/kg	**< 5**	<5	< 5
Chloride, µg/kg	**≤ 50**	<50 - <100	<50 - <100
Fluoride, µg/kg	**≤ 50**	<50 - <100	<50 - <100
Sulfate, µg/kg	**≤ 50**	<50 - <150	<100 - <200
Al, µg/kg	≤ 50	<50	<50
Mg + Ca, µg/kg	≤ 50	<50	<50
Suspended solids, µg/kg	≤ 50	<50	-
Fe, µg/kg	-	<50	<50
NH_3, mg/kg	-	3 - 35	5 - 16
NO_3, µg/kg	-	<100	<200
TOC, mg/kg	-	<500	<50 - <500

[a] Some of the power plants might not have a limit for these parameters.

[b] The plants should aim to limit silica to <1000 µg/kg.

2.1 Alkalinity control

Boric acid is used in nuclear reactors to control core reactivity. However, its addition lowers the pH of the coolant. To maintain the desired pH level, an alkaline solution, such as lithium hydroxide (LiOH) or potassium hydroxide (KOH), must also be added. Initial assessments in PWRs indicated that lithium borates could present solubility issues and potentially precipitate in the crud, although they could still be used if lithium concentrations were kept low. Potassium hydroxide was initially rejected, not due to concerns about fuel cladding, but because it was believed to contribute to excessive residual radioactivity. However, operational experience from VVERs has shown that potassium hydroxide does not lead to problematic radioactivity buildup [2].

In VVER reactors, three alkali metals, potassium (K), lithium (Li), and sodium (Na), are used to control the pH of the primary coolant. Their combined concentration is expressed as "equivalent potassium concentration," denoted as K_{tot} or K_{eqv}, and measured in mg/L or mg/kg. This value represents the sum of the concentrations of K^+, Li^+, and Na^+ during power operation. In contrast, PWRs rely solely on lithium hydroxide to maintain alkalinity and pH at operating temperatures.

K_{tot} values will depend on the concentration of boric acid, and therefore limits are not constant. As illustrated in Figure 1, different operational zones are defined. K_{tot} should be maintained within the optimal range (Zone A) during power operation, and any measurements outside this zone should prompt corrective actions. The maximum equivalent lithium concentration that could be measured in a VVER is 3.8 mg/kg, which is slightly higher than the Westinghouse/EPRI limit of 3.5 mg/kg. Most measurements in VVERs have remained well below this threshold, indicating compliance with Westinghouse requirements.

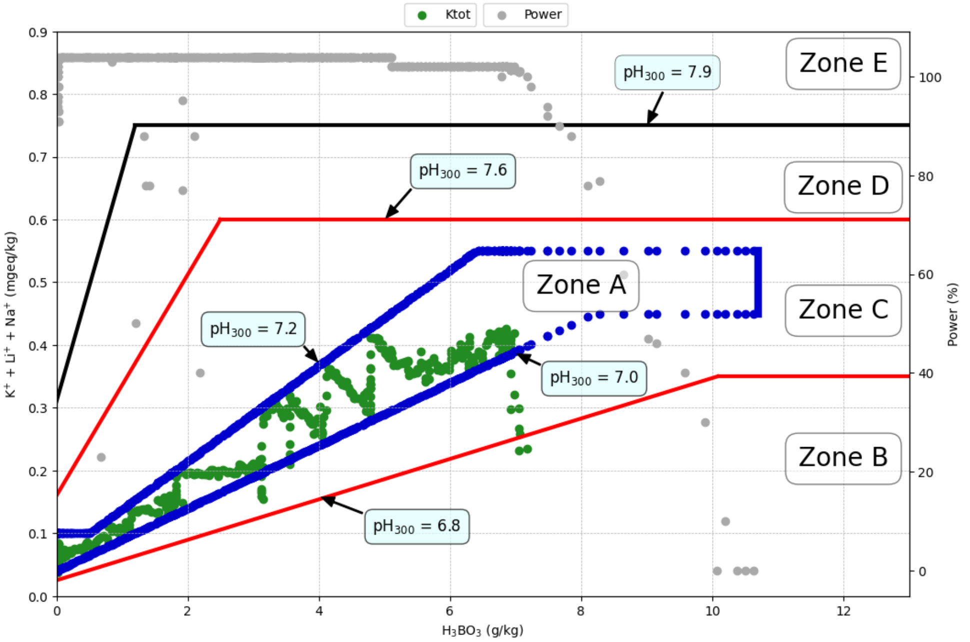

Figure 1. Example of alkalinity control K_{tot} as the sum of K^++Li^++Na^+ (mmol/kg) versus boric acid concentration H_3BO_3 (g/kg) for a VVER-1000, together with the K_{tot} optimal area (Zone A) and action levels areas (Zones B, C, D, E) during power operation.

2.2 Hydrogen source

Maintaining an appropriate hydrogen concentration in the primary coolant is essential to suppress the radiolytic production of oxygen and to mitigate the risk of accelerated corrosion. Based on Westinghouse operating experience in PWRs, a minimum hydrogen concentration of 25 cc/kg is required to prevent an increase in the Primary Water Stress Corrosion Cracking growth rate in nickel-based fuel materials. However, a level of just 5 cc/kg is needed to maintain reducing conditions in the fuel assembly [1]. The upper limit of 50 cc/kg is intended to avoid the formation of brittle hydrides in zirconium-based alloys.

Hydrogen limits in VVERs are generally similar to those required by EPRI and Westinghouse, although the acceptable range is broader, typically from 20 to 60 cc/kg. Measurements from VVERs have mostly fallen within the lower end of this range but remain consistent with Westinghouse experience (see Figure 2).

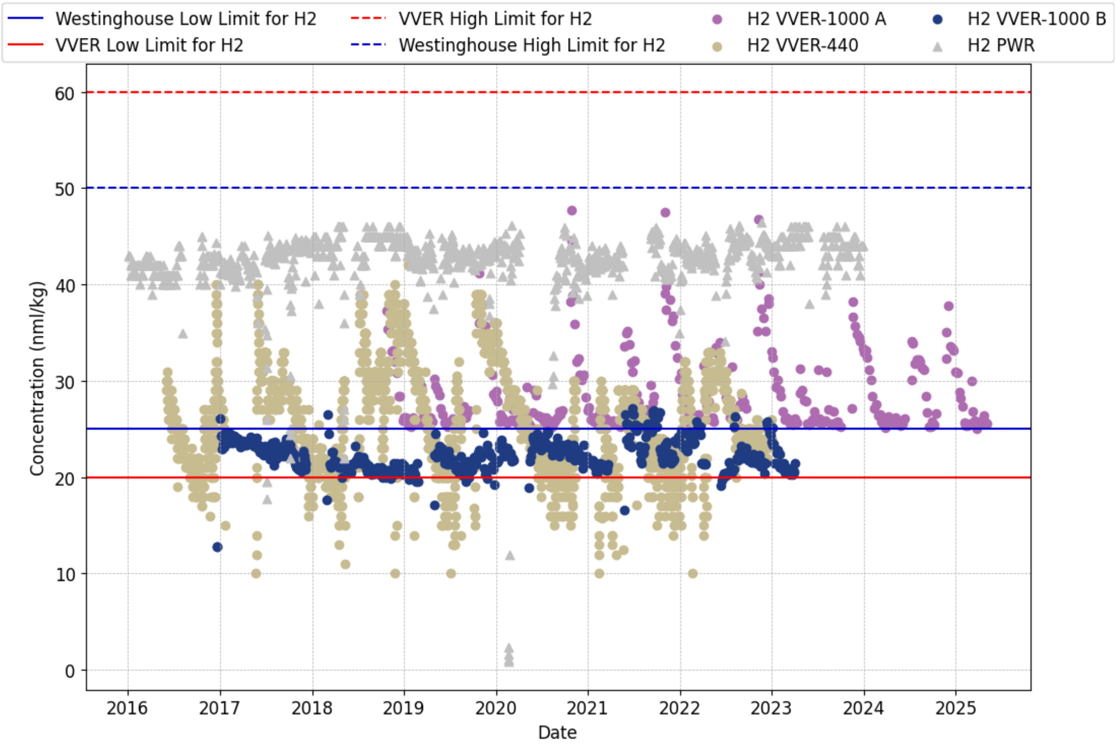

Figure 2. Hydrogen concentration in VVERs coolant, with Westinghouse and VVERs required minimum and maximum hydrogen limits during power operation.

In PWRs, dissolved hydrogen is directly injected to maintain reducing conditions, which suppress radiolysis and reduce dissolved oxygen concentrations through radiation-induced reactions. In contrast, VVERs typically generate hydrogen indirectly through the radiolysis of ammonia during power operation. This method effectively maintains the required hydrogen concentration. Additionally, some VVERs are equipped to inject hydrazine into the coolant to manage oxygen transients when necessary.

2.3 Anions

Chloride and sulfate species are known to increase the risk of stress corrosion cracking (SCC) in stainless steel and certain nickel-based alloys. Fluorides can also accelerate corrosion in zirconium-based alloys. For this reason, chloride (Cl^-), fluoride (F^-), and sulfate (SO_4^{2-}) are considered control parameters by Westinghouse when evaluating fuel performance and water chemistry compatibility.

Westinghouse/EPRI guidelines specify a maximum concentration of 50 µg/kg for each of these anions in the primary coolant during power operation. VVER guidelines are generally similar, although in some cases they allow slightly higher limits. Unlike Westinghouse, VVERs may classify these anions as either control or diagnostic parameters, depending on the plant.

Recent measurements during normal operation in VVERs have shown consistently low levels of these anions (see Figure 3). As long as concentrations remain below the maximum limits specified by Westinghouse, no adverse effects are expected. The stable and low levels of sulfate and fluoride also suggest that the ion exchange resins are functioning effectively and are not being degraded by ammonia or other chemical additions.

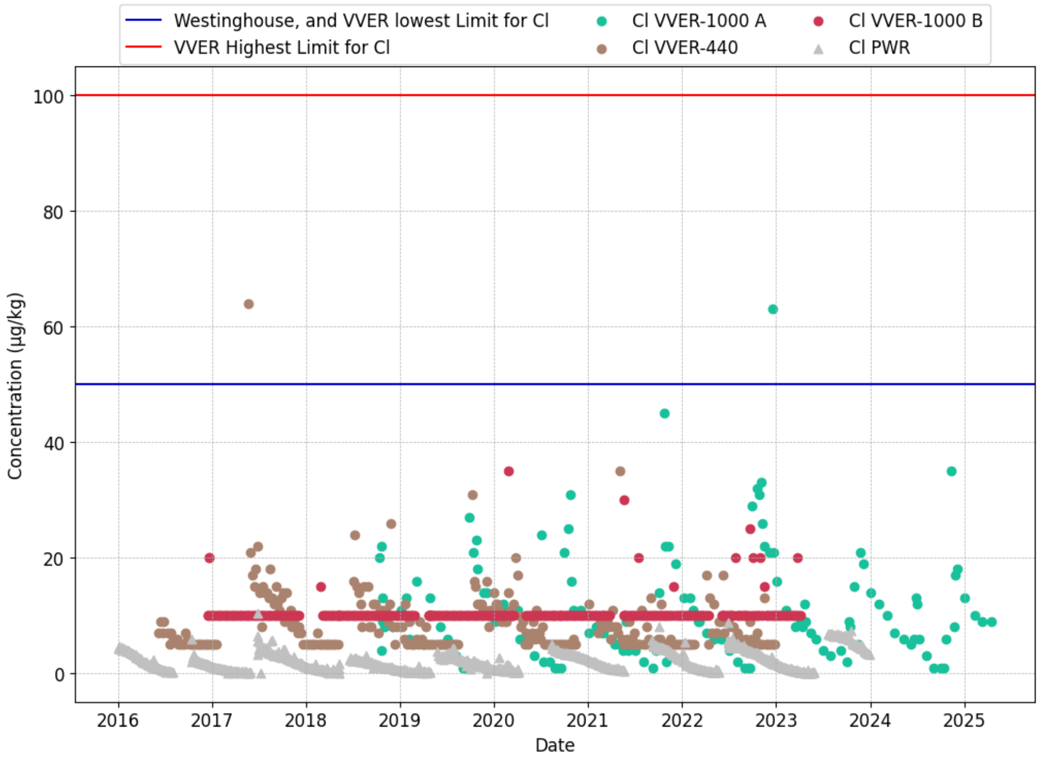

Figure 3. Chloride concentration in VVERs coolant, with Westinghouse and VVERs required chloride limits during power operation. The two limits for VVER indicate the range between different VVER power plants.

2.4 Silica and zeolite forming cations

Silica and zeolite-forming cations, namely aluminum (Al), calcium (Ca), and magnesium (Mg), are considered important control and diagnostic parameters by Westinghouse. Elevated concentrations of these species can contribute to the densification of fuel crud, which reduces thermal conductivity and can negatively impact fuel performance.

In contrast, these parameters are generally not prioritized in VVERs. In most cases, they are either not measured or not assigned specific limits within the various systems. This difference in monitoring practices highlights a key area where VVER chemistry control diverges from Western PWR guidelines. In fact, some crud measurements done in a VVER-440 has shown the presence of silica and calcium in crud particles seen during visual inspection [3]. Regardless, crud is rarely seen in significant amount in VVERs during inspections and, together with mostly low levels of cations measured (Figures 4 and 5), the fuel continues to perform well.

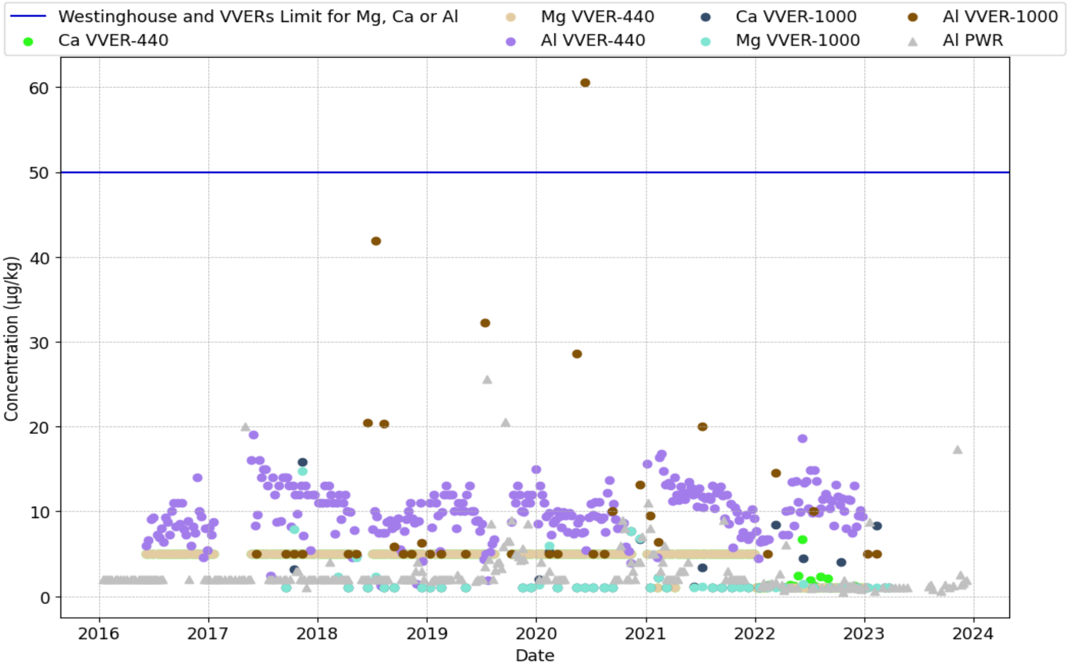

Figure 4. Magnesium, aluminium and calcium concentration in VVERs coolant, with Westinghouse required limits during power operation and VVERs limits for some power plants. The flatness in the Mg data is due to measurements mostly below the limit of detection.

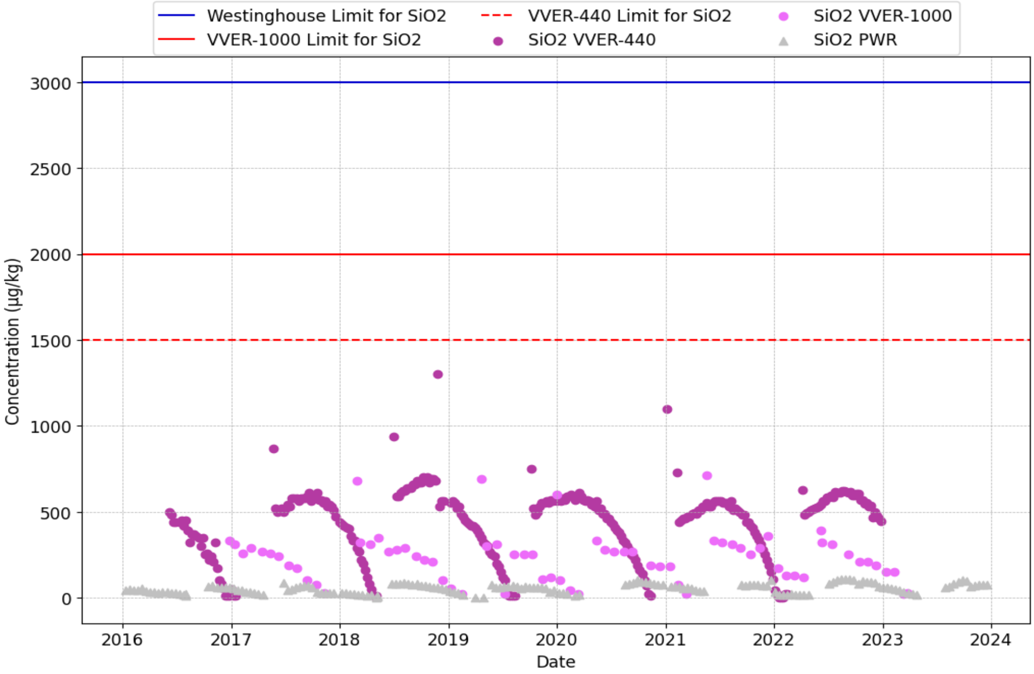

Figure 5. Silica concentration in VVERs coolant, with Westinghouse required limits during power operation and VVERs limits for some power plants.

2.5 Other parameters

In addition to the control parameters discussed earlier, VVER plants monitor several other diagnostic parameters, including iron, ammonia, nitrates, and total organic carbon (TOC). While these are not considered control or diagnostic parameters by Westinghouse, elevated levels of these substances can still pose risks to fuel performance.

Iron, for example, can contribute to the formation of crud deposits on fuel surfaces. Ammonia and nitrates, if present in excess, may affect the efficiency of ion exchange systems and lead to undesirable chemical interactions. TOC levels are also monitored to ensure that organic contaminants do not interfere with coolant chemistry or fuel integrity. Figure 6 present the iron concentration in the coolant in VVERs, and as can be seen, the levels are maintained below the limits recommended by the VVER guidelines.

Despite the differences in classification, the limits set by VVER guidelines for these parameters are generally respected during power operation, helping to maintain stable and safe operating conditions.

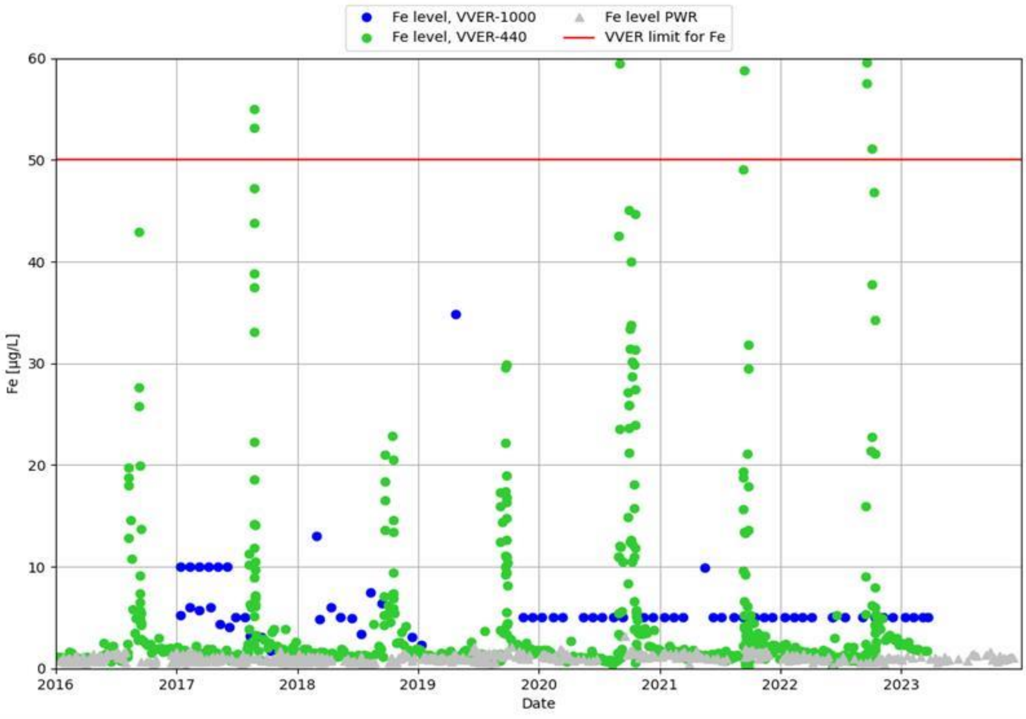

Figure 6. Iron level in the primary coolant of one VVER-1000, one VVER-440 and two PWR reactors

2.6 Steam generators

Steam generators play a significant role in influencing the water chemistry of the primary coolant. Corrosion within these systems can lead to elevated concentrations of metallic elements and activated corrosion products in the coolant.

In VVER reactors, steam generators are constructed using stainless steel materials, whereas PWRs typically use nickel-based alloys. This difference in material composition affects the types and levels of corrosion products observed. For example, PWRs tend to exhibit higher activity levels of cobalt-58 (Co-58), which originates from nickel-based materials. In contrast, the primary activated corrosion product from stainless steel, cobalt-60 (Co-60), is found at similar or lower levels in VVERs. In Figures 7 and 8 a comparison of the levels of Co-58 and Co-60 measured for different PWRs and VVERs can be seen.

Understanding these material differences is essential for interpreting coolant chemistry data and assessing the impact on fuel performance and radiation fields.

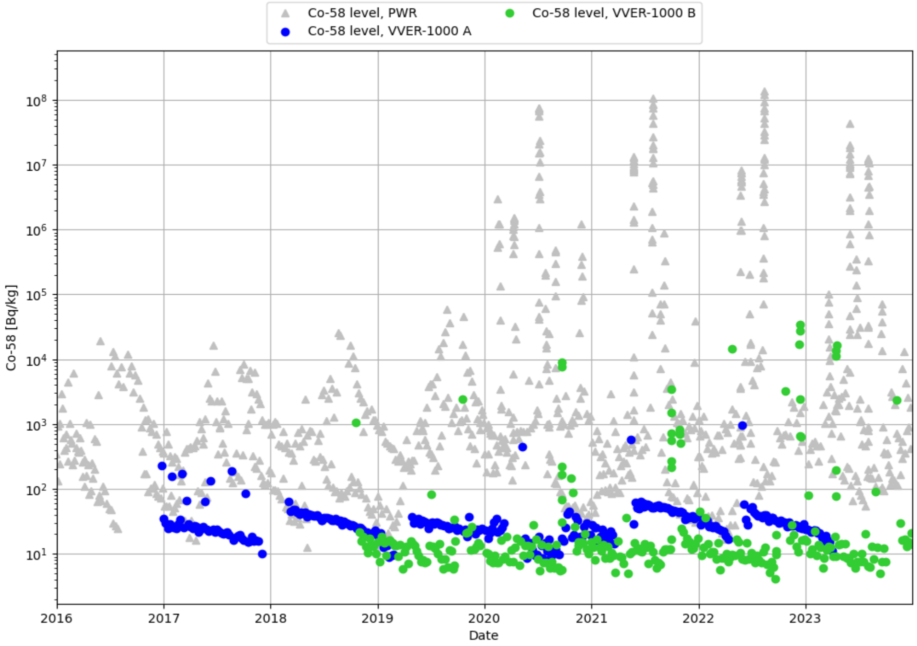

Figure 7. Co-58 level in the primary coolant of two VVER-1000 and two PWR reactors

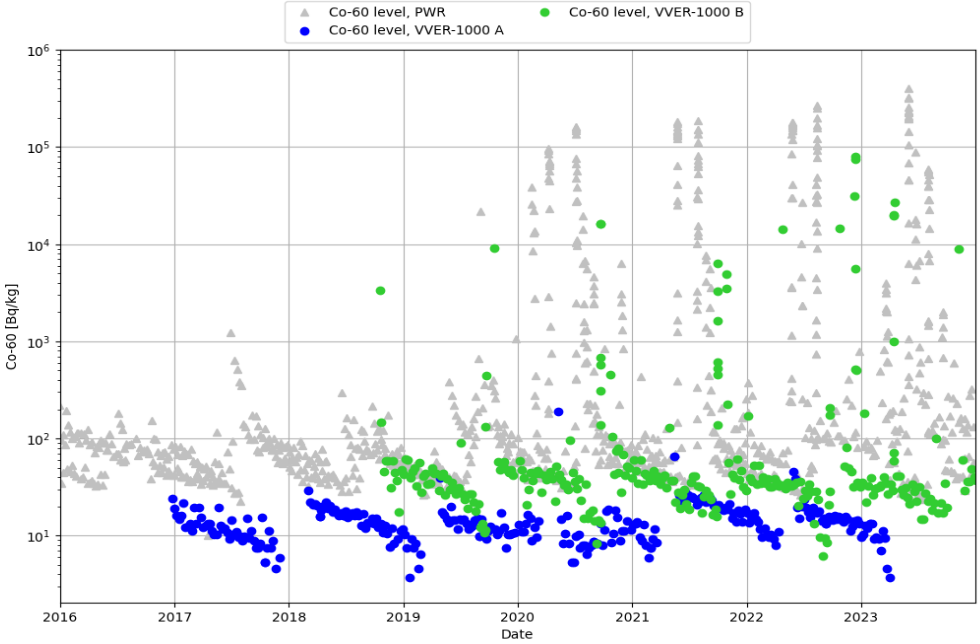

Figure 8. Co-60 level in the primary coolant of two VVER-1000 and two PWR reactors

3. Conclusions

The evaluation of water chemistry in VVER-440 and VVER-1000 reactors, along with a comparison of internal VVER guidelines against EPRI PWR and Westinghouse supplemental water chemistry recommendations, indicates that most parameters fall within the operating ranges used in Western PWRs.

Although hydrogen concentrations have been measured at or below the limits required by Westinghouse, the levels are sufficient to reduce the radiolytic decomposition of water and are therefore considered acceptable by Westinghouse.

As long as chemistry conditions are maintained within these established ranges, no adverse impact on fuel performance is expected. The analysis confirms that Westinghouse fuel is compatible with the coolant chemistry of both VVER-440 and VVER-1000 reactors.

Acknowledgements

We would like to express our sincere gratitude to our VVER customers for their continued support, collaboration, and trust throughout the course of this work.

References

[1] PWR Primary Water Chemistry Guidelines: Volume 1, Revision 4, EPRI, Palo Alto, CA: 1999. TR-105714-V1R4.

[2] L. Oliver, B. Helmersson, R. De Vito. Westinghouse VVER Fuel Experience And Fuel Qualification Need For Introducing KOH In Pressurized Water Reactors. NPC 2018.

[3] S. EL JAMAL, S. BUDDAS, L. JAVANAINEN, L. OLIVER, B. HELMERSSON, R. DEVITO. COMPARISON BETWEEN LOVIISA VVER-440 AND PWR OPERATING EXPERIENCE. TO BE PRESENTED IN THE INTERNATIONAL CONFERENCE ON WATER CHEMISTRY AND NUCLEAR REACTOR SYSTEMS, NPC. SEPTEMBER 22-26, 2025.

The POLCA8H Nodal Code for VVER-1000

Antonios Mylonakis[*], **Carl Adamsson and Sten-Örjan Lindahl**

Westinghouse Electric Sweden AB
721 63 Västerås, Sweden

[*]E-mail: *antonios.mylonakis@westinghouse.com*

Abstract. Westinghouse Electric Sweden introduces POLCA8H 1.0, a new nodal code for VVER-1000 reactors, with planned extension to VVER-440 cores. The code solves the neutron diffusion equation in hexagonal geometry using the Fourier expansion method. Each hexagonal assembly is modelled either as one column of hexagonal nodes or as six columns of triangular nodes. For treating axial heterogeneities, on-the-fly axial homogenization is performed. The cross-section representation model accounts for all significant physical phenomena influencing reactor behavior. A coupled thermal-hydraulics module computes the coolant density and temperature distributions for each assembly by solving the conservation equations for mass, momentum, and energy. The distribution of coolant in the core is estimated in an iterative manner from the requirement that the pressure drop over all channels must be equal in a core steady state. Pin power reconstruction is carried out using the conventional two-step approach, where the nodal flux solution is combined with precomputed pin power form factors obtained from lattice physics calculations. The code is implemented in modern Fortran and parallelized using OpenMP to ensure computational efficiency on shared-memory architectures. POLCA8H is intended to be used for steady-state core design and related licensing applications as well as for the class of safety calculations that can be performed with steady-state methods. Selected initial V&V results are presented, providing evidence of satisfactory accuracy and performance in representative reactor physics applications.

1. Introduction

POLCA8H is a three-dimensional code for simulating the neutronic, thermal, and hydraulic behaviour of a VVER reactor core. The code solves the coupled neutronic and thermal-hydraulic equations. POLCA8H is intended to be used for all VVER steady-state core design and related licensing applications. POLCA8H is also used to prepare input and initialize dynamic AOO and accident analyses.

The neutronic module of POLCA8H solves the two-group diffusion equation using the Fourier expansion method for a core made up of either hexagonal prisms or triangular ones with hexagons broken up into equilateral triangles. The code calculates the three-dimensional (3D) power distribution in the reactor core. The reactor core, including parts of the axial and radial reflector regions, is divided into computational nodes to which homogenized equivalent two-group macroscopic cross sections are assigned. The computation of the 3D power distribution includes the thermal-hydraulic feedback, the influence of control rods, as well as important reactivity feedback effects such as those due to fuel temperature and xenon absorption. POLCA8H can model sixth, third and full core symmetries.

The thermal-hydraulics module considers each vertical nodal array as a channel where the principles of mass, energy, and momentum conservation are applied. Separate loss coefficients can be provided for important assembly components such as inlet orifices, bottom nozzles, tie plates and spacers.Geometric axial variations in the fuel assemblies can be treated.

Co-funded by the European Union

Funded by the European Union. Views and opinions expressed are however those of the author(s) only and do not necessarily reflect those of the European Union or Euroatom. Neither the European Union nor the granting authority can be held responsible for them

APIS

POLCA8H tracks the important nuclides by solving the nuclide transmutation equations assuming linear nuclide chains. The equations are integrated in time using the predictor-corrector technique.

Pin powers, linear and average planar heat generation rates are calculated by the pin power reconstruction module. The module superimposes fuel assembly internal rod power distributions provided by a lattice code such as PHOENIX5 on the nodal powers predicted by the POLCA8H flux solver.

In Section 2, an overview of the main models of the code is provided. Section 3 presents some indicative validation results.

2. Main models

2.1 Neutronics

The multi-group diffusion equation for group $g, g = 1, \dots, NG$, is

$$D_g \nabla^2 \phi_g - \left(\Sigma_{ag} + \Sigma_{rg}\right)\phi_g + \sum_{\substack{h=1 \\ h \neq g}}^{NG} \Sigma_{sgh}\phi_h + \frac{\chi_g}{k_{eff}} \sum_{h=1}^{NG} \Sigma_{fh}\phi_h = 0 \tag{1}$$

where notation is conventional. In matrix formulation, Eq. 1 becomes

$$\widehat{D} \nabla^2 \vec{\phi} + \widehat{\Sigma}^{xs} \vec{\phi} = 0 \tag{2}$$

The cross sections can vary spatially within each node around their mean value $\bar{\Sigma}_{gh}$ leading to:

$$\Sigma_{gh}^{xs}(r) = \bar{\Sigma}_{gh} + \Delta\Sigma_{gh}(r), \qquad g, h = 1, \dots, N \tag{3}$$

This intra-nodal variation is due to deviations in burnup, moderator density, fuel temperature, xenon, and heavy nuclides from the values assumed by the lattice code model.

The homogenized average cross section matrix for any node is given by:

$$\left.\begin{aligned} \tilde{\Sigma}_{gh} &= \bar{\Sigma}_{gh} + \Delta\tilde{\Sigma}_{gh} \\ \Delta\tilde{\Sigma}_{gh} &= \frac{\int \Delta\Sigma_{gh}(r) \cdot \phi_h(r) dV}{\int \phi_h(r) dV} \end{aligned}\right\} \tag{4}$$

Eq. 2 may be written as:

$$\widehat{D} \nabla^2 \vec{\phi}(r) + \tilde{\Sigma} \vec{\phi}(r) = -\vec{S}^{xs} \tag{5}$$

where $\tilde{\Sigma}$ is the matrix containing $\tilde{\Sigma}_{gh}$. The non-uniformities of the node are formally accounted by the following source term:

$$\vec{S}^{xs}(r) = \left(\Delta\widehat{\Sigma}(r) - \Delta\tilde{\Sigma}\right) \cdot \vec{\phi}(r) \tag{6}$$

where the matrix $\Delta\widehat{\Sigma}(r)$ is composed by the variations $\Delta\Sigma_{gh}(r)$. The integral of $\vec{S}^{xs}(r)$ over the node volume equals zero, because of the definition of matrix $\tilde{\Sigma}$.

Eq. 5 can be rewritten in the following way:

$$\nabla^2 \vec{\phi} + \widehat{B}^2 \vec{\phi} = -\widehat{D}^{-1} \vec{S}^{xs}(r) \quad , \quad \widehat{B}^2 = \widehat{D}^{-1} \tilde{\Sigma} \tag{7}$$

where $\widehat{B}^2$ is the buckling matrix.

The eigenvectors of the eigenvalue equation $\hat{B}^2\vec{U}_g = B^2\vec{U}_g$ make up a matrix $\hat{U} = [\vec{U}_1, \vec{U}_2, \ldots, \vec{U}_{NG}]$. In two energy groups, the eigenvalues of the matrix will always be real (if no up-scattering is allowed). Otherwise, complex eigenvalues may appear. By multiplying Eq. 7 by $\hat{U}^{-1}$, the multi-group diffusion equation is decomposed into NG non-homogeneous 'one-group' wave equations. Moreover, if the dimensionless coordinates are used

$$\xi = \frac{2x}{h_x} \quad , \quad \eta = \frac{2y}{h_x} \quad , \quad \zeta = \frac{2z}{h_z}$$

with h_x being the base width of any of the six triangles making up the hexagon and h_z the node height, the following set of 'one-group' equations appear

$$\frac{\partial^2\psi_g}{\partial\xi^2} + \frac{\partial^2\psi_g}{\partial\eta^2} + \frac{1}{R^2}\frac{\partial^2\psi_g}{\partial\zeta^2} + b_g^2\psi_g(r) = -q_g^{xs}(r) \qquad , g=1, \ldots, NG \tag{8}$$

In Eq. 8 the following set of new quantities have been introduced:

$$\vec{\psi}(r) = \hat{U}^{-1}\vec{\phi}(r) \tag{9}$$

$$b_g^2 = \frac{1}{4}h_x^2 B_g^2 \quad , \quad R = \frac{h_z}{h_x}$$

$$\vec{q} = \frac{1}{4}h_x^2\hat{U}^{-1}\hat{D}^{-1}\vec{S}^{xs}(r) \tag{10}$$

The modal flux ψ_g has no direct physical interpretation and may be complex. The physical flux is always positive and continuous over node boundaries while the modal one may be negative and discontinuous. Employing Eq. 9, one may freely move back and forth between the physical flux Φ_g and the modal flux ψ_g. Eqs 8 are solved as described in [1].

2.2. Cross section model

POLCA8H currently applies a two energy group structure with two group constants together with an effective removal cross section (Σ_r) defined as $\Sigma_r = \Sigma_{s,2\leftarrow 1} - \Sigma_{s,1\leftarrow 2}\frac{\Phi_2}{\Phi_1}$ where Σ_s is the scattering macroscopic cross section.

The main function of the cross-section module of POLCA8H is to supply the flux solver with macroscopic two-group, node average cross sections and neutron diffusion coefficients ($D_g, \Sigma_r, \Sigma_{ag}, \Sigma_{fg}, \nu\Sigma_{fg}, \kappa\Sigma_{fg}$, g = 1,2). The symbols in the parenthesis stand for the diffusion coefficient and the removal, absorption, fission, nu-fission and kappa-fission macroscopic cross sections respectively. A macroscopic cross section/diffusion coefficient is reconstructed as a sum of a feedback-free or "base" term and several feedback correction terms. The model for macroscopic cross sections takes the following form:

$$\begin{aligned} \Sigma \;=\; & \Sigma^{base}(E, \rho_h, \rho) \quad + \quad \Delta\Sigma^{SG} + \Delta\Sigma^{CR} \\ & + \; \Delta\Sigma^{BHI}(E, \rho, B_h) \\ & + \; \Delta\Sigma^{DBA} \\ & + \; b_{B1}\left[C_B - C_B^{base}\right] + b_{B2}\left[C_B - C_B^{base}\right]^2 \\ & + \; c_{Xe}\left[N_{Xe} - N_{Xe}^{base}(E, \rho_h, w_{CBH})\right] \end{aligned}$$

$$\begin{aligned} &+ \quad d_{Dop}\left[\sqrt{T_f} - \sqrt{T_f^{base}}\right] \\ &+ \quad c_{T_m}[T_m - T_m^{base}] \\ &+ \sum_i \sigma_i\left[N_i - N_i^{base}(E, \rho_h, B_h, w_{CBH}, DBA)\right] \\ &+ \quad w_{CBH}\left[(1 - \delta_{CR})\Delta\Sigma^{CBH,out} + \delta_{CR}\Delta\Sigma^{CBH,in}\right] \\ &+ \quad \Delta\Sigma^{spat} \end{aligned} \qquad (11)$$

The base cross sections, $\Sigma^{base}$are computed by a lattice code such as PHOENIX5 at “base conditions”. A base condition is defined as an exposure state (E) with a given instantaneous coolant density (ρ) for a depletion case with a given coolant density history (ρ_h), absence of control rods, no spacer grids, detectors and reference fuel temperature (T_f^{base}), moderator temperature (T_m^{base}) and power density (yielding a reference xenon equilibrium concentration N_{Xe}^{base}). The base cross sections are calculated for a reference boron concentration.

2.2.1. Control rod and spacer grid

The instantaneous impact on the nodal cross sections by the presence of control rods, spacer grids and detector is modelled via the following dedicated terms, $\Delta\Sigma^{CR}$, $\Delta\Sigma^{SG}$. Both terms are calculated by respectively postprocessing branch calculations performed with the lattice code.

2.2.2. Boron, control rod and discrete burnable absorber history

The history effect for depleting at a different boron concentration is captured by the term $\Delta\Sigma^{BHI}$ of Eq. 11. Additionally, the instantaneous variation in boron concentration C_B is modelled with the expression $b_{B1}\left[C_B - C_B^{base}\right] + b_{B2}\left[C_B - C_B^{base}\right]^2$ where b are sensitivity coefficients provided by the lattice physics code.

Since both the isotope history and intra-nodal cross section models are designed for only mild spatial and spectral history effects, they cannot fully capture the strong impact of Control Rod History (CRH) on nodal cross sections. For this purpose, the CRH history effects are modelled separately via the term $w_{CRH}\left[(1 - \delta_{CR})\Delta\Sigma^{CRH,out} + \delta_{CR}\Delta\Sigma^{CRH,in}\right]$ with δ_{CR} representing an un-rodded ($\delta_{CR} = 0$) or rodded state ($\delta_{CR} = 1$) and w_{CBH} being the control rod history. Briefly, this model interpolates between the two extreme cases, namely, the case with the control rods always inserted during depletion and the case with the control rods never inserted. The ΔΣ terms needed by this model are calculated by the lattice code.

Discrete burnable absorber rods may be inserted in some of the fuel assemblies during the first cycle of operation and then removed during the cycle outage. The impact of discrete burnable absorbers in depletion history is modelled via the term $\Delta\Sigma^{DBA}$. This term is computed with the lattice code by combining the cross sections generated from a depletion calculation where discrete burnable absorbers are inserted at the initial depletion period and then removed with the cross sections generated with no discrete burnable absorbers initially inserted.

2.2.3. Fuel and moderator temperatures

A deviation in fuel temperature T_f is handled with the term $d_{Dop}\left[\sqrt{T_f} - \sqrt{T_f^{base}}\right]$ where d_{Dop} coefficients are included in the data provided by the lattice code. The effect of varying moderator temperature on cross sections is modelled with the expression $c_{T_m}[T_m - T_m^{base}]$ where c_{T_m} are coefficients also obtained with the lattice code.

2.2.4. Fuel depletion

Fuel depletion at off-base conditions results in an isotope inventory (N_i) that differs from the one obtained at reference conditions. POLCA8H handles this by explicitly tracking all important nuclides (i) and correcting for the isotopic deviations through the summation term:

$$\sum \sigma_i \left(N_i - N_i^{base}(E, \rho_h, B_h, w_{CBH}, DBA) \right),$$

where w_{CRH} and DBA stand for the control rod and discrete burnable absorber histories.

The deviation of the xenon concentration from the one at base conditions is modelled separately via the term $c_{Xe}\left[N_{Xe} - N_{Xe}^{base}(E, \rho_h, w_{CBH})\right]$ where c_{Xe} is the xenon sensitivity coefficient estimated with lattice calculations.

2.2.5. Intranodal variation of cross sections

Burnup induced intra-nodal effects are accounted via a spatial variation correction term ($\Delta\Sigma^{spat}$) which is computed internally by POLCA8H. More specifically, the spatial intra-nodal cross section deviation $\Delta\Sigma(r)$ is assumed to be given by a radially non-separable quadratic Legendre polynomial expansion. The coefficients of the Legendre expansion are calculated using the deviation of properties, e.g. burnup, coolant density, at nodal sides and nodal vertical edges from their nodal average values. By spatially homogenizing $\Delta\Sigma(r)$ in a node, the correction term $\Delta\Sigma^{spat}$ is obtained. This term is then used in the solution of the modified diffusion equation solved by POLCA8H, see Section 2.1.

2.3. Axial Homogenization

Axial heterogeneities appear inside the nodes due to presence of spacers, control rods, enrichment zoning etc. POLCA8H includes a method to handle such heterogeneities via on-the-fly axial homogenization calculations.

The module of axial homogenization uses the concept of axial sub-nodes to model all the axial heterogeneities of each fuel assembly. Then it solves the one-dimensional (1D) diffusion equation for each assembly in the axial direction with sub-nodal resolution. This calculation generates flux weights that are used to homogenize and transfer the cross sections from the sub-nodal to the nodal level that is used by the 3D flux solver. Axial discontinuity factors are also calculated and provided to the 3D flux solver.

Moreover, the module uses the detailed 1D axial power distribution computed for each channel in the sub-node level to calculate axial form factors. With the aid of those, the pin power model described in Section 2.4 accounts for axial heterogeneities.

Since the 3D flux distribution affects parameters which can impact the 1D axial calculations (e.g., nodal powers, nodal exposures, coolant densities, radial leakages, etc.), an iterative process is employed with the purpose to obtain a converged solution. Consequently, POLCA8H generates consistent 3D nodal and 1D local fluxes in each assembly.

2.4. Pin power reconstruction

The knowledge of the power distribution at the pin and pellet level constitutes the basis for the calculation of several secondary quantities like peaking factors, pin burnup, pin linear heat generation rate and thermal margins.

Since the POLCA8H flux solver is a coarse mesh method with a primary function to compute nodal powers, the calculation of pin and pellet powers is performed in a post-processing stage where POLCA8H superimposes pin power form factors supplied by the lattice code on the smoothly varying homogeneous power distribution inside each sub-node. As a result, a power distribution at the pellet level is obtained.

More specifically, POLCA8H computes the local (i.e., pellet level) power distribution as following:

$$p(x,y,z) \quad = \quad c^{norm} \sum_{g=1}^{2} S_g^{rad}(x,y) \cdot S_g^{ax}(z) \cdot P_g^{hom}(x,y,z), \tag{12}$$

where c^{norm} is a normalization factor. The term $S_g^{rad}(x,y)$ is the radial fine structure shape function (one value per fuel rod at a given axial height) carried over from the lattice calculation. This function accounts for the heterogeneous nature of relative rod power distribution due to effects such as individual pin enrichments and the local effects of control rods. The shape function is parameterized with dependence on fuel segment type, exposure node burnup, instantaneous coolant density, coolant density history, control rod presence of various control rod types, discrete burnable absorber correction, and control rod history.

The term $S_g^{ax}(z)$ is the axial fine structure shape function that is represented by a set of axial form factors. These factors are calculated internally by the axial homogenization module of POLCA8H as mentioned in Section 2.3.

The last term, $P_g^{hom}(x,y,z)$, is the “homogeneous” power distribution inside a node obtained by solving the two-group diffusion equation with realistic boundary conditions and with slowly varying cross sections. This term accounts for global, smooth power variations from such effects as the uneven leakage of neutrons from neighbouring nodes and by the fact that the assemblies are depleted in a different environment in the reactor than assumed in lattice physics calculations.

Using the pin power distribution computed by Eq. 12, the thermal or heated pin power distribution is subsequently calculated accounting for:

- the fraction of the fission power that is radiated out of the pin through gamma and (fast) neutron transport and absorbed in the surrounding coolant and construction material.
- the fraction of the fission power that is radiated out of the pin and subsequently deposited in the fuel pins (pellet and cladding) of the assembly including the pin of radiation origin (gamma smearing effect).

2.5. Fuel depletion and nuclide concentration tracking

All types of burnup calculations are performed in a geometry built up of so-called exposure nodes. An exposure node is characterized by being homogeneous in the axial direction except for any control rod discontinuities in the node (partial presence). The default technique for depletion calculations is the Predictor-Corrector method.

In POLCA8H, the evolution of nuclide concentrations is modelled explicitly for a selected set of heavy nuclides and fission products that significantly influence core reactivity and isotopic inventory. More specifically, the model for the transmutation of nuclides with time constants of order of days, includes both production and destruction mechanisms. More specifically, a nuclide is produced through one or a combination of three mechanisms:

- direct fission
- decay of the predecessor nuclide
- conversion

A nuclide may disappear through:

- decay
- neutron absorption

POLCA8H simplifies the depletion equations by linearizing the decay and conversion chains. More specifically, a complicated chain is decomposed into a number of linear chains for each of the non-fission source terms described by separate equations. This allows each of the linearized equations to be solved separately. The net result for a nuclide is obtained by adding the contributions from the various linear chains. The time integration of the governing equations for nuclide number density is performed via the predictor-corrector method.

2.6. Thermal-Hydraulics

The Thermal-Hydraulic (TH) model is used to determine the distribution of pressure, enthalpy, temperature, coolant flow and coolant density at steady-state conditions.

The TH calculation considers a domain starting from the core support plate until the end of core that is defined to be the exit of fuel assemblies. Each assembly is modelled as one or six parallel flow channels which are treated individually. Each channel is divided axially into the so-called exposure nodes. Separate loss coefficients can be provided for important assembly components such as spacer grids. For each node of the axial direction of the problem domain, balance principles for energy, momentum and mass of coolant are considered.

3. Programming and parallelization

POLCA8H is developed in Fortran using features up to the version 2008. Shared memory parallelization using OpenMP is utilized. Figure 1 shows the speedup curve of POLCA8H for a full cycle calculation of a VVER-1000. In this cycle calculation, the full core is simulated and each assembly is modelled as six triangles. In addition, the option for automatized calculation of the following quantities was activated:

- Axial offset as a function of total control rod insertion, cycle burnup, and core power
- Differential control rod worth as a function of ditto
- Boron reactivity coefficient
- Power reactivity coefficient

Figure 1 shows the scalability achieved by POLCA8H for an increasing number of computer cores. More specifically, a speed up of ~35 is observed with 60 computing cores. In terms of wall-clock time, using one core the code needs 1h 29m to complete the calculations. When 60 cores are used, the calculation set takes only 2m 22s.

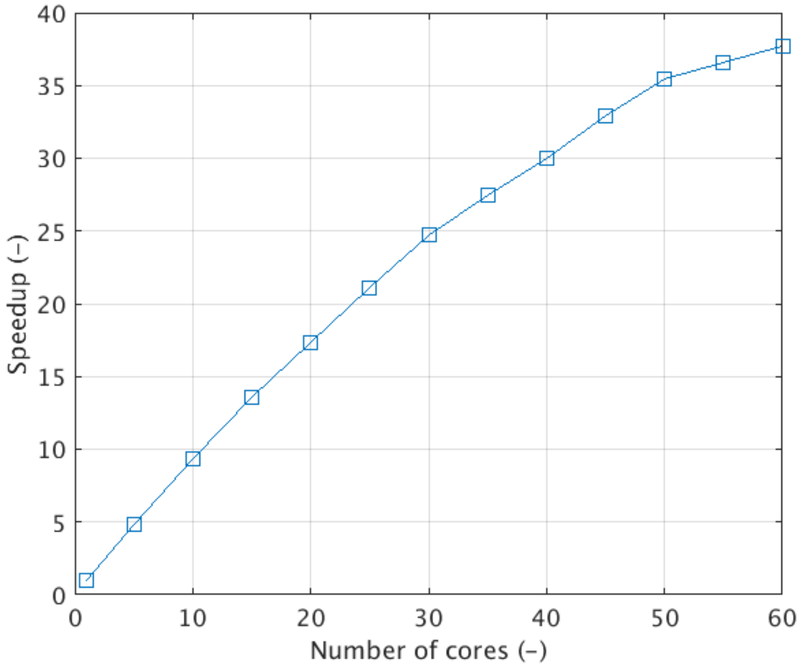

Figure 1. Speedup curve of POLCA8H for a calculation of a VVER-1000 full cycle.

4. Some representative validation results

Apart from specific verification and validation tests, aimed at individual models, the entire POLCA8H code package was validated against the X2 benchmark problem [2]. Some representative results from this benchmark are provided in this section. Comparisons are presented between predictions made by POLCA8H, as well as with other codes in the context of [2]. It should be noted that the objective of this work is not to perform a comparative assessment of POLCA8H against other codes. Therefore, the identities of the other codes used in [2] are not provided in this work, and the emphasis is placed on demonstrating the accuracy and robustness of POLCA8H across the benchmark scenarios.

In subtask 2.1 of the benchmark, predictions of critical boron concentration as a function of the reactor core burnup were compared with measured values for four cycles. Figure 2 shows the operational data used for the simulation of Cycle 01. Figure 3 illustrates the prediction of critical boron concentration in comparison with the predictions made with other codes in the context of [2] and the measured concentration. Figure 4 depicts the deviation between the measured and calculated critical boron concentration vs burnup. The predictions made by POLCA8H are in line with the predictions made by other codes.

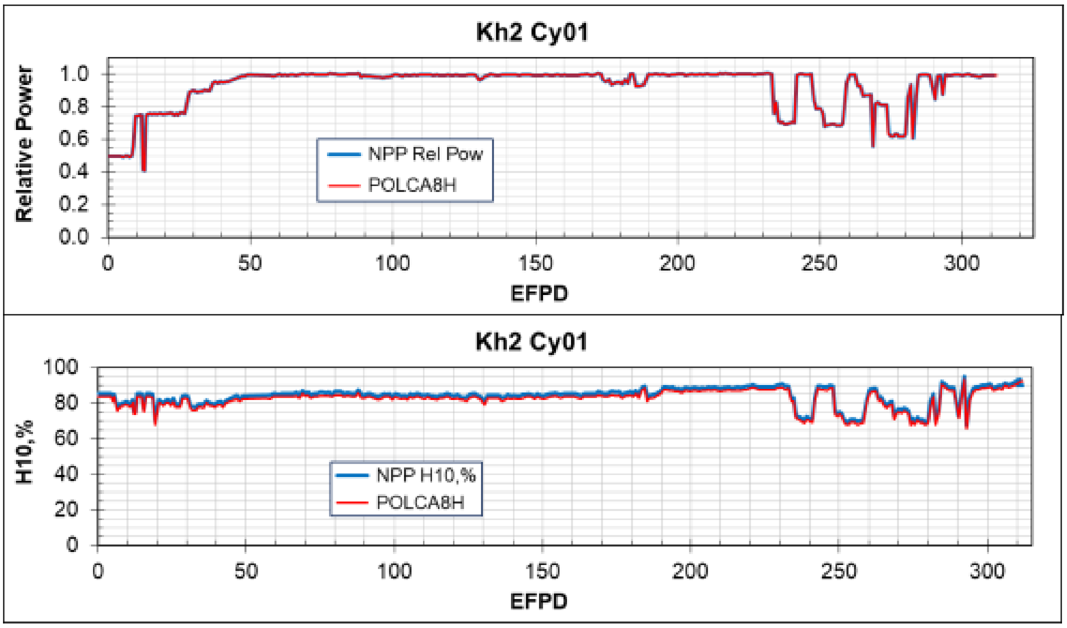

Figure 2. Operating conditions for cycle 01. Reactor thermal power, relative to rated power (top) and control rod bank 10 insertion (bottom).

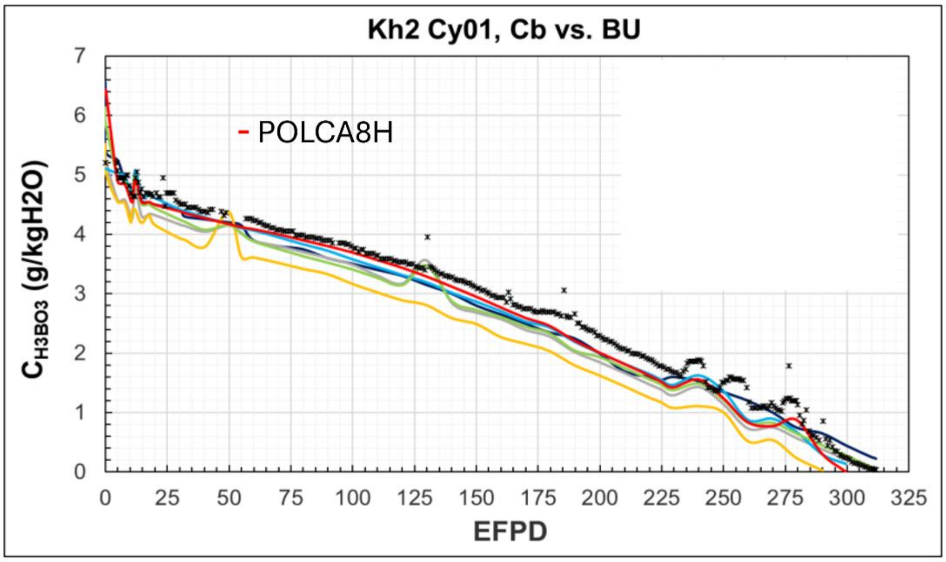

Figure 3. Critical boron concentration for Cycle 1 vs cycle burnup (Effective Full Power Days). The curve predicted by POLCA8H is illustrated with red color. The markers “x” in black represent the measured data.

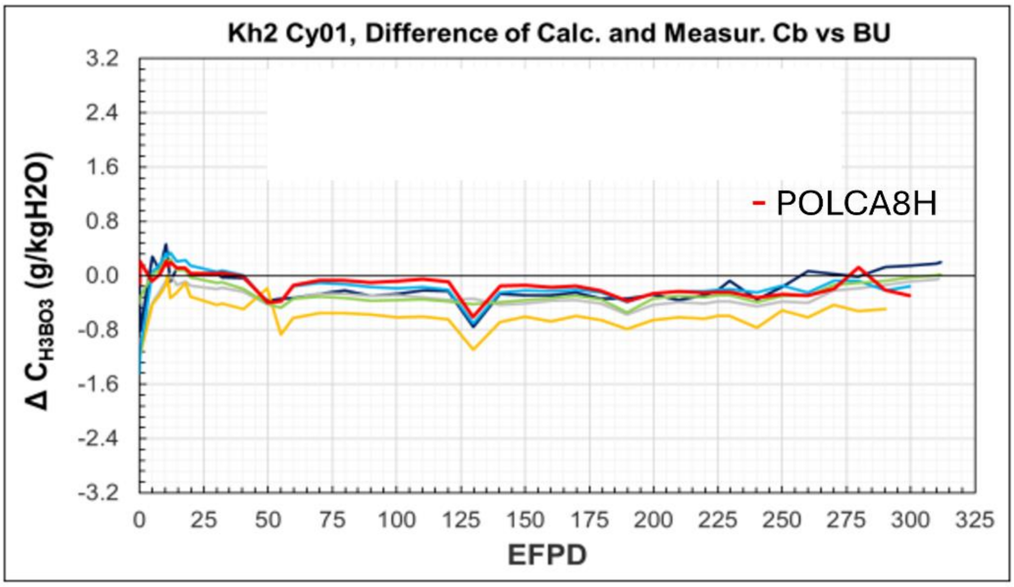

Figure 4. Critical boron concentration of Cycle 0: deviation from measured value for various code packages. The error curve of POLCA8H is illustrated with red color.

In the subtask 2.2 of the X2 benchmark, 2D assembly relative power distributions were calculated and compared against the reconstructed ones, see [2], at the Beginning, Middle and End Of Cycle (BOC, MOC and EOC) in hot full power conditions. Figure 5, presents the RMS error (%) of the assembly averaged power density distributions against the reconstructed values. The RMS error of predictions made with POLCA8H is lower than ~2.5% while notable is its stable behavior.

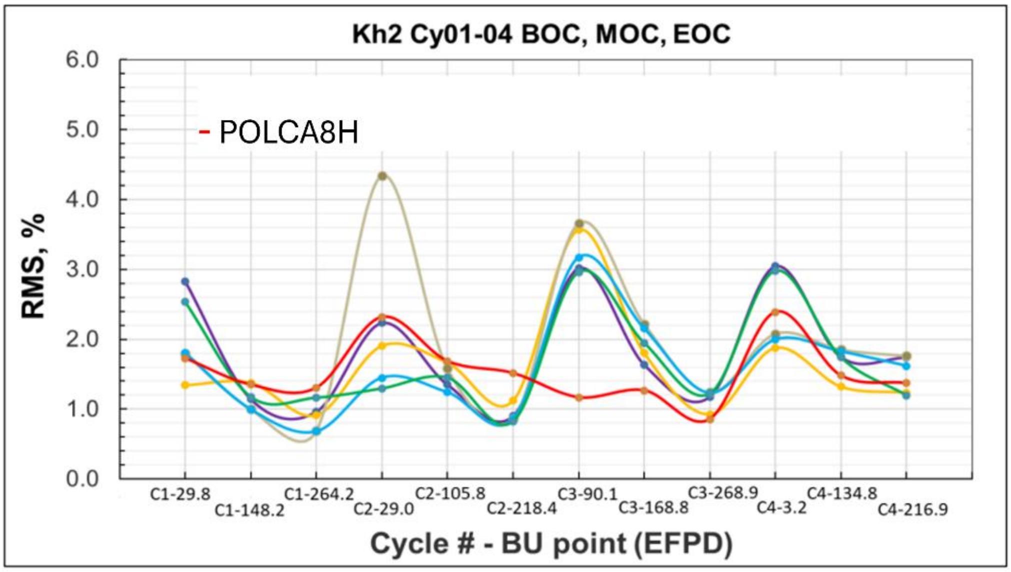

Figure 5. Power distribution RMS error for various code packages: cycles 01-04. The error curve of POLCA8H is illustrated with red color.

Subtask 2.3 regards the simulation of reactor physics measurements at hot zero power conditions. Figure 6 presents the absolute differences between the predictions and the measurements. POLCA8H deviations remain in the range of -0.18 to 0.07 g/kg showing in all cases comparable or lower errors than the ones of other codes.

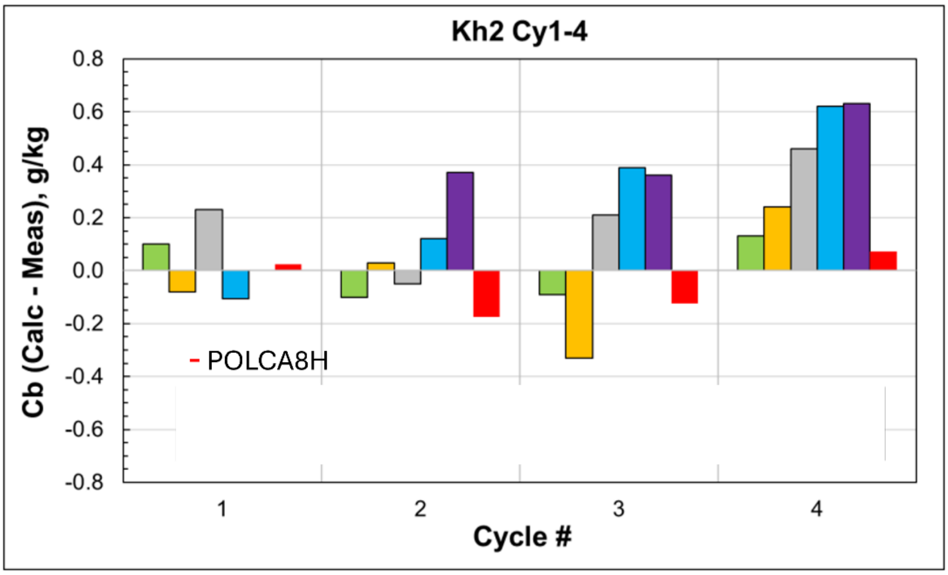

Figure 6. Absolute differences for calculated Critical Boron concentration (g/kg) compared with measurements for HZP, BOC(0) /startup/ condition. The error bar of POLCA8H is illustrated with red color.

In Subtask 3.1 of the X2 benchmark, fuel assembly (FA) axial power distributions at multiple burnup points across four cycles were compared against measured data, reconstructed values, and results from other codes. Figure 7 presents the axial RMS deviation for each assembly location for all available codes throughout the cycles. Notably, POLCA8H demonstrates consistently stable RMS behavior, that is rather independent of the assembly location, burnup point, or cycle number. The RMS differences for POLCA8H are approximately 4% to 6% on average.

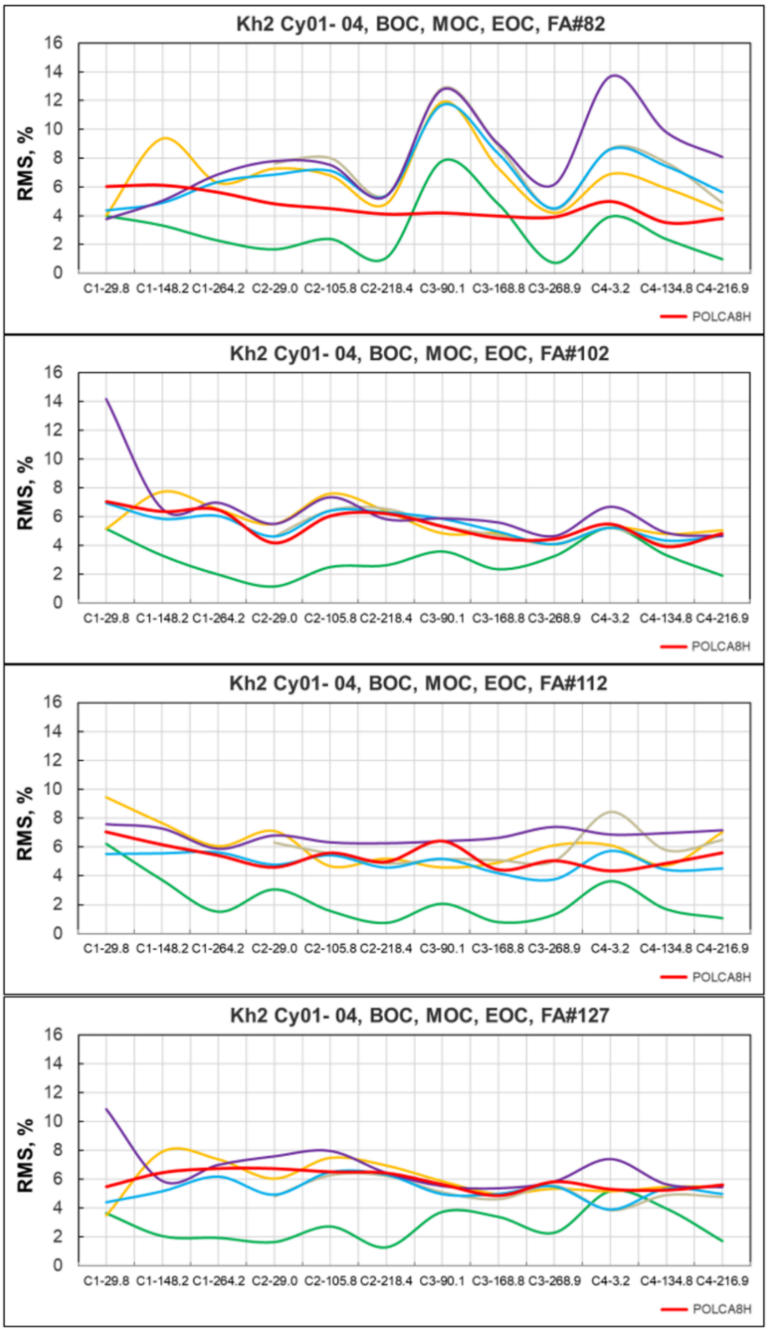

Figure 7. RMS error for axial relative power comparison with reconstructed values for fuel assemblies with absolute coordinates #82, #102, #112 and #127.

5. Conclusions

POLCA8H 1.0, developed by Westinghouse Electric Sweden, is a modern nodal code for VVER-1000 reactors, with planned support for VVER-440 cores. It solves the neutron diffusion equation in hexagonal geometry using the Fourier expansion method, and handles axial heterogeneities via on-the-fly homogenization. The code includes a coupled thermal-hydraulics module that iteratively provides feedback to the neutronics solver. Pin power reconstruction is performed using the traditional two-step method. POLCA8H is written in modern Fortran and is parallelized with OpenMP for efficiency in multithread environments. Initial validation results show a satisfactory accuracy against measurements and predictions from other codes.

Acknowledgement

The authors acknowledge the contributions of Sergiy Maryokhin and Pyry Savolainen for their work on the validation with the X2 task, and Kalev Tammemäe for his efforts in the scalability study. Waldemar Lipiec is acknowledged for his constructive review of the manuscript.

References

[1] Lindahl S.Ö., Mylonakis A., POLCA8 - modelling of cross section variations inside hexagonal assemblies, Int. Conf. Physics of reactors, 2022, Pittsburg, USA, 2022

[2] Lötsch T., Kliem S., Bilodid E., Khalimonchuk V., Kuchin A., Ovdienko Yu., Ieremenko M., Blank R., Schultz G., The X2 benchmark for VVER-1000 reactor calculations. Results and status, Int. Conf. Novel Vision of Scientific & Technical Support for Regulation of Nuclear Energy Safety, Kiev, 2017

LWR 2025 Proceedings, p. 24-30

Mitigation of Local Power Peaking by Introducing HF Spacer Pins in the VVER-440 Follower Fuel Assembly

Akif Abdullayev [1], Douglas Hake [2], Jan Höglund [1]

[1] *Westinghouse Electric Sweden AB, 72163 Västerås, Sweden*
[2] *Westinghouse Electric Company, PA 16066 USA*

E-mail: *akif.abdullayev@westinghouse.com, hakedr@westinghouse.com, hoglunjs@westinghouse.com*

Abstract. A VVER-440 core consists of 312 fixed Fuel- and 37 follower Fuel Assemblies (FA), in total 349 FA. The fixed FAs function as fuel assembly types in western NPPs and VVER-1000 plants. The follower assembly is an extension of the control assembly and is attached to the absorber part by a mating feature incorporated in the top nozzle. The follower is intended to take the place of the control assembly when it is withdrawn.

Enhanced moderation conditions in the fuel-absorber connection region right above the follower fuel rods and low absorption of thermal neutrons in the gas plenum region at the top of the follower fuel rods induces an undesired local power peak in the nearby fuel rods of neighbouring fixed FA when the control assembly is partially inserted in a core. This power peaking in the region of the fuel-absorber connection has two undesirable effects on fuel operation: 1) It increases the neutron flux and linear heat generation and 2) it increases the power ramp when the control rod is moved. For better fuel performance and thermal margins, it is desirable to mitigate this power peak as much as possible.

In Westinghouse VVER-440 follower FAs a neutron absorbing feature is added to the peripheral fuel rods in the form of a hafnium (Hf) spacer to mitigate the power peak in neighbouring fixed FAs. In the 36 peripheral fuel rods, the stainless-steel spacers between the plenum spring and the pellet stack are replaced with Hf spacers which are also relocated to a position between the top end plug and the spring.

In this paper, the results from analyses of the Hf spacers effectiveness to mitigate the undesired power peaks are presented. At first a partially inserted follower FA was modelled in MCNP5 and the pin powers in a neighbouring (fixed) fuel assembly were calculated. Results show that the suppression effect is very strong and that the local excess from the Hf pins is around 15%. However, the axial power distribution from MCNP is not fully realistic and the MCNP calculation also does not consider doppler feedback. These effects are only possible to model in a 3D core simulator.

A more realistic evaluation of the power ramp was obtained by modelling the operation of the follower FAs with Hf pins in the Westinghouse ALPHA-H/PHOENIX-H/ANC-H (APA-H) 3D core simulation code package. A series of calculations was performed for a representative VVER-440 operating cycle with the lead bank moving from an all-out (250 cm) to an all-in (0 cm) position at hot full power. The axial surface power was collected for every fixed FA neighbouring each lead bank. The conclusion that the Hf spacers in the upper non-fuel region of the follower FA do suppress local power in neighbouring assemblies as predicted.

In summary, the results from the local power peak study in MCNP5 and the 3D core simulator modelling in APA-H, clearly demonstrate that Hf pins in the Westinghouse VVER-440 follower fuel is an effective way of mitigating the power peak in surrounding fuel assemblies.

Keywords: VVER-440, Follower, Power Peak, Hafnium

Co-funded by the European Union

Funded by the European Union. Views and opinions expressed are however those of the author(s) only and do not necessarily reflect those of the European Union or Euroatom. Neither the European Union nor the granting authority can be held responsible for them

APIS

1. Introduction

After the Russian full-scale invasion of Ukraine, a joint program between utilities and Westinghouse aiming to diversify fuel deliveries and enhance the security of VVER-440 fuel supply was established with co-funding by the European Union through the Horizon program.

Westinghouse had delivered VVER-440 fuel to Loviisa NPP between 1998 – 2007 and the fuel performance in Loviisa had generally been very good with only one leaking assembly out of 741 operating. However, Grid-to-rod fretting (GTRF) was considered the leaker cause and several rods in the leaking assembly had considerable wear. With reference to these wear indications and the increased fuel resident time required from improved fuel utilization in all European plants, it was concluded necessary to increase the design margins to GTRF and the VVER-440 fuel design was upgraded with new materials and new grid configuration to mitigate GTRF, see Figure 1. The upgraded Fixed VVER-440 design was denoted NOVA E-5 and the Follower design was denoted NOVCC.

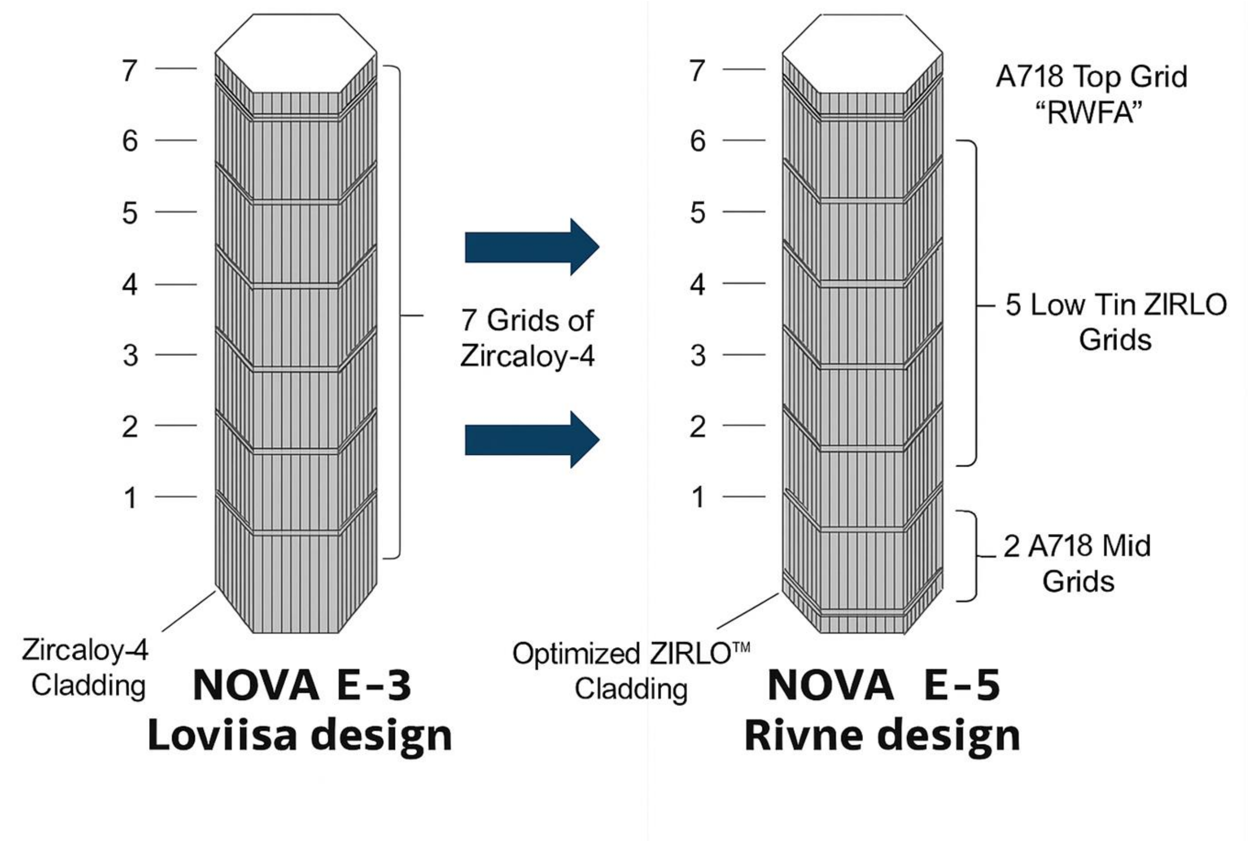

Figure 1. Addition of one grid and change of grid material between NOVA E-3 and E-5

Feedback from several VVER-440 customers on power uprates, margin limitations and Follower operation initiated an additional fuel development program. The next developed designs of Westinghouse VVER-440 fuel are denoted NOVA E-6 and NOVCD. The design changes consist of a longer pellet stack, 60 mm for NOVA E-6 and 40 mm for NOVCD, and corresponding adjustments to other components to enable the increased stack lengths, see Figure 2. In addition, the NOVCD is equipped with a neutron absorbing feature in the follower assembly to absorber rod connection to limit the power peak in this area, see Figure 2.

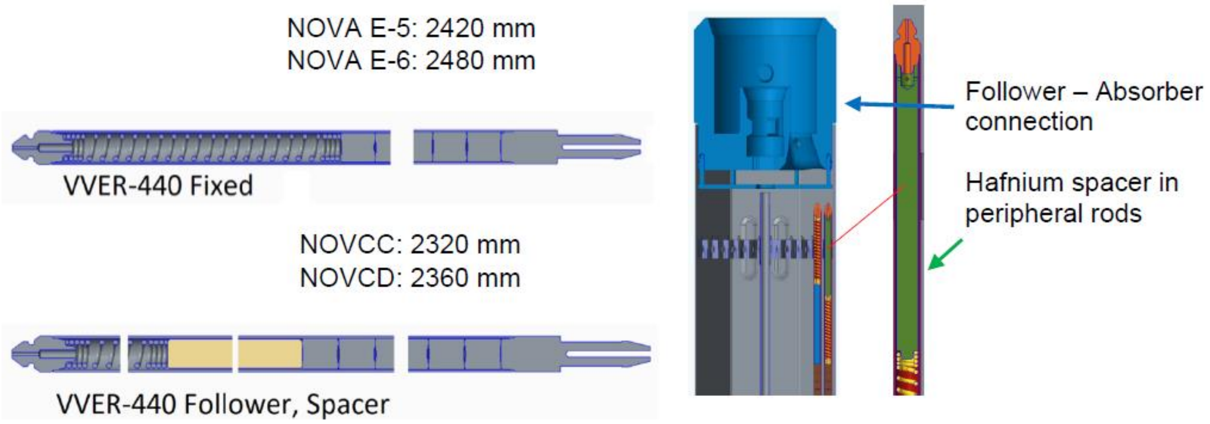

Figure 2. Pellet stack length NOVA E-5 vs. NOVA E-6 and NOVCC vs NOVCD. Hafnium spacers in NOVCD.

Westinghouse VVER-440 NOVCC Follower fuel connected to a control assembly that is partially inserted in a core induces an undesired local power peak in the nearby fuel rods of neighbouring (fixed) fuel assemblies. The power peaking is caused by enhanced moderation conditions in the fuel-absorber connection region right above the follower fuel rods and low absorption of thermal neutrons in the gas plenum region at the top of the follower fuel rods. For better fuel performance and thermal margins, it is desirable to mitigate this power peak as much as possible.

In the NOVCD stainless steel spacers are replaced by hafnium (Hf) spacers in the 36 peripheral fuel rods, see Figure 2. In the peripheral rods the Hf spacers are located above the plenum spring while the central rods with steel spacers have the plenum spring on top, see Figure 2. This solution with the Hf spacers is in European patent EP4343791.

In this paper, the results from analyses of the Hf spacers effectiveness to mitigate the undesired power peaks are presented. At first a partially inserted follower FA was modelled in MCNP5 and the pin powers in a neighbouring (fixed) fuel assembly were calculated. Results show that the suppression effect is very strong and that the local excess from the Hf pins is around 15%. However, the axial power distribution from MCNP is not fully realistic and the MCNP calculation also does not consider doppler feedback. These effects are only possible to model in a 3D core simulator.

A more realistic evaluation of the power ramp was obtained by modelling the operation of the follower FAs with Hf pins in the Westinghouse ALPHA-H/PHOENIX-H/ANC-H (APA-H) 3D core simulation code package. A series of calculations was performed for a representative VVER-440 operating cycle with the lead bank moving from an all-out (250 cm) to an all-in (0 cm) position at hot full power. The axial surface power was collected for every fixed FA neighbouring each lead bank.

2. Analyses with MCNP5

The local power peak induced by a partially inserted NOVCC follower fuel assembly was compared to the corresponding power peak from NOVCD follower fuel. For the calculations the Monte Carlo code MCNP5, v.1.51 was employed. A partially inserted control assembly into the core is modelled in MCNP5 which is used to calculate axial distributions of pin power averaged for selected groups of fuel rods in a neighbouring (fixed) fuel assembly. In addition, axial distribution of pin power is estimated for every pin for the group/row closest to the control assembly.

The geometry of the MNCP model with NOVCD is shown in Figure 3. The central follower assembly is surrounded by one ring of fixed assemblies, and the follower fuel assembly is partially inserted.

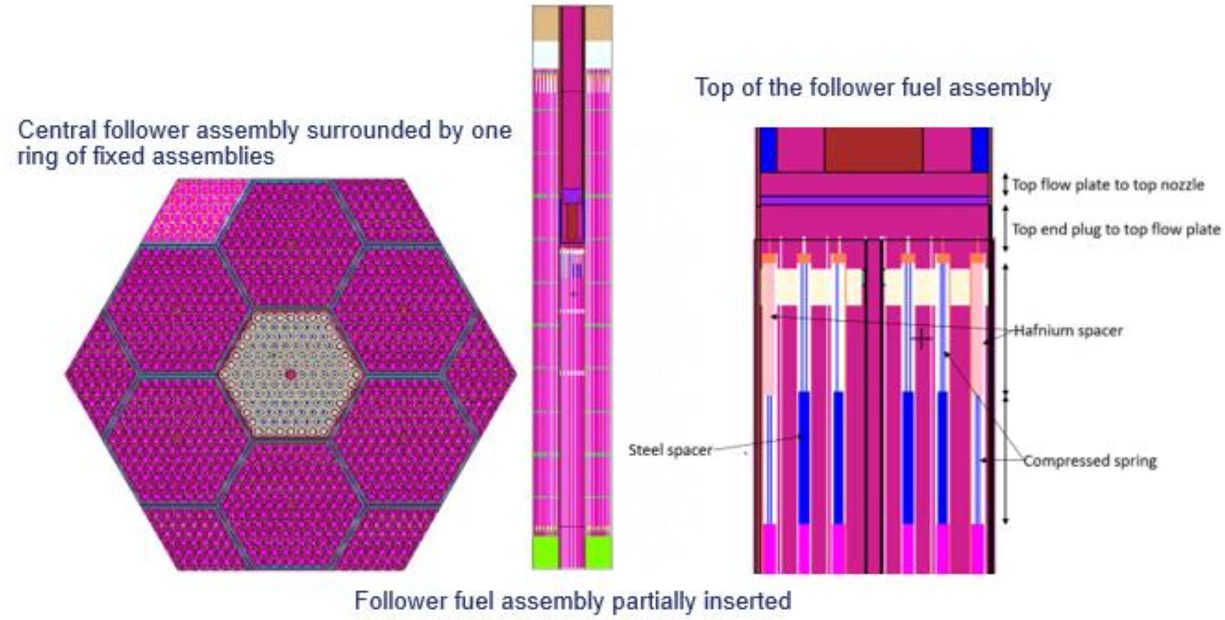

Figure 3. Geometry of the MNCP Model

The assumptions of the MNCP Model are:

- Hexagonal reflective boundary conditions
- Upper and lower reflector regions
- All assemblies have uniform fuel composition simulating 3.82 wt% U-235 with burnup of 26 MWd/kgU
- Axial burnup variation is not considered
- Fuel Temperature: 900 K
- Temperature of all other components: 558 K
- Moderator density: 0.75 g/cm3 (at pressure of 122 bars)
- Zero boron concentration in moderator, simulating EOC conditions

Results from the analyses with MCNP clearly show that the power peak induced by a partially inserted NOVCC is effectively mitigated by the Hf pins in the NOVCD design, see Figure 4.

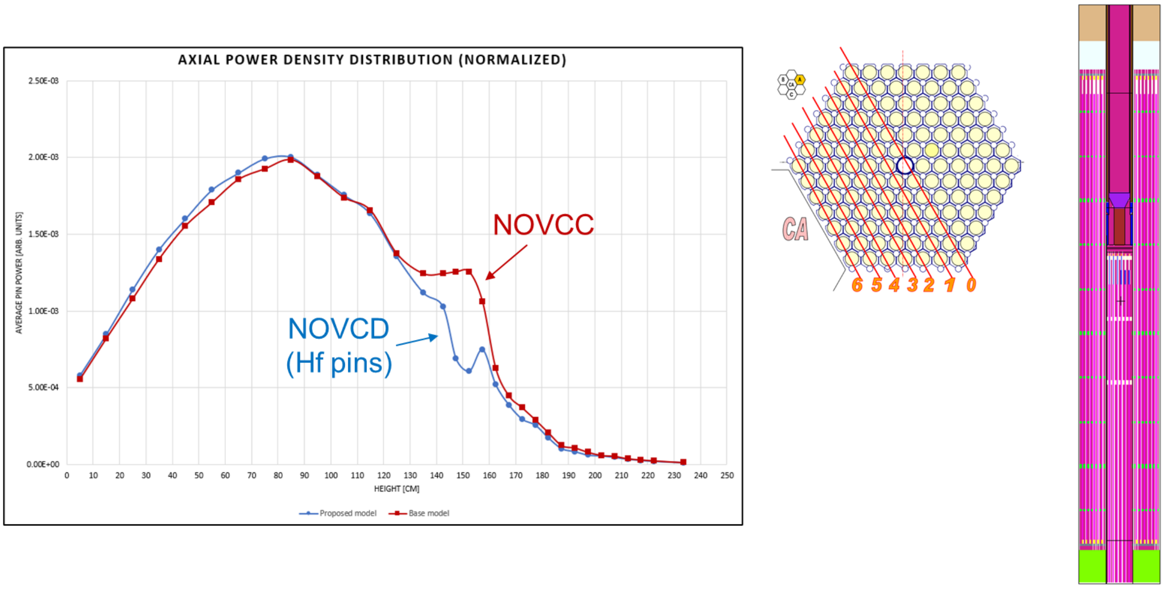

Figure 4. Power peak in neighboring fixed fuel assembly, peripheral fuel rods closest to follower (Row 6)

3. 3-D core simulation with ANC-H

Core with VVER-440 has been simulated using Westinghouse Core Design code ANC-H (Advanced Nodal Code). The hafnium region of the NOVCD leveraged cross sections of resident fuel which includes hafnium plates along the periphery and fixed in shroud. The geometry similar such that its representation in a homogenized node in ANC-H is sufficiently accurate for this study.

A series of calculations was performed for a representative VVER-440 cycle. These calculations represent the lead bank moving form an all-out (250 cm) to an all-in (0 cm) position at hot full power. The axial surface power was collected for every assembly neighbouring each H6 lead bank.

Surface fluxes for one assembly, neighbouring central follower of lead bank, is processed and presented in Figures 5-9 below.

Overall, the plots below a support the conclusion that the inclusion of hafnium spacers, which replaces of stainless steel in peripheral fuel rods do suppress local power in neighbouring assemblies as predicted by MCNP5 calculations.

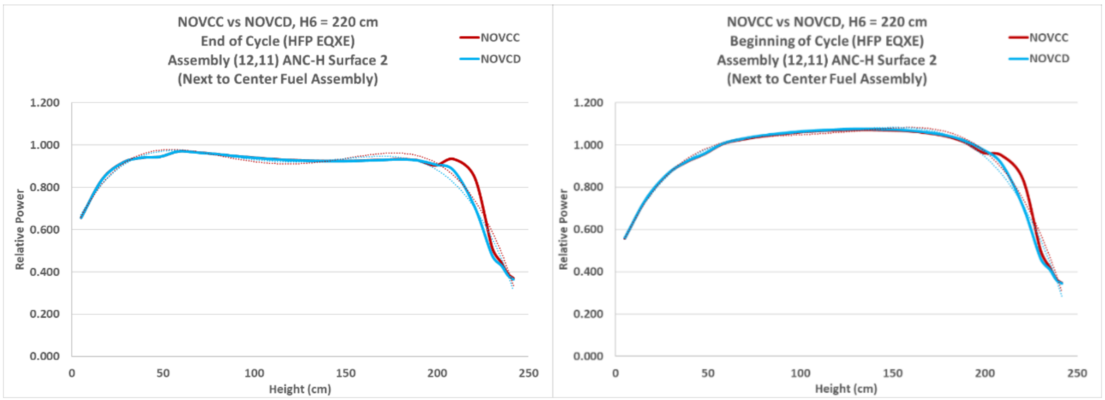

Figure 5. Lead bank inserted to approximately a typical long term operating position

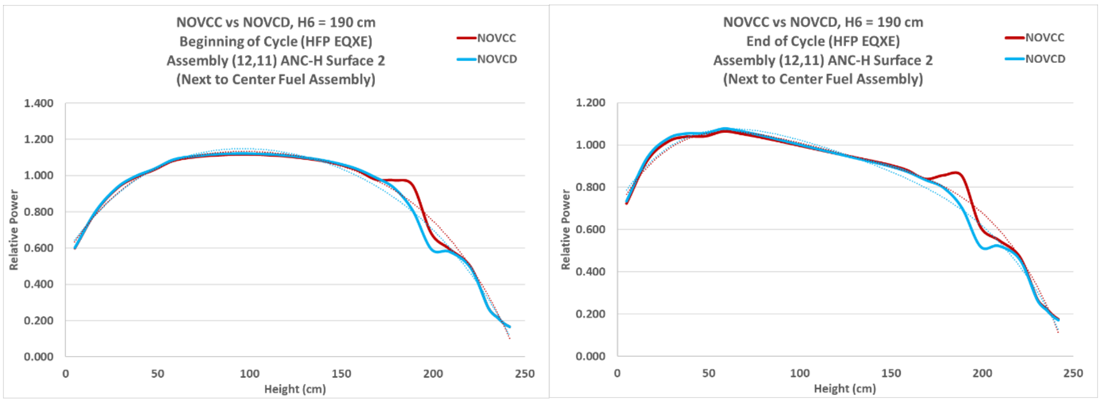

Figure 6. Lead bank inserted to mimic bank position in the MCNP calculations

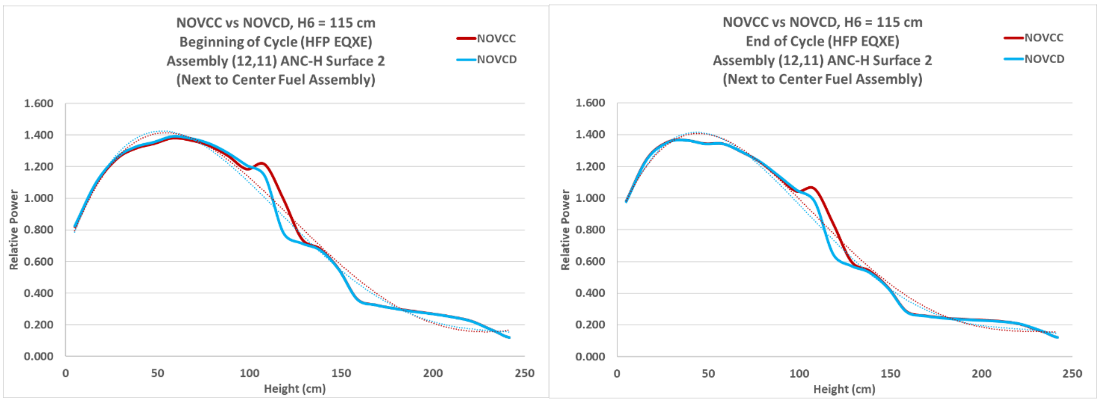

Figure 7. Lead bank inserted to 50% relative to normal operation position

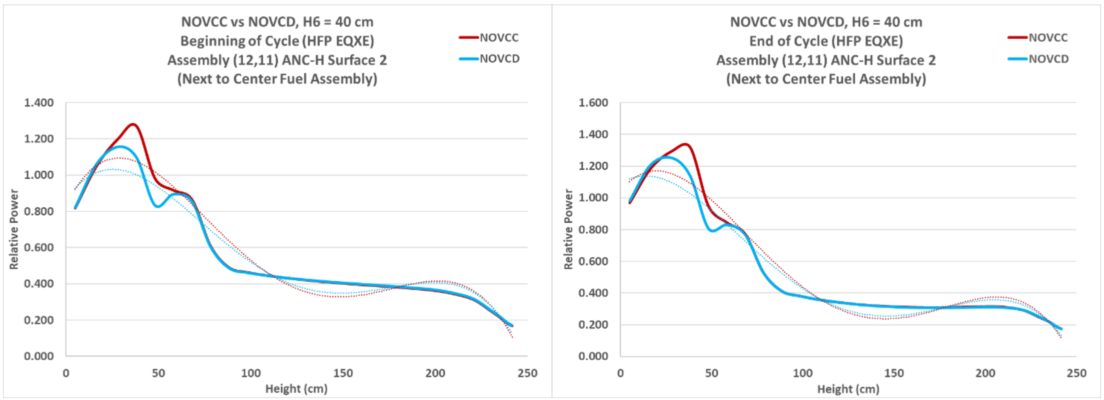

Figure 8. Deep lead bank insertion

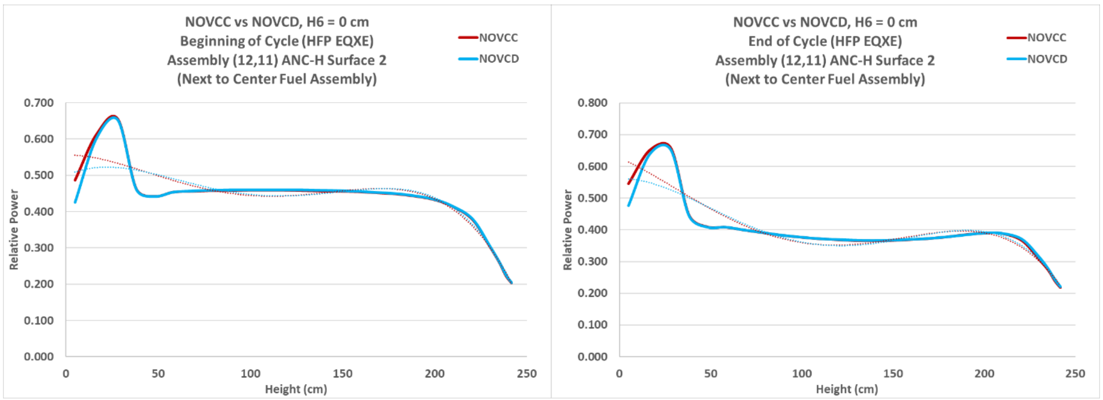

Figure 9. Lead bank full insertion

4. Conclusion

Monte Carlo and 3-D core simulations confirm that the implemented design feature with Hf spacer pins in the follower fuel assembly - NOVCD effectively mitigates local power peaking in adjacent fixed fuel assemblies.

LWR 2025 Proceedings, p. 31-39

Next Generation VVER-1000 Fuel Development

Alex Riznychenko[1], Uffe Bergmann[2], Jan Höglund [3]

[1] – [3] *Westinghouse Electric Sweden AB, 72163 Västerås, Sweden*

*E-mail: *[1]riznyco@westinghouse.com, [2]bergmauc@westinghouse.com, [3]hoglunjs@westinghouse.com*

Abstract. The upgraded Robust Westinghouse Fuel Assembly designs (RWFA/RWFA-T) have demonstrated an excellent irradiation performance in mixed and homogeneous cores of VVER - 1000 reactors in Ukraine, Temelín NPP in the Czech Republic and Kozloduy NPP in Bulgaria with positive overall feedback from all Customers on the fuel performance.

Further enhancement of products for the VVER-1000 market considering the voice of the Customers for potential design improvements is a part of Westinghouse long-term strategy. The ongoing Next Generation VVER-1000 Fuel Development is presented here.

In 2020 Westinghouse initiated a Research and Development project focused on developing a Next Generation Grid Design for Westinghouse VVER-1000 fuel assembly designs family. The objective of the development is to develop a structural grid with improved neutronic, mechanical and thermal-hydraulic properties versus the existing Westinghouse grid designs for VVER-1000 fuel. Zr-alloy grid material is used to enhance the neutron economy. To compensate for the expected reduced grid strength characteristics with use of zirconium material, the grid mechanical design is optimized for increased lateral strength by transitioning from a strap-based design to individual grid cells design. It is expected that this design approach together with optimized to minimize flow resistance cell shape and grid spring will also result in a sufficient overall fuel assembly pressure drop reduction to meet the design objectives. Results of the performed Computational Fluid Dynamics (CFD) calculations, scoping mechanical and comparative tests utilizing prototype grids made by additive manufacturing demonstrated superior lateral strength characteristics and significantly lower pressure drop for the new grid design. Confirmatory mechanical testing is planned to be completed in 2026/2027. Lead Test Assemblies with the Next Generation (NG) Grid Design are expected in 2028.

Keywords: VVER-1000, Development, Grids, Pressure Loss

1. Introduction

Westinghouse has delivered more than 3000 of RWFA VVER-1000 fuel assemblies to different European Customers. An overall RWFA design is presented in the Figure 1.1. The RWFA-T fuel assembly was designed for Temelín NPP, and incorporates 5 mid structural grids with mixing vanes made of Zr1%Nb material for improved thermal performance.

Both designs include similar components such as 312 fuel rods, top and bottom nozzles, 18 guide thimble and one instrument tubes. In total there are 16 and 13 spacer grids respectively in the RFWA and RWFA -T designs. Top, bottom and first mid grids are made from A718 material, while the other grids are made of A718 or Zr1%Nb. The hexagonal grids are strap based, formed by using straight straps intersecting at 60° angles, creating hexagonal grid cells with triangular rod pitch of 12.75 mm. The grid's typical cells are designed to have a co-planar single spring and two dimples offset at 120° each to support the fuel rods.

Co-funded by the European Union

Funded by the European Union. Views and opinions expressed are however those of the author(s) only and do not necessarily reflect those of the European Union or Euroatom. Neither the European Union nor the granting authority can be held responsible for them

APIS

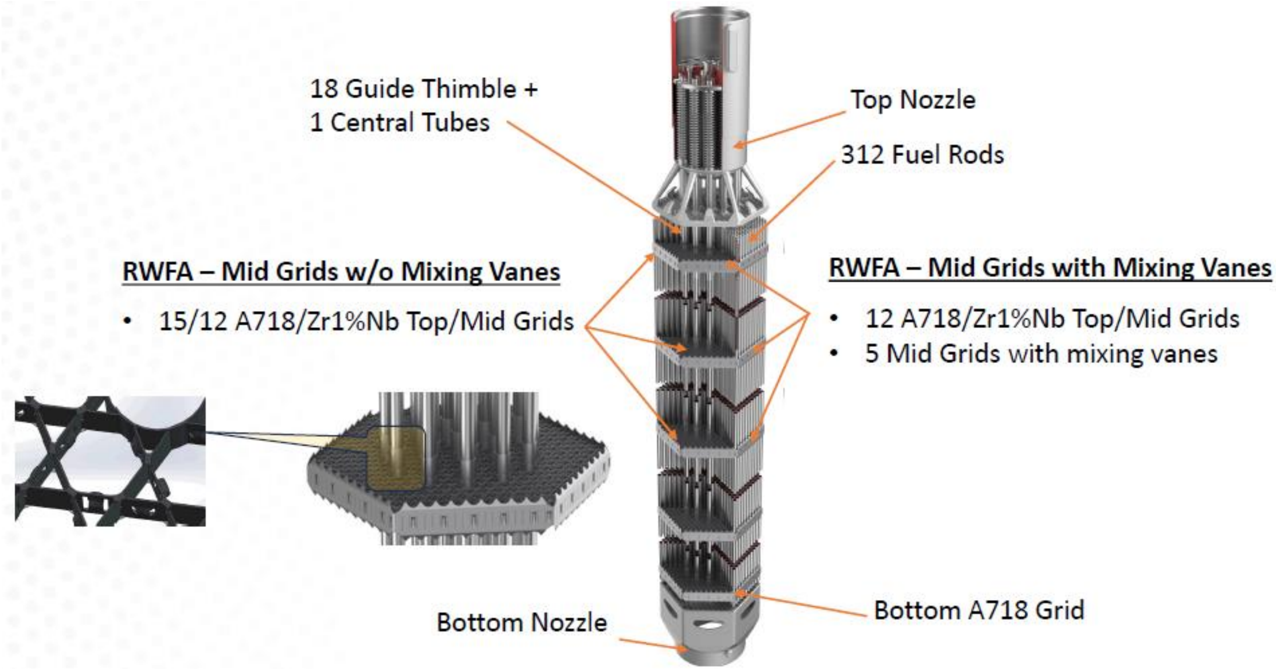

Figure 1.1 Overall Westinghouse VVER-1000 design

Both RWFA and RWFA-T fuel assembly designs have demonstrated an excellent irradiation performance in mixed and homogeneous cores of VVER-1000 reactors in Ukraine, Temelín NPP in the Czech Republic and Kozloduy NPP in Bulgaria with positive overall feedback from all customers on the fuel performance.

Based on customer feedback and experience from operations in Ukraine and Temelín it was concluded that a new grid design with lower pressure loss and improved lateral strength characteristics will help to enhance products for the VVER-1000 market within the Westinghouse long-term strategy.

In 2020 Westinghouse initiated a Research and Development project focused on developing a Next Generation Grid Design for Westinghouse VVER-1000 fuel assembly designs family. The objective of the development is to develop a structural grid with improved neutronic, mechanical and thermal-hydraulic properties versus the existing Westinghouse grid designs for VVER-1000 fuel. Zr-alloy grid material is used to enhance the neutron economy. The following objectives are defined for the Next Generation Grid:

- Mid grids of Zr-alloy material to improve neutron economy.
- A 20 % pressure drop reduction for grids without mixing vanes compared to the existing RWFA grid design. Expected pressure reduction for the entire Fuel Assembly is ~12%.
- A Zr-alloy structural grid strength at least as for the RWFA A718 grids. An improved grid lateral strength will enable an increase of the vertical handling speeds during core loading/unloading.
- Possibility to incorporate mixing vanes for improved DNB performance.

To compensate for the expected reduced grid strength characteristics with use of zirconium material, the grid mechanical design is optimized for increased lateral strength by transitioning from a strap-based design to individual grid cells design.

2. NG VVER-1000 structural grid

There is a very limited room in the existing strap-based grid design technology to reach the objectives of the research and development project. Any grid modifications made to reduce the grid pressure loss in most cases will cause a reduction in grid strength which shall be increased instead and any increase in mechanical strength requires design changes that will lead to increased pressure drop. Therefore, alternative grid design concepts that have potential to reach the main development objectives have been considered during the development. The grid design presented herein is an individual cell-based grid design that consist of 312 single cells, see Figure 2.1

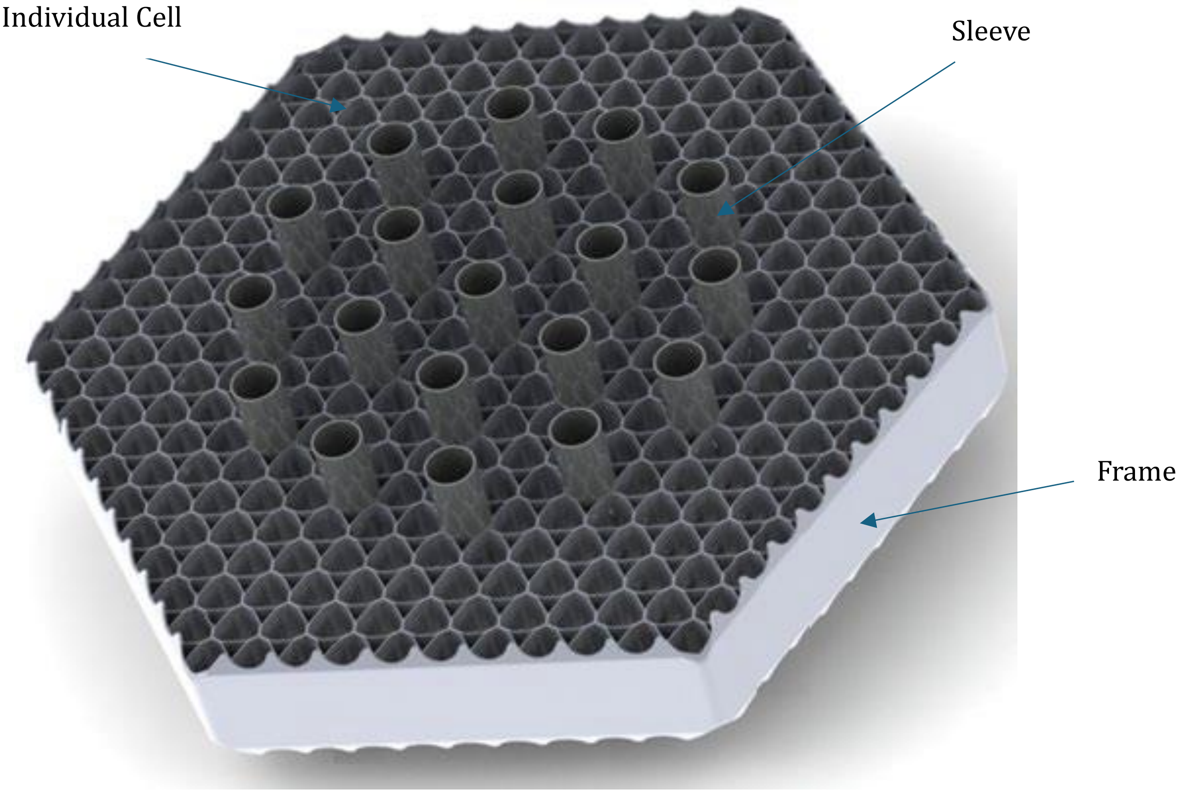

Figure 2.1 *NG VVER-1000 Structural Grid Overall View*

Each cell is formed from a sheet of metal to the designed cell shapes. Individual cells, outer straps and sleeves are assembled in a welding fixture and joined by laser welding. The quantity of unique cell types was optimized to improve grid manufacturability. Similar cell forming and grid manufacturing processes are utilized at Westinghouse Sweden (WSE) to manufacture spacer grids for Boiling Water Reactor fuel designs. There is an extensive experience at WSE concerning dimensional tolerances and process capability to manufacture cell-based grid designs. Results of the performed scoping tests and evaluations showed that the cell-based grid design approach has a hight potential to meet the design objectives.

3. Scoping tests and preliminary evaluations

3.1 Testing of additively manufactured grids

Additive manufacturing (AM) was used to enable for early scoping tests of several new design options. Full scale prototype test grids have been built in Inconel A718 by AM on Westinghouse's EOS M290 machine. New grid concepts and the RWFA grid design, used as reference design, have been printed, see Figure 3.1 as an example.

Figure 3.1 Additively manufactured RWFA grid

The geometry of the AM build models was optimized to reach similar mechanical and thermal-hydraulic properties as grids made by conventional manufacturing. For example by adding simulated weld nuggets on the AM built RWFA grids to match a realistic grid flow blockage area, see Figure 3.2.

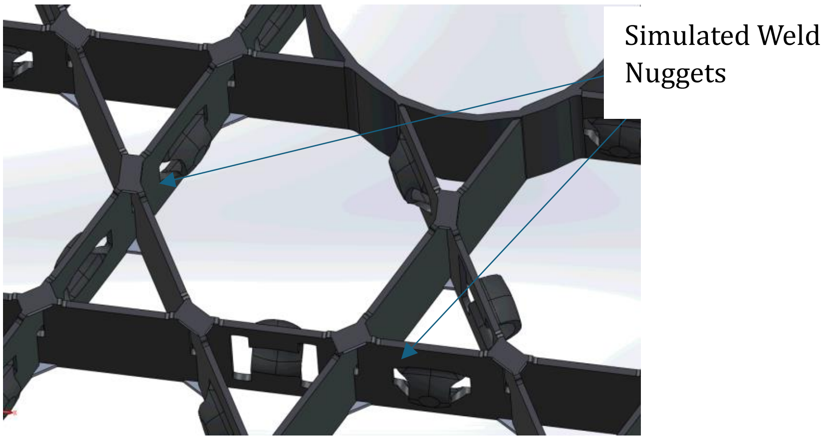

Figure 3.2 Simulated intersection weld nuggets on AM RWFA grid.

Machine printing and heat treatment parameters have been optimized to reach similar material properties as conventional grids. To reduce the surface roughness of AM built grids closer to conventional manufactured grids, chemical etching was used for the final surface treatment. This process improved the surface roughness significantly. However, the low levels of roughness for conventionally manufactured grids were not reached in full.

Comparative scoping mechanical and hydraulic tests have been performed on new grid concepts and on RWFA grids made by AM and also on RWFA production grids to obtain a baseline for the comparison. The AM grid testing objective was to evaluate following characteristics on the new grid design concepts:

- DNB performance. Tests were carried out in the Westinghouse ODEN loop;
- Pressure drop. Tests were carried out in the new Westinghouse EMBLA loop;
- Grid lateral strength, obtained by applying static loads on sides and corners;
- Rod loading forces.

3.1.1. DNB scoping test in the ODEN loop

The DNB test objective was to show that a cell-based grid design and strap-based grids without mixing vanes have comparable DNB performance. Mini-size AM grids of a new design concept with 3 hexagonal cell layers containing 19 heater rods and no thimble with use of uniform heater rods have been tested within a smaller test matrix to obtain a level of DNB performance. The obtained DNB performance results have been compared one-to-one against data from previous DNB tests performed in 2012 on the WFA design which has grids similar to the RWFA design. Test results demonstrated a good agreement within a few percent of difference. The test demonstrated that the existing DNB correlation can be applied to the new cell-based grid design without need of further DNB testing.

3.1.2. Pressure drop scoping test in EMBLA loop

A scoping test was performed using a full-size VVER-1000 skeleton mockup to measure relative differences in pressure drop of the AM New Grid Design vs. an AM RWFA grid and an AM RWFA grid vs. a conventionally manufactured prototypical RWFA grid. Results presented in Figure 3.3 show lower pressure drop by ~30% of the AM new grid compared to the AM RWFA design In Figure 3.4 a 10% higher pressure drop for the AM RWFA grid vs the prototypical RWFA grid is shown. This indicates that the AM process and AM RWFA design features add ~ 10% in pressure loss against a conventionally manufactured RWFA grid. This pressure drop scoping test demonstrated that the new cell-based grid design has a clear potential for reduced resistance to the flow in comparison with the existing RWFA grid design.

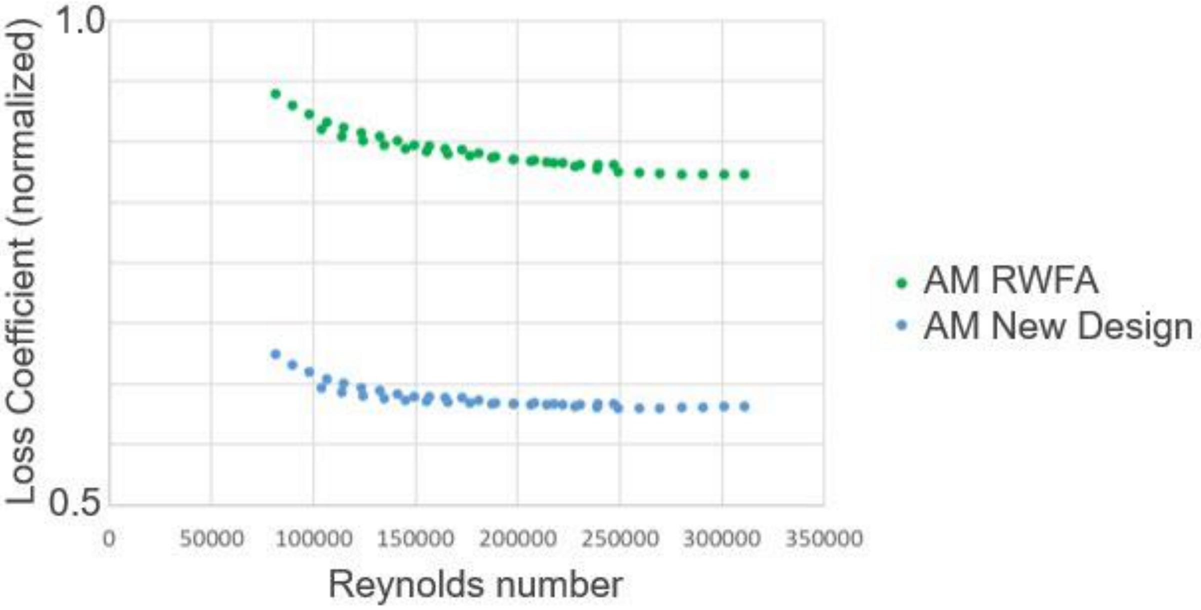

Figure 3.3 AM RWFA vs AM New Grid Design Normalized Loss Coefficients

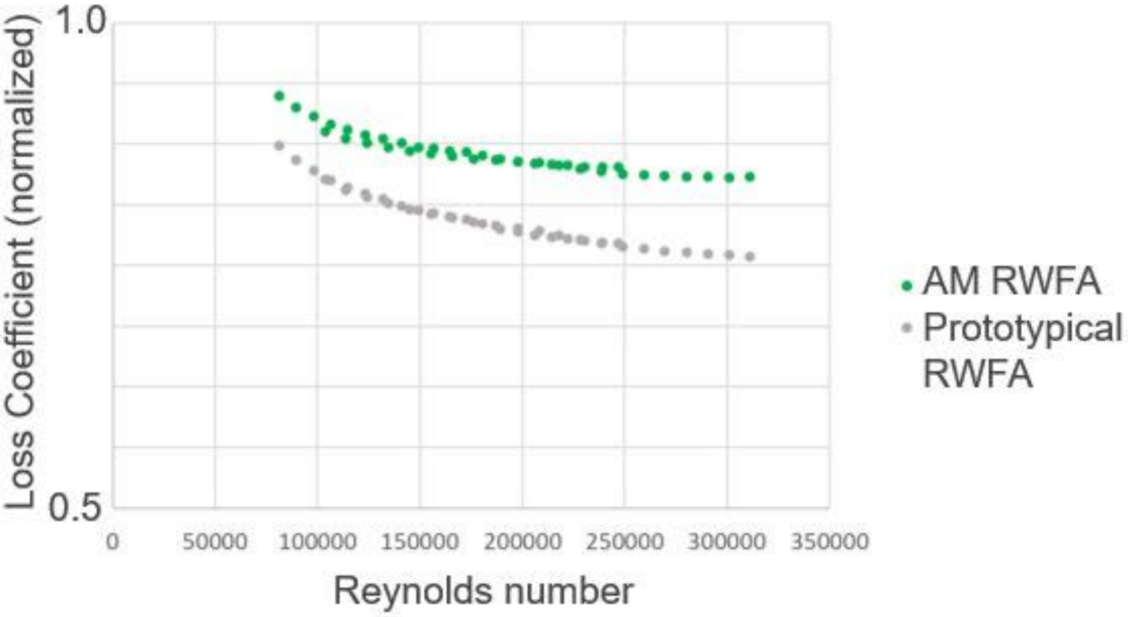

Figure 3.4 AM RWFA vs RWFA Production Grid Design Normalized Loss Coefficients

3.1.3. Lateral load comparative scoping test

This test was performed on prototypical RWFA, AM RWFA and AM new grid design variants. The overall test setup in presented in Figure 3.5.

Figure 3.5 Lateral Scoping Test Setup

The AM RWFA test results demonstrated similar loads for onset of buckling versus the production RWFA grid. The new grid design demonstrated a potential for improving the lateral load capacity against the existing RWFA grid design.

3.1.4. Simplified rod loading scoping test

The test was done on prototypical RWFA, AM RWFA and AM new grid design variants. Overall test setup is presented in Figure 3.6. During the test, a single test rod was manually pushed through grid cells using three guiding fixtures while measuring the drag force. Cells surrounding the test cells were filled with rodlets to simulate fuel rod presence in adjacent cells. Test results demonstrated acceptable loading forces for the new grid design variants.

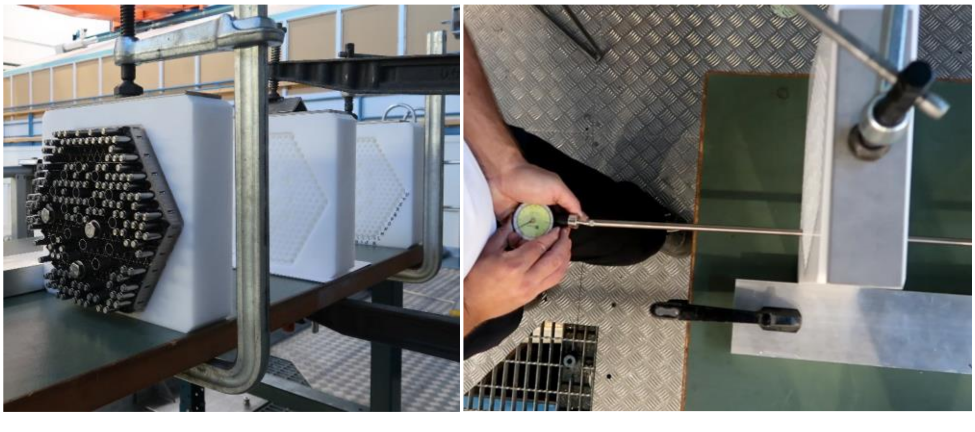

Figure 3.6 Rod Loading Test Setup

3.2. Detailed design phase testing and evaluations

Several scoping tests have been performed during the detailed NG design phase:

- Individual spring load-deflection test

- Spring structural simulation
- Mini grid testing:
  - Rod drag test
  - Cell stiffness test
- Structural simulation of a full grid model

Obtained results provided input for grid spring design selection and tuning to finalize the NG grid design for confirmatory testing.

3.2.1. Individual spring testing and simulations

The testing was performed on individual test samples stamped from A718 material, heat treated to have as-build grid material properties. Test results provided load-deflection characteristics of the considered spring designs to validate ANSYS spring models. As an example, in Figure 3.7 a spring load-deflection curve obtained by testing is shown together with the ANSYS analytical model. The spring models were developed for structural verification of considered spring types made of A718 and **Low Tin ZIRLO™** (LTZ) for in-cell force optimization. The same models were used also for simulation of fuel rod insertion for spring optimization to minimize risk of spring distortion.

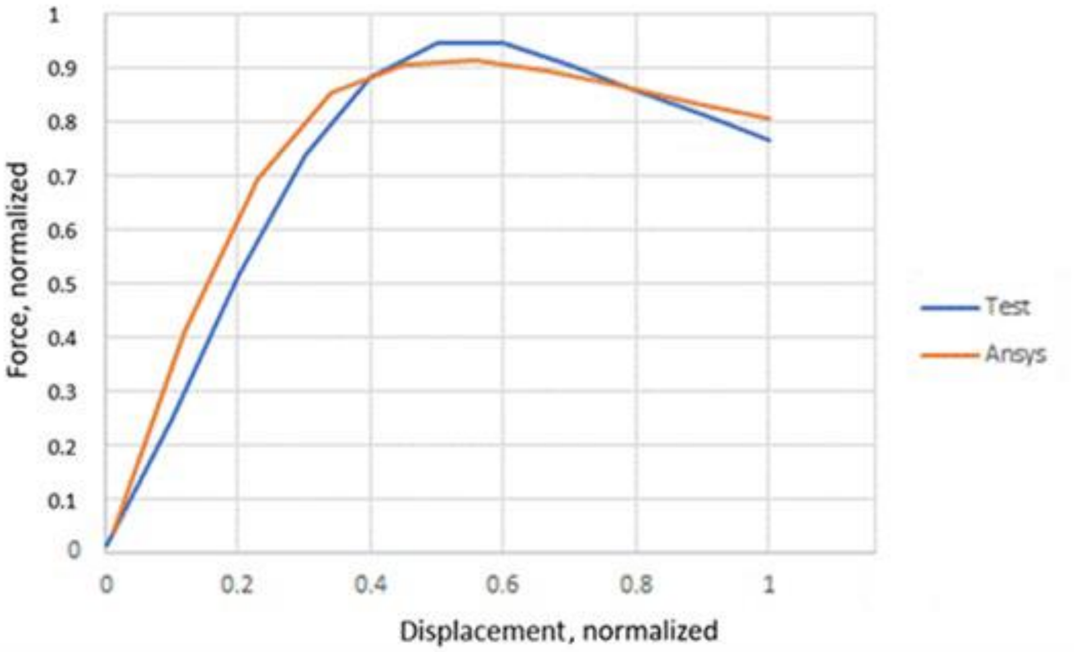

Figure 3.7 Grid Spring Load-Deflection Curves

3.2.2. Mini grid testing

Mini grids were made of 7 LTZ cells welded together by means of laser welding. Two sets of mini grids with two considered spring types were heat treated and cells pre-sized with use of mandrels to represent as-built grid condition. Prototype manufacturing of mini grids has been successfully completed and provided an input for manufacturing evaluation of the full-scale grids.

A drag test was performed to determine the in-cell drag force during fuel rod insertion in 7-cell mini-grids with the considered spring types. An evaluation of the residual deformation of the spring designs after rod insertion based on 3D spring scans before and after testing has also been performed during this testing. Measured drag forces during the test were in the intended range predicted by the ANSYS analytical models. Considered spring types demonstrated an excellent resistance against spring distortion due to fuel rod end plug insertion.

An in-cell stiffness test performed with the use of mini grids confirmed the expected in-cell spring characteristics predicted by analytical models.

Mini grid testing provided input for spring type selection to finalize grid design for confirmatory testing.

3.2.3. Structural simulation of full grid model

Structural evaluation of a full scale ANSYS model has been performed considering several grid design features and conditions such as cell design, spring type, cells welding, interaction between cell walls, presence of fuel rod sections, spring pretension and plastic material model for grid components. Simulation setup included grid side support with force applied through push plates to the full grid side or locally at corners or side centre.

Simulation results showed that calculated grid lateral vs deflection characteristics comply with expected results to meet the NG grid design objectives. This study also provided input for spring type selection to finalize grid design for confirmatory testing. Confirmatory mechanical test will be performed complete full-scale conventionally manufactured grids to verify grid lateral strength characteristics.

4. Status of the NG VVER-1000 fuel development

The NG grid development project is successfully progressing. Confirmatory grid crush strength testing, pressure loss and grid-to-rod fretting performance testing are expected to be performed with conventionally manufactured grids during 2026. Remaining tests and validations are scheduled for completion in 2027. Loading of lead test assemblies are expected in 2028.

Towards Modelling of Advanced-Technology Fuel Rods with the TRANSURANUS Code

A. Schubert*[1], I. M. Paponetti[2], P. Aragón[1],
D. Jaramillo-Sierra[1], Zs. Soti[1], P. Van Uffelen[1]

[1]European Commission – Joint Research Centre, Karlsruhe, Germany
[2]University of Bologna, Italy

[*]*E-mail: Arndt.Schubert@ec.europa.eu*

Abstract. In the frame of the Euratom APIS project (Accelerated Program for Implementation of secure WWER fuel Supply), properties for advanced technology fuel (ATF) have been implemented in the TRANSURANUS fuel rod performance code of the European Commission's Joint Research Centre (JRC). The APIS project includes the application and qualification of fuel performance simulations, making use of datasets from the International Fuel Performance Experiments (IFPE) database of the OECD/NEA, as previously applied in Co-ordinated research projects (CRP's) of the IAEA (FUMEX-II and FUMEX-III).

This paper demonstrates the implementation and application of near-term advanced-technology fuel in the TRANSURANUS code – by the examples of Cr-doped UO_2 fuel, Zirlo cladding as well as Cr-coated cladding. For 4 transient-irradiated WWER fuel rods compiled in the IFPE database (Kola3-MIR dataset), the outcomes of the earlier IAEA projects were reproduced and complemented by means of the latest version of TRANSURANUS. Starting from standard UO_2 fuel and Zr1Nb cladding and assuming identical irradiation histories, the simulated impact of the above-mentioned hypothetical ATF fuel and cladding configurations was analysed for: the fuel-to-cladding gap sizes, the fuel centre temperatures, the integral fission gas release as well as the final radial profiles of the local Xe concentration. The results are consistent with those published earlier in the frame of the APIS project but show in more detail the impact on fission behaviour in doped fuels with larger grains and initial density. The simulated performance of ATF fuel rods meets expectations when compared to the standard options, especially the reduced fission gas release during the ramp tests.

1. Introduction

This paper outlines part of the progress from the Euratom project 'Accelerated Program for Implementation of secure WWER fuel Supply (APIS)' (https://apis-project.eu/). The project is divided into several work packages (WP's), each focusing on different aspects of advanced fuel development, modeling and application. We focus here on one (WP6) that is specifically dedicated to advanced fuel performance modeling. The objectives of that WP include implementing new material properties in the latest version of TRANSURANUS [1-4], updating coupling interfaces for multi-physics analysis, and developing modern methodologies for model development and code calibration within the Best-Estimate Plus Uncertainty (BEPU) analysis framework [5-7].

The extensions of the TRANSURANUS code in the frame of the APIS project are outlined in section 2. In the following section, we present its application with fuel performance simulations using datasets from the International Fuel Performance Experiments (IFPE) database of the OECD/NEA [8]. The paper demonstrates in particular the application of the TRANSURANUS fuel rod performance code to near-term advanced-technology fuel (ATF), the results of which are summarized in the fourth and last section, together with the outlook.

2. Extension of the TRANSURANUS fuel performance code

This section addresses a part of the extensions of the TRANSURANUS code to include properties for near-term advanced-technology fuels. They cover property models for the Cr-doped UO_2, ZIRLO cladding and Cr-coated Zircaloy-4, for which advanced fuel materials have been implemented by the JRC in the TRANSURANUS code, while Westinghouse implemented ADOPT^{TM} fuel property models.

2.1 Fuel and cladding material properties

For simulating Cr-doped UO_2 fuel, specific correlations for fuel creep and densification are applied [2,4]. Fuel cracking is simulated according to the model of Oguma et al. [9]. Additional considerations [10] were made to model the effect of Cr doping in UO_2:

- Adding dopants produces a fuel with a higher density [11]. Fuel densification is thus largely prevented during the base irradiation period.
- An enlarged grain size is accomplished by the addition of the Cr-based dopant.
- Fission gas diffusivity is enhanced due to the presence of Cr_2O_3 in the UO_2 matrix [12].

For Zirlo cladding, a set of correlations and models has been implemented, based on the material properties library [13] issued by the US Nuclear Regulatory Commission (NRC).

2.2 Coating of cladding

The TRANSURANUS fuel performance code has been extended to simulate Cr-coated cladding by independently modelling the coating and the cladding [3,14]. To this end, a set of material properties for Cr metal is applied to the outermost radial zone of the cladding. On the contrary, a homogenized tube of coated cladding is considered when applying correlations for burst stress and rupture strain. While a dedicated correlation for corrosion of Cr coatings at high temperatures [3] is implemented, any corrosion is neglected during base irradiation.

3. Application of TRANSURANUS code extensions

3.1 Hypothetical configurations

For the present analysis we have chosen one fuel rod (#50) ramp tested in the Kola3-MIR transient experiment analyzed in the FUMEX-III project [15]. The analysis focuses on the impact of different ATF configurations on fuel performance parameters such as fuel-to-cladding gap sizes, fuel centre temperatures, integral fission gas release, and final radial profiles of local Xe concentration. While the standard configuration of UO_2 fuel and E110 (Zr1Nb) cladding (cf. [16,17]) is used as basis, the code settings are consecutively modified to Cr-doped UO_2 fuel, Zirlo cladding, and to a combination thereof. In addition, each of these configurations has also been simulated together with a 20 µm thick Cr coating layer on the cladding surface. Regarding Cr-doped UO_2 fuel, the following assumptions were made for the cases analyzed in this paper:

- The initial grain diameter is increased to 50 µm.
- The initial porosity is reduced to 2.5%.
- Fuel densification is negligible.

3.2 Fuel radial geometry and fuel centre temperatures

Figure 1 compares the simulated fuel-to-cladding gap in one fuel slice for 6 different material configurations, starting from the standard UO_2 fuel and E110 cladding, and consecutively applying Cr-doped fuel, Zirlo cladding as well as a combination thereof. The markers illustrate the effect of adding the Cr coating to both E110 and Zirlo cladding.

Expected differences can be seen during the base irradiation: Mainly because of fuel densification, standard UO_2 shows an increase of the gap size prior to approx. 4000 h. Due to the absence of densification this trend is not observed for Cr-doped fuel, and after approx. 6000 h of irradiation we see nearly parallel lines when applying the same cladding for the 2 different fuel types. The simulations of E110 (standard) and Zirlo cladding in turn differ by the different slopes of the gap size evolution. They can be seen already in the early irradiation phase and are mainly due to differences in cladding creep-down. Finally, when applying Cr coating to either cladding type, the given case shows only a very small additional change of the simulated gap size (differences between dashed lines and markers in Figure 1).

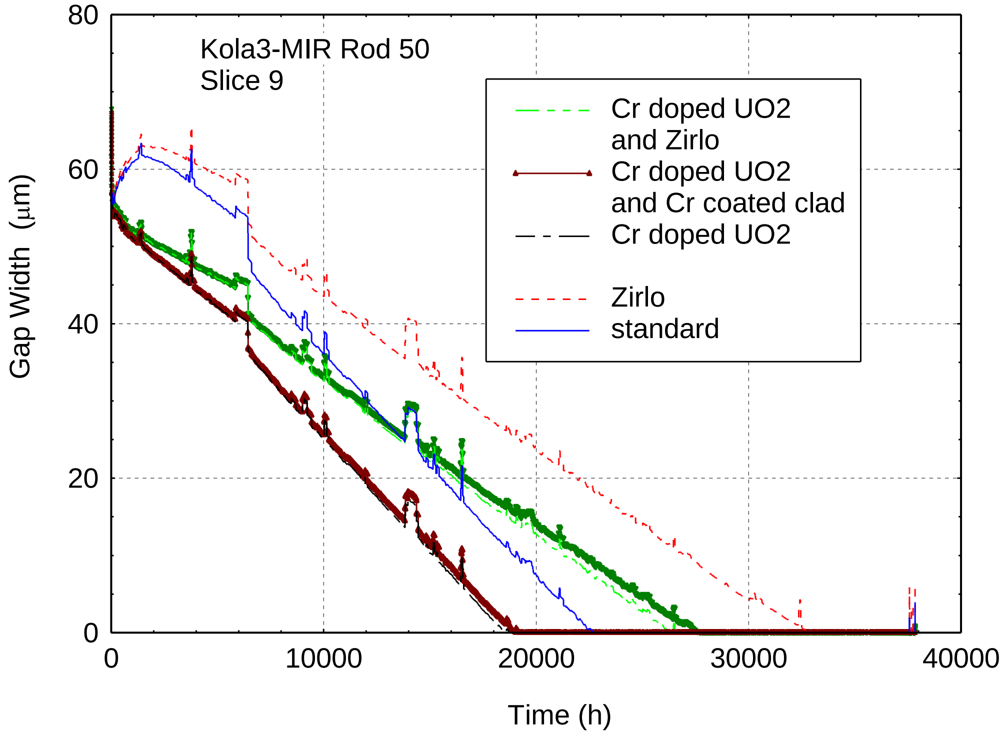

Figure 1. Dependence of the simulated fuel-to-cladding gap width on the irradiation time for the base irradiation of one ramp-tested WWER-440 fuel rod.

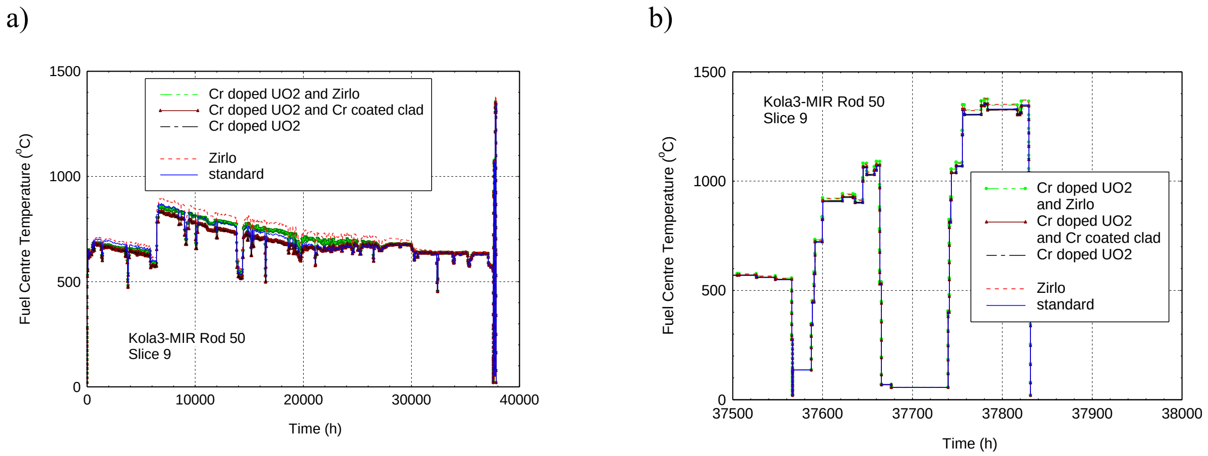

Figure 2. Dependence of the simulated fuel central temperature on the irradiation time for (a) the base irradiation and (b) the correspondent ramp-tests of one WWER-440 fuel rod. See text for details.

Figure 2 shows the corresponding simulations of fuel centre temperatures. The largest differences are observed in the base irradiation and can mostly be linked to the differences in gap sizes as discussed in Figure 1. The temperature evolution in Figure 2b illustrates the 2 ramp phases of the Kola3-MIR experiment. Due to the closed fuel-to-cladding gap the impact of applying the hypothetical ATF configurations is very small (< 25 deg) even at high fuel temperatures (> 1300 °C).

3.3 Uncertainty analysis

To assess the impact of the new material property uncertainties on the fuel behaviour predictions under both normal and transient conditions shown above, we have made 1000 independent runs generated automatically by the Monte Carlo tool embedded in the TRANSURANUS code.

***Table 1**: Uncertainty parameters considered for the fuel and cladding material properties*

Material property	**Uncertainty range for Cr-doped UO_2 fuel**	**Uncertainty range for Zirlo cladding**
Thermal conductivity	±5%	±20%
Thermal expansion coefficient	±5%	±30%
Creep rate	0.5-10 (multiplication factor)	±50%
Density	±2%	No uncertainty applied
Elastic modulus	±30%	±5%
Poisson ratio	No uncertainty applied	±10%
Swelling	±20%	No uncertainty applied
Heat capacity at constant pressure	±5%	±5%
Yield stress	No uncertainty applied	±30%

For applying appropriate uncertainties of the material properties we have followed the same approach as in an earlier study of TRANSURANUS simulations [18] for one case of the IAEA Fumex-II project, that addressed the impact of U_3Si_2 fuel and FeCrAl cladding [19]. The uncertainties have been assumed to be uniformly distributed, with the associated ranges for the Cr-doped UO_2 fuel and the Zirlo cladding provided in Table 1. Note that in most cases there is not enough data available to derive mathematical distribution functions such as a Gaussian. The corresponding ranges are estimated from the experimental uncertainty on which the correlation for the property is derived, or on the basis of the range applied by Ikonen et al. [20] in their uncertainty and sensitivity analysis.

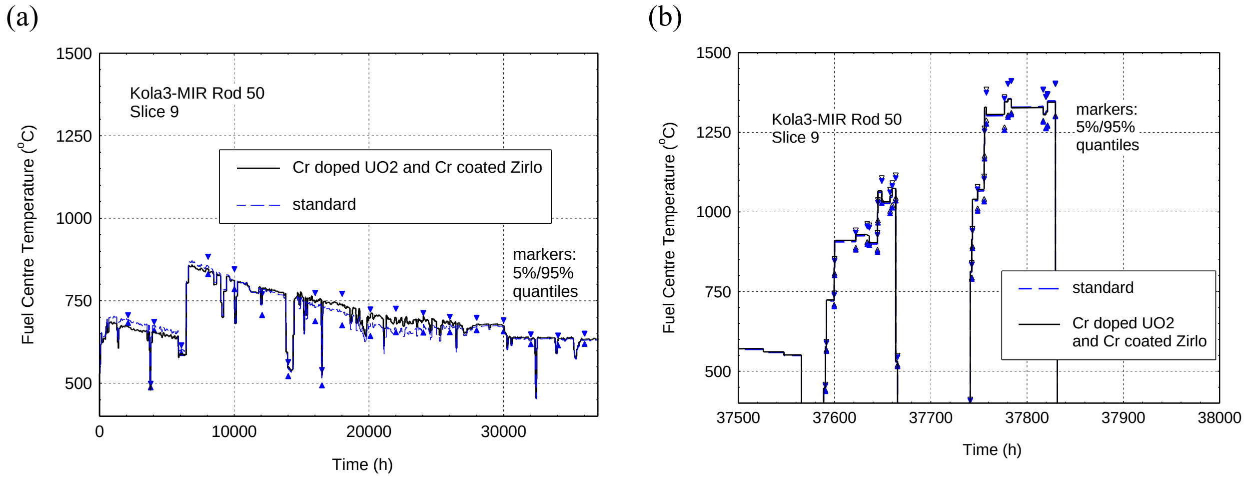

Figure 3. Time dependence of the (5%/95%) uncertainty intervals of the simulated fuel central temperature for (a) the base irradiation and (b) the correspondent ramp-tests of one WWER-440 fuel rod.

The impact of the parameter uncertainties on the simulated fuel central temperature is shown in Figure 3. More precisely, we show the best-estimate results along with the band associated with the 5%/95% confidence limit as a function of time. Despite the uniform distributions of the various material properties considered, the resulting central temperatures have a near-Gaussian distribution (not shown). Figure 3 underlines that the effect of applying a combination of all assumed ATF properties (Cr-doped UO_2 fuel with Zirlo cladding and Cr coating) is not larger than the 5%/95% confidence limits. During the simulated ramp tests, the analogous maximum impact on fuel centre temperatures is much smaller than the confidence band.

3.4 Fission gas release

In analogy to Figures 1 and 2, Figure 4 compares the simulated rod-integral fractional fission gas release for 6 different material configurations, starting from the standard UO_2 fuel and E110 cladding, and consecutively applying Cr-doped fuel, Zirlo cladding, a combination thereof, as well as the effect of the Cr coating (markers). In addition to these best-estimate results (as in Figure 3) the band associated with the 5%/95% confidence limit as a function of time is included.

Unlike for the fuel temperatures, the change from UO_2 fuel to Cr-doped UO_2 fuel leads to a significant decrease of the integral fission gas release. For both fuel types, the application of Zirlo instead of E110 cladding causes only a very moderate increase in the integrated fission gas release that can be linked to the slight increase in fuel temperatures for Zirlo claddings during the ramp phases (cf. Figure 2b).

As observed for gap sizes and fuel temperatures, applying Cr coating to either cladding type leads only to a very small additional change of the simulated fission gas release (full markers in Figure 4).

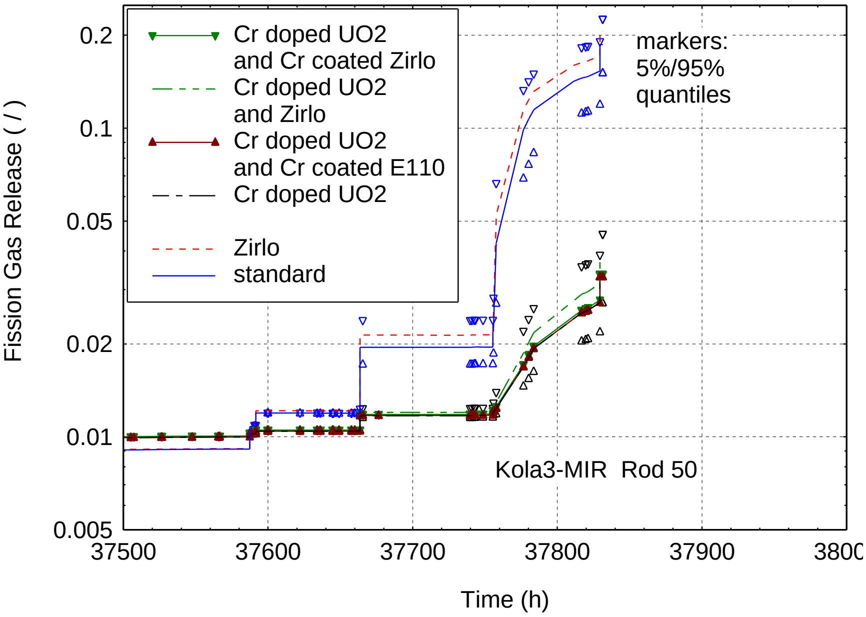

Figure 4. Dependence of the simulated integral fission gas release on the irradiation time for one ramp-tested WWER-440 fuel rod.

Additional sensitivity tests (not shown) have revealed that the large difference in initial grain size is the dominating reason for the decreased fission gas release at nearly identical fuel temperatures. This reasoning is confirmed by an analysis of the corresponding radial distributions of the simulated local Xe concentration at the end of the ramp tests (Figure 5).

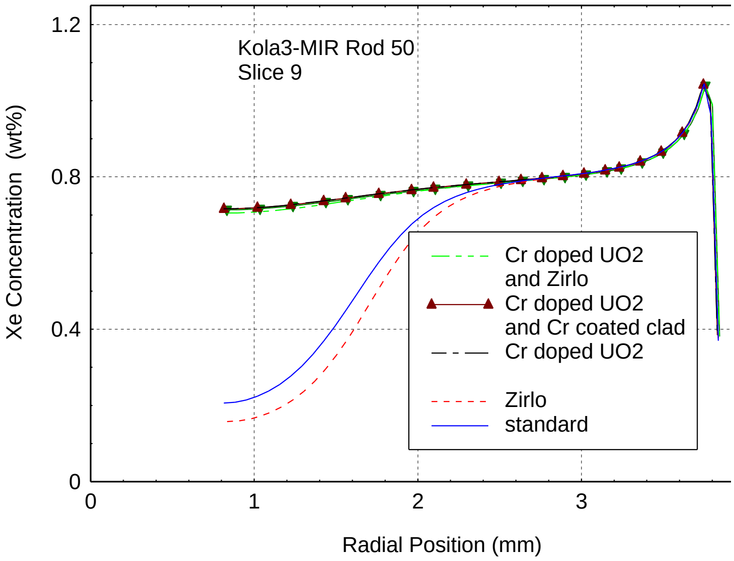

Figure 5. Dependence of the simulated final Xe concentration in the fuel grains on the radial position for one ramp-tested WWER-440 fuel rod.

3.4 Impact of ATF on a set of simulations

For 4 ramp-tested fuel rods of the KOLA-3-MIR experiment, i.e., rod #41, #48, #50, #51 as specified in [15,16], Figure 6 (generated with the new tool TuQuality) summarizes the impact of the addressed ATF material properties on simulated fuel centre temperatures and fission gas release.

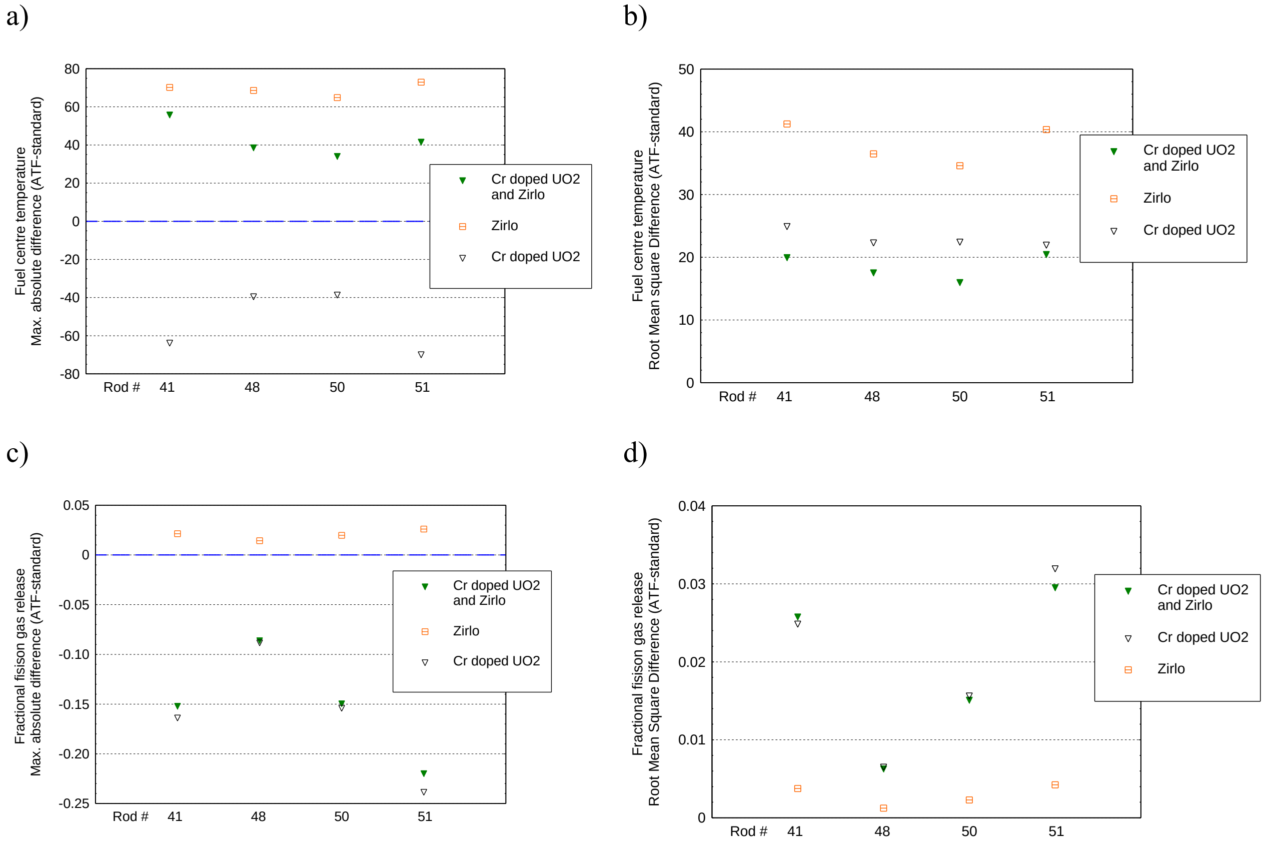

Figure 6. Max. impact of different ATF material properties on simulated fuel centre temperatures and fission gas release for 4 ramp-tested fuel rods of the KOLA-3-MIR experiment.

The figure covers the maximum observed difference as well as the root-mean-square difference for the complete history including base irradiations. The summary does not show the very small additional effect of the Cr coating (cf. above analysis of rod #50). Figure 6 confirms the similar behaviour of the 4 fuel rods analyzed, i.e. an acceptable change in fuel centre temperatures for all addressed types of ATF (max. +/- 80 deg, rms < 45 deg), and a significant decrease of the integral fission gas release, mainly because of the larger grain size caused by Cr doping in UO_2 fuel.

3.5 Sensitivity analysis of fission gas release

The graphical interface TUPython allows for making correlation and sensitivity analyses by evaluating e.g. Pearson correlation coefficient and Spearman’s rank coefficient. The Pearson’s or simple correlation coefficient (SCC) of output quantity y related to input quantity x, is defined as

$$SCC = \frac{\sum_{i=1}^{n}(x_i - \bar{x})(y_i - \bar{y})}{\sqrt{\sum_{i=1}^{n}(x_i - \bar{x})^2}\sqrt{\sum_{i=1}^{n}(y_i - \bar{y})^2}}$$

As an example, the evolution of Pearson's coefficients of sensitivity for the integral fission gas release of Cr-doped UO_2 with Zirlo cladding for rod #50 is shown in Figure 7. It is interesting to note that the impact of the fuel density and cladding thermal strain is more pronounced during the first ramp, whereas the impact of the fuel thermal conductivity becomes dominant during the 2nd ramp. The main reason should be the high fuel temperature that is further increasing with the onset of thermal feedback from fission gas release. These causalities should however be addressed in more detail. The present analysis also underlines the need for considering additional input uncertainties, e.g. a distribution of the initial grain size.

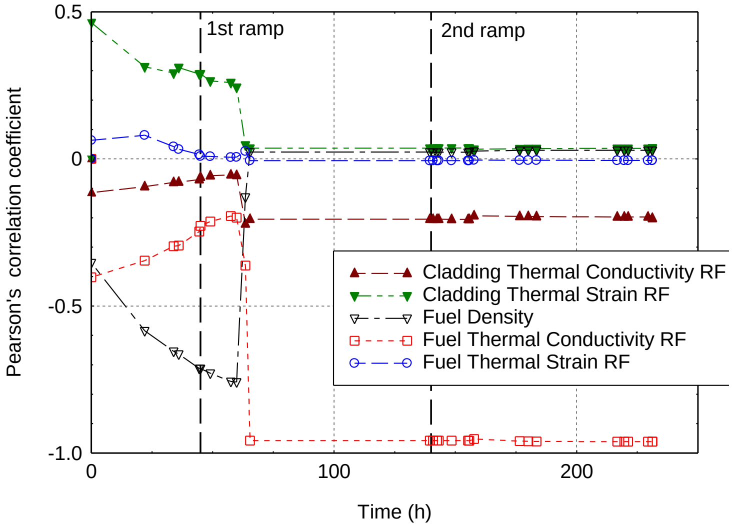

Figure 7. Pearson's coefficients for correlations between simulated fission gas release and applied material properties (fuel and cladding) – dependence on the irradiation time for one ramp-tested WWER-440 fuel rod.

4. Summary and outlook

The impact of Cr-doped UO_2 fuel and Zirlo cladding, together with Cr coating of the cladding surface, on WWER-type UO_2 fuel was investigated by simulating four irradiation experiments incl. ramp tests from the IAEA Fumex-III project. The analyses covered fuel-to-cladding gap sizes, fuel centre temperatures, the integral fission gas release as well as the final radial profiles of the local Xe concentration. The results are consistent with those published earlier in the frame of the APIS project but show in more detail the impact on fission behaviour in doped fuels with larger grains and initial density.

The evolution of the fuel-to-cladding gap size during base irradiation of the different ATF configurations can be consistently explained by differences in fuel densification and cladding creep and leads to moderate changes in fuel centre temperatures (max. +/- 80 deg, rms < 45 deg). While the impact on fuel temperatures during the ramp tests is very small, the application of Cr-doped UO_2 fuel causes a significant decrease of the integral fission gas release that is mainly due to the larger initial grain sizes.

These findings are in line with an uncertainty analysis, assuming uniform distributions of fuel and cladding material properties, and determining the 5%/95% confidence limits in simulated fuel temperatures and fission gas release. When applying Cr coating to either E110 or Zirlo cladding, only very small additional changes can be observed in all analyzed output quantities. The simulated performance of ATF fuel rods thus meets expectations when compared to the standard options, especially the reduced fission gas release during the ramp tests. A sensitivity analysis of fission gas release using Pearson's correlation coefficients demonstrates the consistency of the TRANSURANUS fuel performance simulations while confirming the need for further options for uncertainty input and postprocessing.

Acknowledgement

This work has received funding from the Euratom research and training programme 2021–2027 through the OperaHPC project under grant agreement n° 101061453, as well as from the APIS project (https://apis-project.eu/) under grant agreement n° 101114673.

Co-funded by the
European Union

References

[1] G. Nicodemo, G. Zullo, F. Cappia, P. Van Uffelen, A. De Lara, L. Luzzi, D. Pizzocri, Chromia-doped UO2 fuel: An engineering model for chromium solubility and fission gas diffusivity, Journal of Nuclear Materials 601 (2024) 155301.

[2] A. de Lara, P. Van Uffelen, G. Nicodemo, G. Zullo, D. Pizzocri, E. Shwageraus, Consideration of Cr-doped UO2 fuel performance for a Fluoride-Cooled High Temperature Reactor concept, Annals of Nuclear Energy 209 (2024) 110820.

[3] P. Aragón, F. Feria, L. E. Herranz, A. Schubert, P. Van Uffelen, Fuel performance modelling of Cr-coated Zircaloy cladding under DBA/LOCA conditions, Annals of Nuclear Energy 211 (2025) 110950.

[4] A. de Lara, X. Ha Nguyen, P. Van Uffelen, E. Shwageraus, Comparison of Advanced-Technology-Fuel options in soluble boron-free Small Modular Reactors, Annals of Nuclear Energy 218 (2025) 111355.

[5] G. Robertson, H. Sjöstrand, P. Andersson, A. Göök, P. Blair, Addressing model inadequacy in fuel performance model calibration using MH-within-Gibbs sampling, in: Best Estimate Plus Uncertainty International Conference (BEPU 2024) (Nuclear and INdustrial Engineering (NINE), Lucca, Italy, 2024) paper 311.

[6] G. Robertson, H. Sjöstrand, P. Andersson, A. Göök, P. Blair, Model Inadequacy in Fuel Performance Code Calibration: Derivative-Based Parameter Uncertainty Inflation, Annals of Nuclear Energy submitted (2024).

[7] G. Robertson, H. Sjöstrand, P. Andersson, J. Hansson, P. Blair, Treating model inadequacy in fuel performance model calibration by parameter uncertainty inflation, Annals of Nuclear Energy 179 (2022) 109363.

[8] International Fuel Performance Experiments (IFPE) Database, in: (OECD-NEA, Nuclear Science Working Party on Scientific Issues of Reactor Systems, 2018).

[9] M. Oguma, Cracking and Relocation Behavior of Nuclear Fuel Pellets During Rise to Power, Nuclear Engineering and Design 76 (1983) 35.

[10] J. Sanchez-Torrijos, A. Soler, E. Castro, J. Perez-Fresno, "Assessment of the potential benefits derived from the simulation of different evolutionary ATF materials under LOCA conditions (IFA 650.10)", Proceedings of Conference on Reactor Fuel Performance - TopFuel 2024, ENS, Grenoble, France, 29 September - 3 October.

[11] A. R. Massih, "Effects of additives on uranium dioxide fuel behavior", in, 2014:21, Swedish Radiation Safety Authority (SSM), Uppsala, Sweden, 2014.

[12] M. W. D. Cooper, C. R. Stanek, D. A. Andersson, The role of dopant charge state on defect chemistry and grain growth of doped UO2, Acta Materialia 150 (2018) 403.

[13] K. J. Geelhood, W. G. Luscher, L. Kyriazidis, C. E. Goodson, J. Corson, J. J. Whitman, D. F. Wray, "MatLib-1.2.1: Nuclear Material Properties Library", in, PNNL, 2024.

[14] P. Aragon Grabiel, Implementation of dynamic nuclear fuel thermo-mechanics in transient simulation of lead-cooled reactors, Master thesisBarcelona School of Industrial Engineering, 2021.

[15] "Improvement of computer codes used for fuel bevaiour simulation (FUMEX-III), Report of a coordinated research project", in: IAEA-TECDOC-1697, Vienna, 2013.

[16] S. Boneva, "The priority cases of the Fumex-III exercise simulated with the Transuranus code", INRNE (Ed.), Proceedings of 9th International Conference on WWER Fuel Performance, Modelling and Experimental Support, Helena Resort, Bulgaria, 17 - 24 September p. 350.

[17] D. Elenkov, S. Boneva, M. Georgieva, S. Georgiev, K. Lafchiev, Analysis of the KOLA3-MIR transient experiment with the Transuranus code, in: INRNE (Ed.), 8th International Conference on WWER Fuel Performance, Modelling and Experimental Support (INRNE, Helena Resort, Bulgaria, 2009) 509.

[18] P. Van Uffelen, A. Schubert, Z. Soti, Assessing the effect of some ATF materials and uncertainties on their properties under normal operation conditions by means of the TRANSURANUS code in: Pacific Basin Nuclear Conference 2022 (CNS, Chengdu, P.R. China, 2022).

[19] "Fuel Modelling at extended burnup (FUMEX-II), Report of a coordinated research project", in: IAEA-TECDOC-1687, Vienna, 2011.

[20] T. Ikonen, V. Tulkki, The importance of input interactions in the uncertainty and sensitivity analysis of nuclear fuel behavior, Nuclear Engineering and Design 275 (2014) 229.

Fuel Assembly Bow DNBR Penalty for VVER-1000 reactors

Tommaso Carnicella[1*], **Akif Abdullayev**[1] **and Ulf Lindelöw**[1]

[1]*Westinghouse Electric Company, Sweden, Västerås, 72136.*

[*]E-mail: *Tommaso.Carnicella@westinghouse.com*

Abstract. Fuel assembly bowing is a phenomenon characterized by the axial bending of the fuel assembly. A direct consequence of this deformation is the variation of the inter-assembly gap, which exposes the peripheral region of the fuel assembly to over-moderated or under-moderated conditions. This leads to two distinct effects: an increase in the relative power of the peripheral rods facing the bowed region and an increase in coolant flow rate in the affected areas. The present analysis combines the effects of these two phenomena in order to evaluate the impact on the Departure from Nucleated Boiling (DNBR) for the peripheral subchannels, and consequently the impact on the allowable enthalpy rise factor for the peripheral rods.

The evolution of the inter-assembly gap is a complex process, influenced by overall core distortion, fuel assembly design, burnup history, and core location. Although the enthalpy rise factor tends to decrease with increasing burnup, a fixed value has been conservatively adopted. The Westinghouse thermal-hydraulic subchannel analysis code VIPRE-W was employed. The full-core homogeneous model of the VVER-1000 reactor was discretized into 208 subchannels, with a finer radial decomposition applied in the region between the hottest fuel assemblies. Adjacent regions were also subdivided into subchannels to ensure accurate predictions for the first and second rows of fuel rods, with mesh resolution progressively reduced further from the region of interest. The impact of inter-assembly gap variation is assessed by introducing penalties on the enthalpy rise factor. These penalties are derived by translating the margin between the DNBR and its design limit (DL-DNBR, Reference [1]) into an equivalent power increase. Based on the results, penalties have been quantified for the peripheral rods in the first and second rows, accounting for the combined effect of thermal-hydraulic behaviour and local power peaking induced by the increased inter-assembly gap.

1. Introduction

The axial deformation of the fuel assembly is a direct consequence of multiple interacting phenomena occurring during reactor operation. The magnitude of bowing is strongly dependent on the specific operating conditions within the core. A large assembly bow can increase inter-assembly gap, potentially leading to elevated power levels in peripheral fuel rods, which may compromise fuel operational reliability and safety. Therefore, a dedicated analysis is required to address this issue. To perform such analysis and implement preventive measures, accurate knowledge of the in-core gap distribution is a fundamental input.

Identifying the in-core gap distribution resulting from the assembly bow remains a significant challenge. Currently, no hardware or software solutions are available that can accurately quantify the inter-assembly gap distribution in VVER reactors.

The present work provides a description of methodology used to evaluate implications of increased inter-assembly gap on the core parameters, and account for the effects on the DNBR for normal operating conditions. The attention has been focused on the peripheral rods, located in the side and in the corner of the fuel assembly (See Figure 1), which are the ones exposed to over-moderation. In particular, the ones located in the side and in the corner of the fuel assembly, have been chosen as hot reference rods to quantify the impact on the DNBR.

Thermal-hydraulic analyses were performed using VIPRE-W, the Westinghouse version of the EPRI subchannel analysis code (Reference [2]), specifically adapted for VVER licensing applications and equipped with DNB correlations tailored to VVER-1000 fuel designs (Reference [3]).

Penalties to be applied in addition to the nominal uncertainties when operating with bowed assemblies were calculated. These penalties have been determined on a cycle-independent and gap distribution-independent basis. This analysis is based on the assumption of a predefined maximum inter-assembly gap of 12 mm.

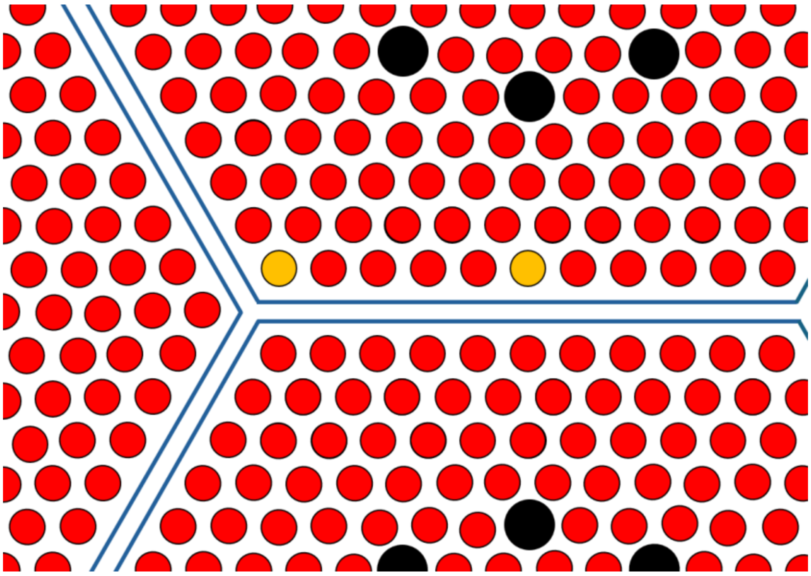

Figure 1. Illustration of peripheral regions of three fuel assemblies. In yellow, the corner and side peripheral hot rods.

2. Inputs, model and assumptions

This section explains the main assumptions, the boundary conditions adopted and the VIPRE-W model used for performing the calculations.

2.1 Inputs: increase of peaking factors for peripheral rods

The increase in power peaking factors has been derived from Monte Carlo mini-core simulation performed using MCNP (Reference [4]). The mini-core consists of 19 fresh assemblies (

Figure **2** (A)) modeled reducing the concentration of boric acid to a value of 80% with respect to the one that is usually adopted in VVER-1000 at beginning of cycle with Xenon in equilibrium. This assumption is conservative and results in a significant overestimation of both local and integral power increases due to the enlarged inter-assembly gap. In the mini-core model, fuel assemblies are intentionally displaced to simulate increased inter-assembly gaps, affecting side and corner rods.

The increased in the enthalpy rise factors ($F_{\Delta H}$) for the first and second rows of peripheral rods is expressed as function of:

- 1-sided gap - distance along the normal between opposite faces of adjacent assemblies; this parameter defines changes in fuel rod local power for peripheral side fuel rods row (Figure 2 (B)).
- 2-sided gap - sum of two distances along the normal between opposite faces of two adjacent assemblies; this parameter defines changes in fuel rod local power for peripheral corner fuel rod (Figure 2 (C)).

The increase of enthalpy rise factors as a function of the gap for the first and second rows of side and corner rods are plotted in Figure 3 and Figure 4.

.

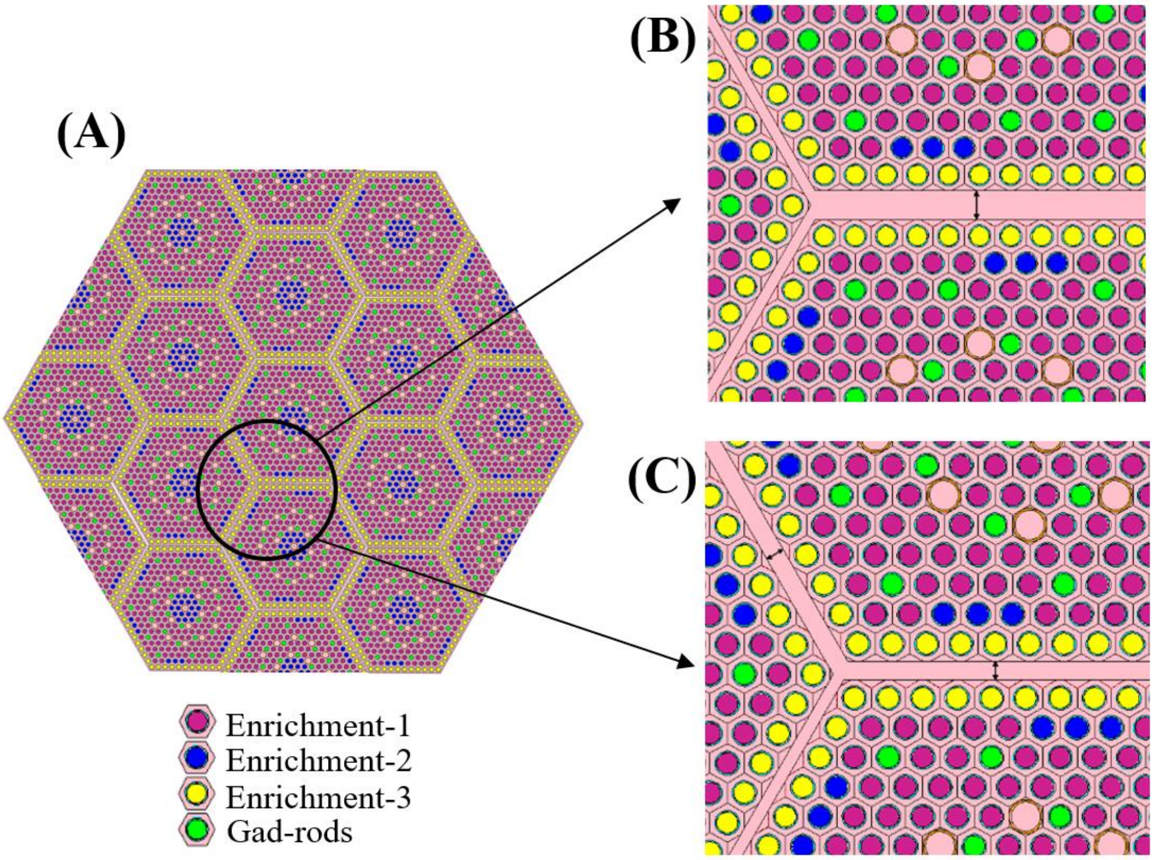

Figure 2. Layout of 19 assemblies mini-core (A) and reference displacements for peripheral side rods with 1-sided gap (B) and peripheral corner rods with 2-sided gap (C).

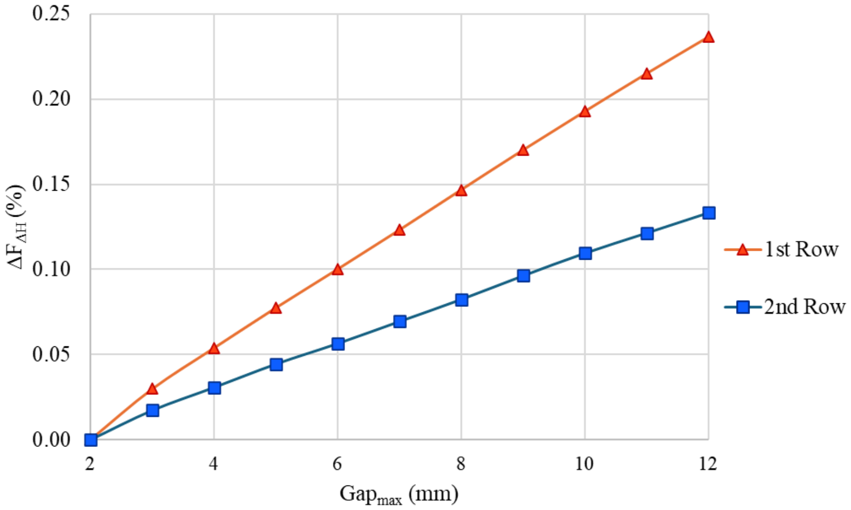

Figure 3. Increase of enthalpy rise factor as function of maximum gap, for 1st and 2nd row of peripheral side rods.

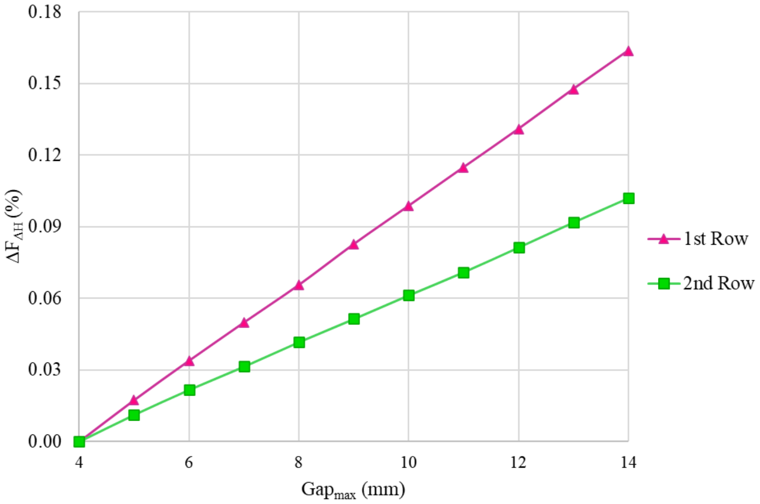

Figure 4. Increase of enthalpy rise factor as function of maximum gap, for 1st and 2nd row of peripheral corner rods.

2.2 MODEL- 208-Channels VIPRE-W Model

A dedicated VIPRE-W model consisting of 208 channels was developed to simulate the thermal-hydraulic behaviour of peripheral hot channels in the core with particular interest on DNB. The model focuses on regions between the three hot fuel assemblies where the peak power rods are expected to occur due to inter-assembly gap openings, particularly at the side and corner locations of the hot fuel assemblies.

To ensure accurate DNBR predictions, a detailed mesh was applied in the region of interest, surrounding the hot channels with adjacent subchannels (Figure 5). This approach allows for fine resolution where needed, while maintaining computational efficiency in the rest of the core, which is modeled with a coarser mesh (Figure 6).

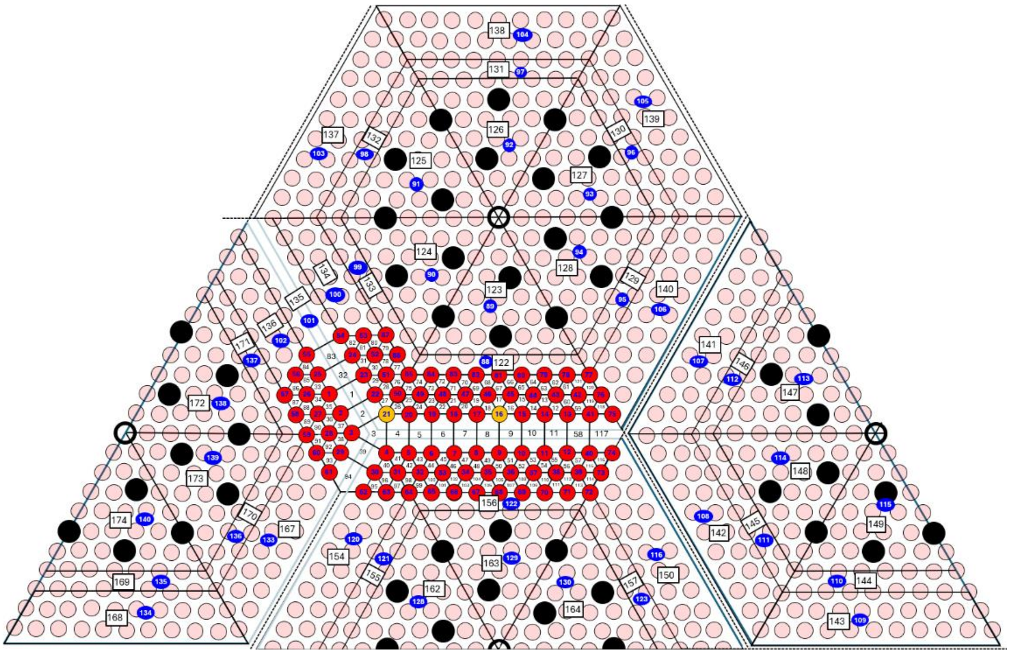

Figure 5. VIPRE-W 208-channels model for VVER-1000 reactor: region of interest.

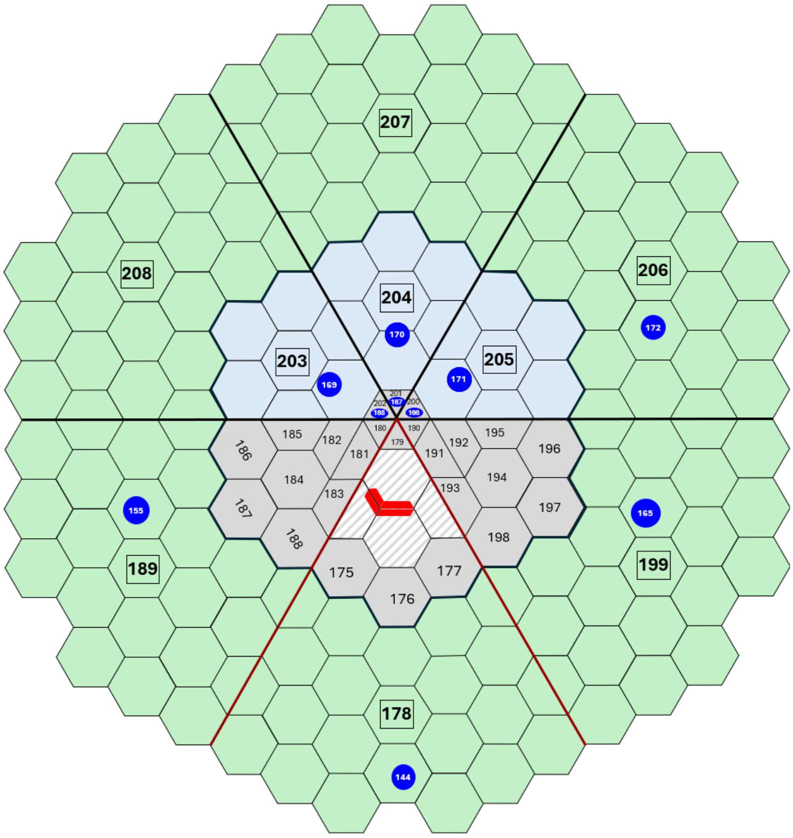

Figure 6. VIPRE-W 208-channels model for VVER-1000 reactor: full core.

The model incorporates axial variations in the geometry of inter-assemblies channels to account for assembly bow effects. Specifically, changes in channel area, hydraulic diameter, and gap width are introduced as a function of axial position. The axial gap shape is assumed to follow a cosine distribution, with the maximum gap located at the centre of the active length of the fuel assembly.

The described model was employed for a preliminary analysis where several Critical Heat Flux (CHF) correlations have been used in order to identify the most limiting channels which can be used as reference channels for DL- DNBR and DNBR analysis with fuel assembly bow.

The results identified channels 17 and 66 as representative for 1st and 2nd row for the side case. For the peripheral corner subchannels, channels 26, 28, and 75 were selected: channel 26 represents the 1st row, while channels 28 and 75 represent the 2nd row.

2.3 Assumptions

The analysis follows the Revised Thermal Design Procedure (RTDP), as described in Reference [1]. This is a standard methodology applied by Westinghouse for both PWR and VVER reactors. In this approach, uncertainties in thermal-hydraulic parameters are statistically combined with uncertainties in DNB correlations to define the Design Limit DNBR (DL-DNBR).

The CHF correlation used in the analysis was developed and validated for the specific fuel design considered, based on dedicated test data (Reference [5]). It accounts for both mixing vane and non-mixing vane regions.

The evaluation was conducted considering the side case (only 1 side of the hot assembly faces the increase of the gap) and the corner case (2 sides of the hot assembly face the increase of the gap).

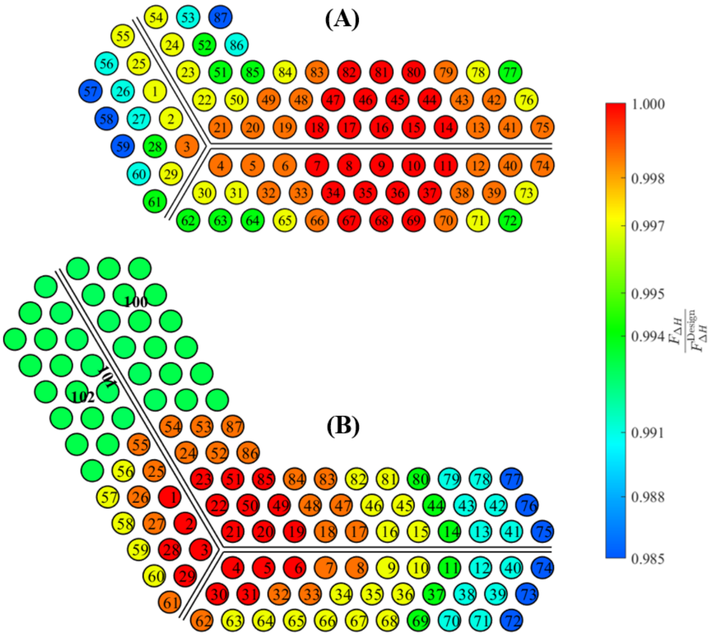

Figure 7. Reference normalized enthalpy rise factor adopted for side (A) and corner case (B).

The design enthalpy rise factor ($F_{\Delta H}^{Design}$) was adopted as the reference for all scenarios[1]. The reference distribution of rods relative power in the region of interest is shown in Figure . In all cases, the relative power of hottest fuel assemblies is kept equal, corresponding to $F_{\Delta H}^{Design}/1.04$.

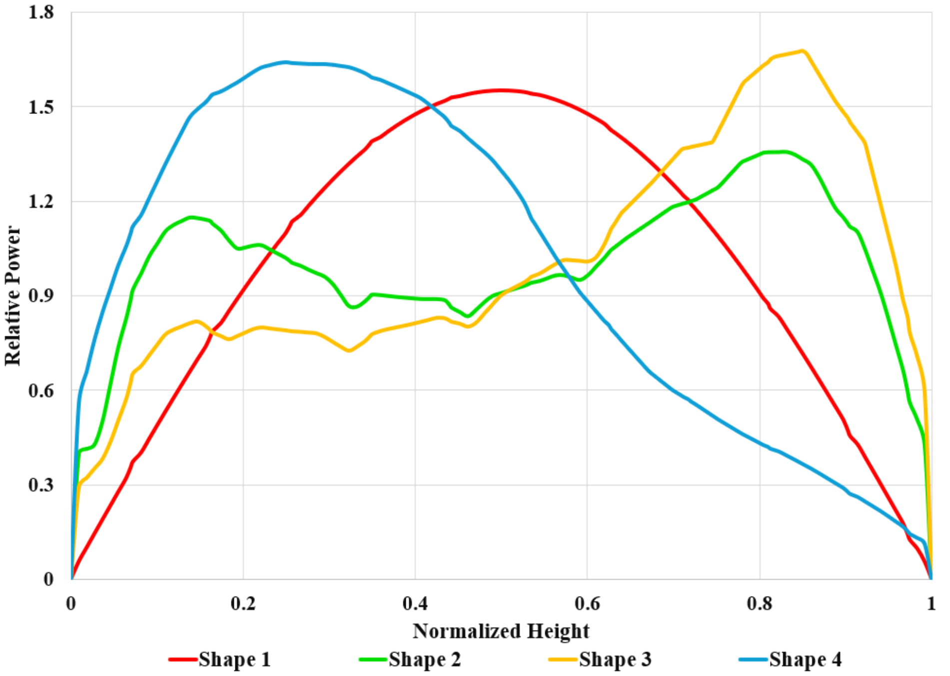

Figure 8. Axial power profiles adopted.

Table 1. *Replace Operational scenarios and relative power shapes adopted.*

Case Number	Condition	Power Shape
1	Low Power High Pressure (LPoHPr)	Shape 1
2	High Power High Pressure (HPoHPr)	Shape 1
3	Low Power Low Pressure (LPoLPr)	Shape 1
4	High Power Low Pressure (HPoLPr)	Shape 1
5	Low Flow (60% flow reduction)	Shape 2
6	Drop Rod	Shape 2
7	Static Rod Misalignment	Shape 2
8	High Power Low Pressure with High Axial Offset	Shape 3
9	High Power Low Pressure with Low Axial Offset	Shape 4
10	Nominal	Shape 1

---

[1] Only the Static Rod Misalignment event presents power factor 31.5% higher than the design value.

A total of 10 operational scenarios were defined by varying system pressure, inlet coolant temperature, inlet flow rate, core thermal power, and axial power shape (Figure 8). These scenarios were analysed to identify the most limiting condition with respect to DNB. There reactor conditions and relative axial power shapes adopted are listed in Table 1.

3. Methodology

This section presents the methodology specifically developed to calculate the penalties related to the enthalpy rise factor ($\delta_{F\Delta H}$) for the first and second rows of fuel rods. These penalties are a function of the DNBR variation caused by the fuel assembly bow effect.

The methodology consists of the following steps:

1. DL-DNBR calculations: for side and corner cases DL-DNBR has been evaluated for the 10 operational scenarios keeping the inter-assembly gap constant and equal to 2 mm.
2. Evaluation of DNBR considering fuel assembly bow phenomena: performed by increasing gap at step of 1 mm and simultaneously increasing the $F_{\Delta H}$ related the first and second rows of rods.
3. Evaluation of DNBR variation with the $F_{\Delta H}$: calculation of the DNBR derivative with the enthalpy rise factor (∂ DNBR^{bow}/ ∂ $F_{\Delta H}$).
4. Conversion of the derivative into a power margin ($\Delta F_{\Delta H}$).
5. Calculation of the allowed enthalpy rise factor ($F_{\Delta H}{}^{A}$).
6. Evaluation of the corrective enthalpy rise factor penalty ($\delta_{F\Delta H}$) for those cases where the design limit is violated.

3.1 Design Limit DNBR analysis

The calculated DL-DNBR is used in safety analyses as a criterion to demonstrate the absence of DNB with 95/95 confidence for the limiting rods during normal operation and Condition II transients.

The DL-DNBR has been evaluated for both side and corner cases, focusing on the channels located at the periphery of the assembly. For each case, 10 operational conditions were investigated, with particular attention to reference channels in the 1st and 2nd row of rods (see Section 2.2), in order to identify the most limiting conditions. The evaluation follows the Revised Thermal Design Procedure (RTDP), in which the DL-DNBR is determined by statistically combining uncertainties in thermal-hydraulic parameters and DNB correlations, as prescribed by the methodology. Specifically, the uncertainties considered include core flow rate, core power, pressurizer pressure, core inlet temperature, design enthalpy rise factor ($F_{\Delta H}{}^{Design}$), and engineering enthalpy rise factor ($F_{\Delta H}{}^{E}$). This ensures that the DL-DNBR reflects conservative limits under realistic operating conditions.

The radial power distribution adopted for this set of analysis is shown in Figure 7.

Due to the lack of statistical data on inter-assembly gap distribution and the associated local power increase, the DL-DNBR for side and corner rods is calculated keeping the inter-assembly gap constant and equal to 2 mm, which correspond to the reference nominal value.

3.2 Calculation of DNBR with assembly bow phenomena

The inter-assembly gap was progressively enlarged in 1 mm steps, leading to a corresponding increase in the enthalpy rise factor, as shown in Figure 9 (side case) and in Figure 10 (corner case). This process was carried out for each of the 10 scenarios across both cases.

The axial variation of the inter-assembly gap was accounted for by adjusting the flow area, gap size, and the wetted and heated perimeter of the inter-assembly channels as a function of axial position. A cosine-shaped axial bending profile was adopted for this analysis, ensuring that the gap at the extremities of the assembly's active length remained constant at 2 mm for all gap distributions considered.

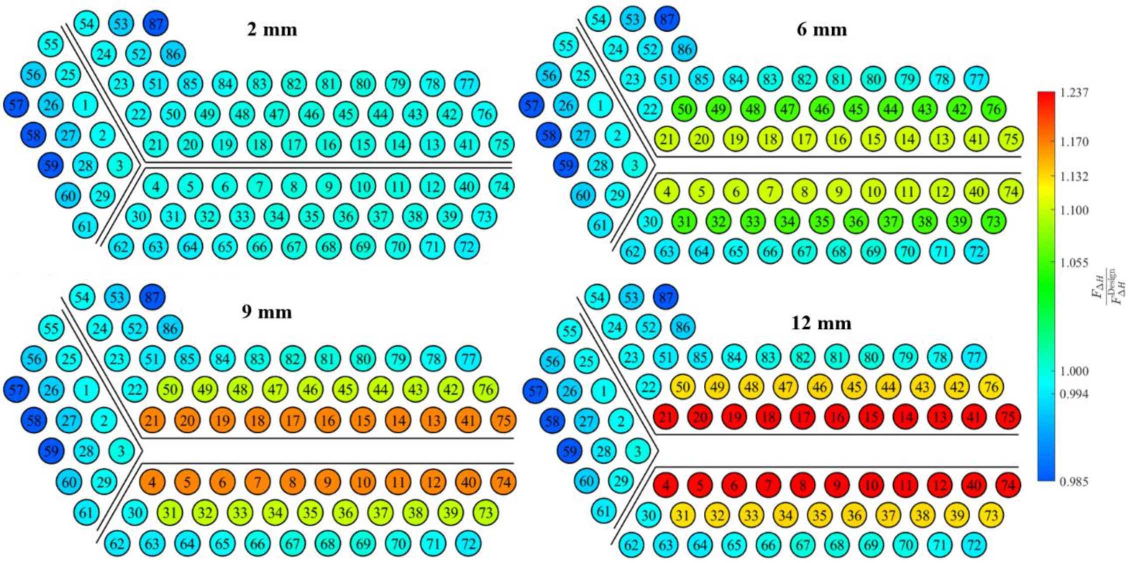

Figure 9. Increase of enthalpy rise factor to respect the design value as function of inter-assembly gap for side case

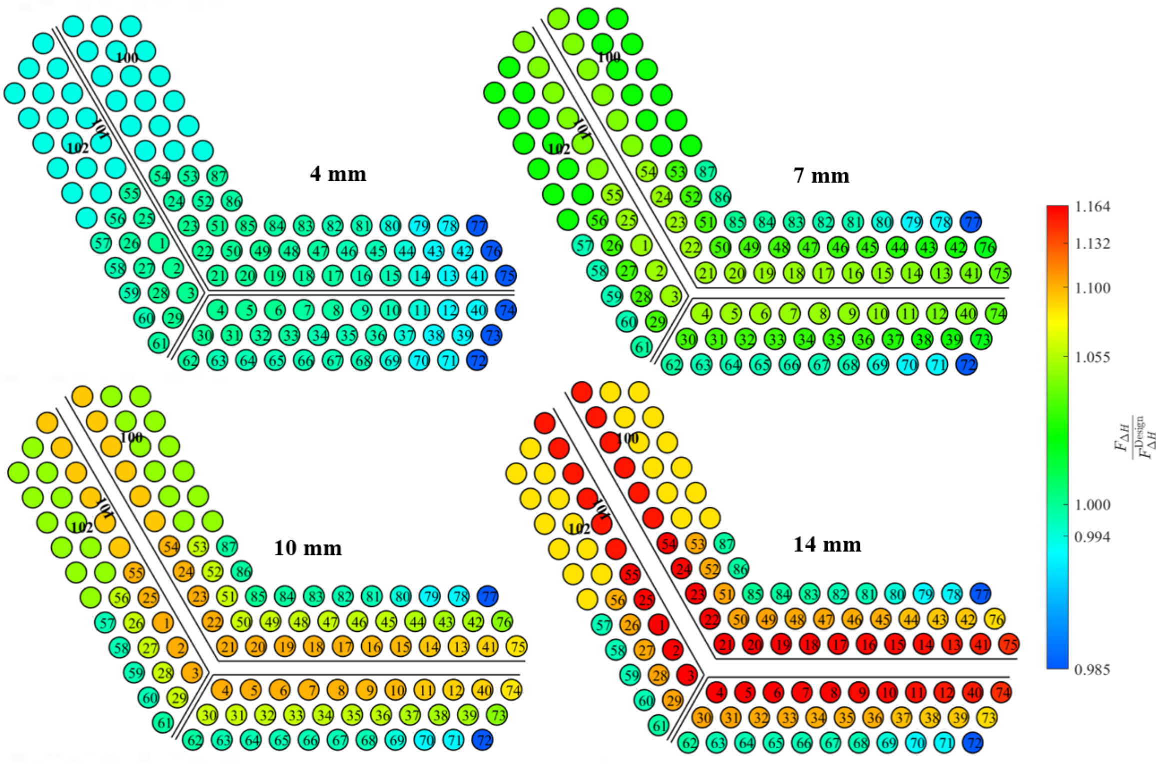

Figure 10. Increase of enthalpy rise factor to respect the design value as function of inter-assembly gap for corner case.

The DNBR evaluated under fuel assembly bow conditions was then normalized with respect to the corresponding DL-DNBR, which represents the threshold below which corrective penalties are required. For each value of inter-assembly gap g, the normalized DNBR* is evaluated as follows:

$$DNBR^*_{i,j}(g) = \frac{DNBR^{bow}_{i,j}(g)}{DL\text{-}DNBR_{i,j}} \qquad (1)$$

where i denotes operational condition and j the case.

The use of DNBR* allows for a rapid assessment and identification of the conditions that violate the DL-DNBR, i.e. when it is falls below 1.

The variation of DNBR* as function of the maximum inter-assembly gap for the 10 cases is represented for side case in Figure 11 and Figure 12, valid for channel 17 (1st row) and channel 66 (2nd row), respectively.

Those plots show violations for maximum inter-assembly gap of 11 mm and 12 mm.

The variation of DNBR* as function of the maximum inter-assembly gap for the 10 cases is represented for corner case in Figure 13 valid for channel 26 (1st row) and channels 28 and 75 (2nd row).

The plots indicate that no violations occur for the inter-assembly gaps considered in corner cases, and consequently, no penalties are applied.

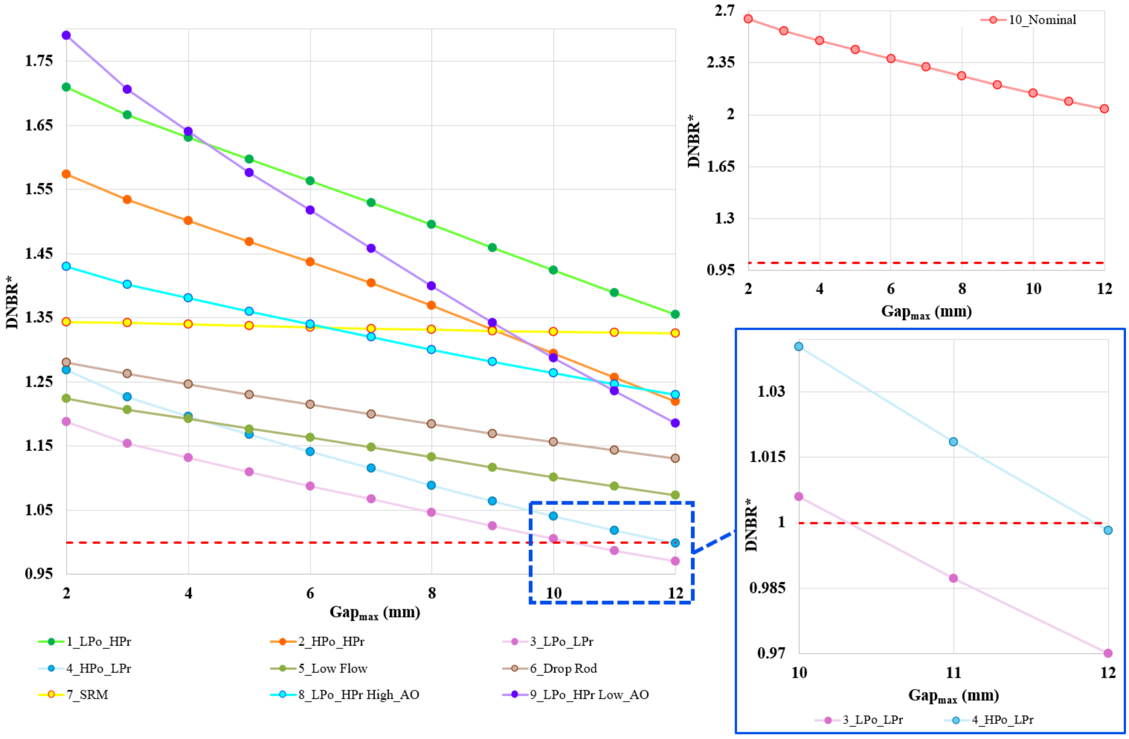

Figure 11. Trend of DNBR* as function of the maximum inter-assembly gap for 1st row (Channel 17) in side case.

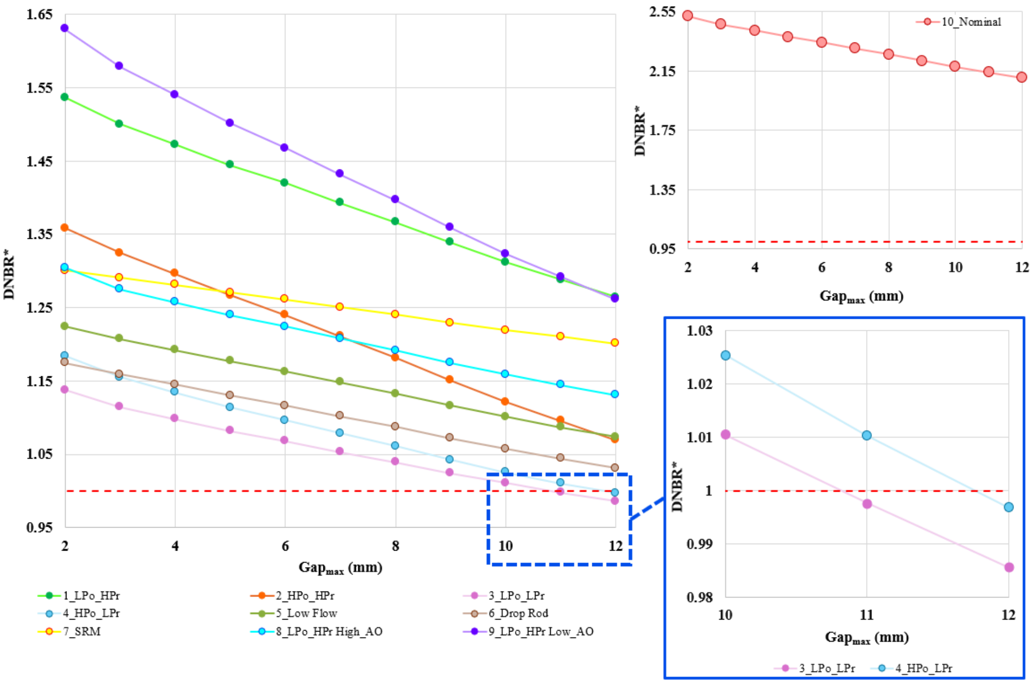

Figure 12. Trend of DNBR* as function of the maximum inter-assembly gap for 2nd row (Channel 66) in side case.

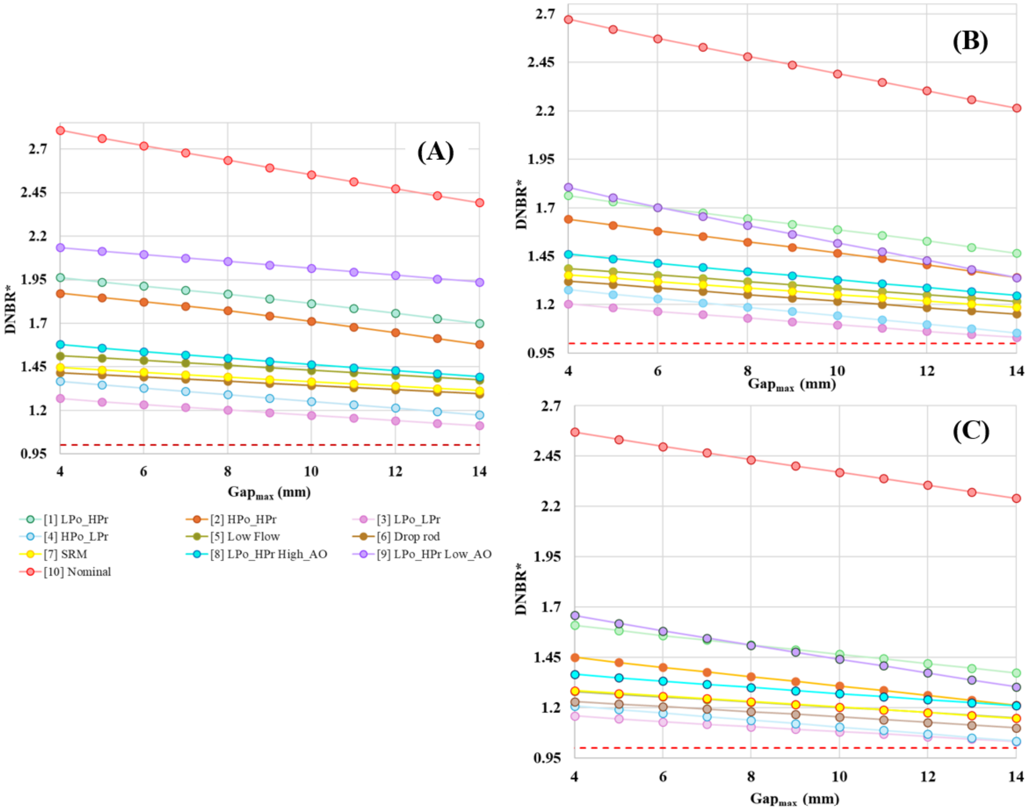

Figure 13. Trend of DNBR* as function of the maximum inter-assembly gap for 1st row (Channel 26, (A)) and 2nd row (Channels 28 (B) and 75 (C)) in corner case.

3.3 Evaluation of enthalpy rise factor penalties

The core of the methodology is based on calculating the derivative of DNBR with respect to $F_{\Delta H}(g)$, $\partial\, DNBR^{bow} / \partial\, F_{\Delta H}$, which will then be converted into an enthalpy rise factor penalty, $\delta_{F\Delta H}$.

The derivative is evaluated for every gap distribution, for both the corner and side cases considering the 10 operational scenarios defined in Section 2.3.

This term is then used to calculate the power margin as follows:

$$\Delta F_{\Delta H\ i,j}(g) = \frac{\text{DL-DNBR}_{i,j} - \text{DNBR}_{i,j}^{bow}(g)}{\dfrac{\partial\, \text{DNBR}_{i,j}^{bow}(g)}{\partial\, F_{\Delta H}(g)}}. \qquad (2)$$

The allowed peaking factor is then evaluated as:

$$F_{\Delta H}^{A}(g) = F_{\Delta H}^{Design} + \Delta F_{\Delta H\ i,j}(g). \qquad (3)$$

As explained previously, if $DNBR^{*} \geq 1$, there is no violation on the DL-DNBR. In this case, the allowed $F_{\Delta H}{}^{A} \geq F_{\Delta H}{}^{Design}$.

If $DNBR^{*} < 1$, then allowed $F_{\Delta H}{}^{A} < F_{\Delta H}{}^{Design}$ and the relative peaking factor penalty ($\delta_{F\Delta H}$) is calculated as:

$$\delta_{F\Delta H} = \frac{F_{\Delta H}^{Design}}{F_{\Delta H}^{A}(g)} - 1. \qquad (4)$$

4. Results and discussion

The results of the calculations performed using the procedure described in the previous section show that, for inter-assembly gap increases up to 10 mm, the DNBR remains above the DL-DNBR threshold. This indicates that no peaking factor penalty needs to be applied.

However, for gap increases beyond 10 mm, a penalty must be applied to side rods due to violation of the DL-DNBR criterion under low-pressure and low power (LPoLPr) as well as low-pressure and high power (LPoHPr) cases.

The final penalties assigned for each gap are bounding the penalties calculated for all scenario analysed.

The required penalties for the peripheral rods, related to the 1st and the 2nd row, presented in Figure 14, are:

- For a maximum gap of 12 mm and 11 mm, penalties of 3.43% and 1.43% respectively, shall be applied to the $F_{\Delta H}$ of the peripheral rods.
- For the second row of rods, the corresponding penalties are 1.87% and 0.77% for a maximum gap of 12 mm and 11 mm, respectively.

As explained in the previous Section, only the side case presents violations which require corrective penalties for the peaking factors. The corner case does not present violations so, there is no need to apply penalties.

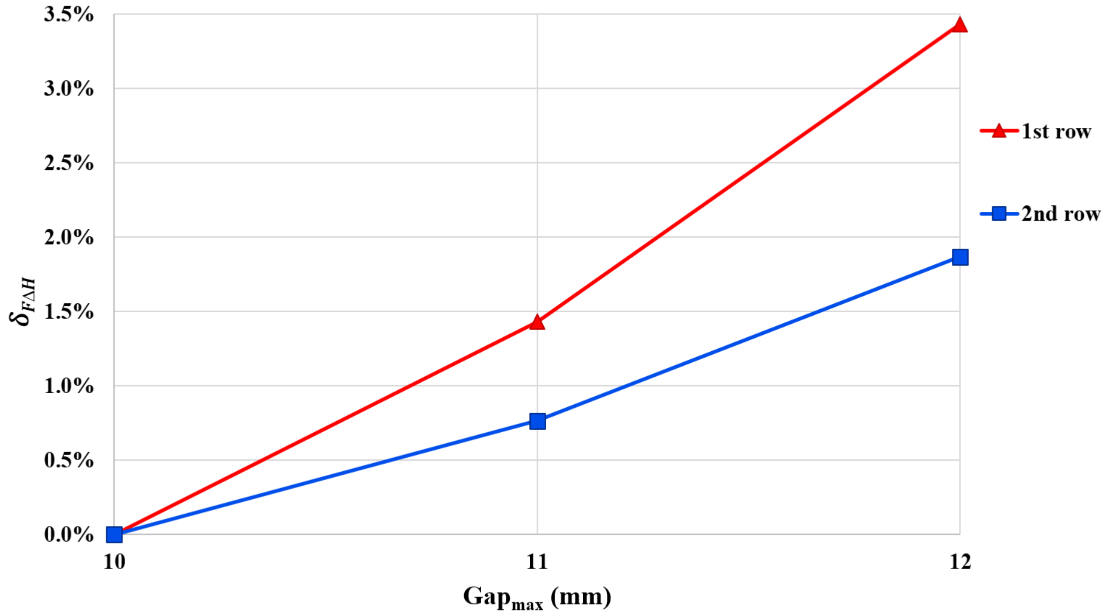

Figure 14. $F_{\Delta H}$ penalties due to fuel assembly bow for side rod related to 1st and 2nd row of rods.

5. Conclusion

The bowed fuel assemblies result in variable inter-assembly pitch across the core, affecting local water moderation and, consequently, the power distribution.

Due to the absence of statistical data on inter-assembly gap distributions, this parameter could not be incorporated into the Design Limit DNBR (DL-DNBR) analysis, which hence does not account for the effects of assembly bow. As a result, the associated penalties were evaluated using a deterministic approach, considering a wide range of gap values to conservatively cover all potential situations.

The change in peaking factors due to assembly bow has been evaluated using a conservatively designed mini-core, composed of the most reactive assemblies from an equilibrium fuel cycle representative of a generic VVER-1000 core. A C-shaped axial bending profile is assumed, representing the maximum bow magnitude and associated local power increase. An inter-assembly gap of 12 mm is used as a bounding value.

A set of penalties on peaking factors has been defined for both normal operation and Condition II transients. These penalties are independent of the fuel cycle and gap distribution, meaning they remain applicable to any future core reload at the plant, provided that the bounding conditions, specifically the maximum inter-assembly gap and its correlation with peaking factor increase, are respected.

These penalties are not intended to be retroactively applied to standard design results based on uniform gap models. Instead, they should be incorporated during the nuclear design phase for cycle-specific core configurations to account for the effects of assembly bow.

To validate the calculated Design Limit DNBR (DL-DNBR), penalties are applied to the peaking factors of corner and side rods. It has been determined that no penalty is required for these rods when the inter-assembly gap does not exceed 10 mm.

Verification of the DNB safety criteria for Condition II transients shall be performed by comparing the calculated minimum DNBR values for side and corner channels during the transient with the corresponding Design Limit DNBR (DL-DNBR). The DNBR analysis for these channels shall be conducted using the 208-channel model provided in this report, applied to the most limiting Condition II transient.

The methodology is conservative by design: it does not account for the reduction in $F_{\Delta H}$ with increasing burnup, and it assumes a low concentration of boric-acid when evaluating the peaking factor increase for peripheral rods due to assembly bow. These assumptions ensure that the applied penalties remain bounding under the most limiting conditions.

6. Future work

The presented analysis describes the methodology used to evaluate the fuel assembly bow phenomenon using VIPRE-W code for simulating it. The application of corrective peaking factor penalties has proven sufficient to prevent violations of the Design Limit DNBR (DL-DNBR).

Although the current approach ensures conservative and safe results, the applied penalties may lead to a significant reduction in fuel assembly power. This is primarily due to conservative assumptions made during the evaluation of peaking factors as a function of the inter-assembly gap. These include the assumption of low boric acid concentration, representative of a fresh core, and the presence of gadolinium-bearing rods, which increase the heterogeneity of energy release within the fuel assembly. Both factors contribute to an amplified local power increase due to bowing.

Future work should focus on removing these conservative assumptions and adopting best-estimate values to achieve more realistic and less penalizing results. Additionally, the lack of detailed data on inter-assembly gap distributions necessitated the use of bounding values and a deterministic penalty application. Acquiring accurate gap measurements and their statistical distribution would enable the identification of best-estimate values and associated uncertainties. This would allow the integration of the inter-assembly gap as a variable in the statistical framework of the Revised Thermal Design Procedure, improving both accuracy and flexibility in core design evaluations.

References

[1] S. Ray, A.J. Friedland, E.H. Novendstern. Westinghouse Advanced Statistical DNB Methodology –The Revised Thermal Design Procedure, Proceedings of the Third International Topical Meeting on Nuclear Power Plant Thermal Hydraulics and Operations, 1988, pp. 261–265.

[2] Cuta, J. M.; Koontz, A. S.; Stewart, C. W.; Montgomery, S. D.; Nomura, K. K. VIPRE-01: A Thermal-Hydraulic Code for Reactor Cores, Electric Power Research Institute (EPRI), Technical Report, 1989, EPRI-NP-2511-CCM-A-Vol.3-Rev.3.

[3] Westinghouse Electric Company. VVER Core Design and Safety Analyses, Westinghouse Nuclear, Technical Data Sheet, [Online]. Available: https://westinghousenuclear.com/data-sheet-library/vver-core-design-and-safety-analyses/

[4] Werner, C.J., et al. MCNP® Version 6.2 User's Manual, Los Alamos National Laboratory Report, 2017, LA-UR-17-29981.

[5] Smith, L. D., Hallehn, A., Elmahdi, A., Sheng, D. -Y., and Tejne, H. Benchmark testing the ODEN CHF loop to Columbia University HTRF, Proceedings of the 14th International Topical Meeting on Nuclear Reactor Thermalhydraulics (NURETH-14), 2011, Paper NURETH14-368, Toronto, Canada.

LWR 2025 Proceedings, p. 65-77

Westinghouse Fuel Thermal -Hydraulic Testing Capabilities

Fredrik Waldemarsson[1]*, Carrie Wood[2]

[1]Westinghouse Electric Sweden
[2]Westinghouse Electric Company

*E-mail: *waldemf@westinghouse.com*

Abstract. Light Water Reactors (LWRs) rely on complex core thermal-hydraulic behavior to ensure safe and efficient operation. As advanced fuel designs are developed to support more demanding reactor operation, advanced modeling and rigorous testing are essential to optimize performance, address emerging challenges and meet regulatory requirements. This paper focuses on the testing aspect and the capabilities currently within Westinghouse to support these developments.

The Westinghouse fuel thermal hydraulic laboratory located in Västerås Sweden has been operated since the 1960's and currently houses five test facilities used for assessing Boiling Water Reactor (BWR), Pressurized Water Reactor (PWR) and Vodo-Vodyanoi Enyergeticheskiy Reactor (VVER) fuel thermal hydraulic performance. The ODEN and FRIGG loops are Westinghouse facilities used for primarily determining fuel critical heat flux for PWR/VVER and BWR fuel designs respectively. Both loops operate at nominal and off-nominal reactor conditions for their respective intended fuel design application. The EMBLA and FRODE loops are used for assessing, among other things, PWR/VVER and BWR fuel assembly and component pressure drop. Both loops operate at or close to reactor representative Reynolds values. The BURE loop is used for assessing long term fretting in BWR fuel. The loop is run at BWR reactor conditions using full BWR assemblies containing natural uranium.

Westinghouse has another PWR fuel and component test laboratory located in Columbia, South Carolina, part of the Columbia Fuel Fabrication Facility (CFFF). This lab was established in the late 1980's from loops and test components originally at the Westinghouse Electric Forest Hills facility in Pennsylvania. The lab contains mechanical test rigs for fuel component and fuel assembly testing as well as three thermal-hydraulic test loops. The Fuel Assembly Compatibility Test System (FACTS) loop, used to gather pressure drop data as well as vibration data for single, full-size fuel assemblies. The Vibration Investigation and Pressure Drop Experimental Research (VIPER) loop, used for thermalhydraulic testing in either a single or dual PWR or VVER fuel assembly configuration to demonstrate grid-to-rod fretting performance, hydraulic resistance as well as the vibration characteristics of the fuel assemblies and fuel rods based on flow at ~500,000 Reynolds number. The Vibration Investigation of Small-scale Test Assemblies (VISTA) loop, often used for small-scale hydraulic testing of fuel assemblies for proposed fuel design changes, prior to investing in FACTS or VIPER testing.

1. Introduction

Light Water Reactors (LWRs) rely on complex core thermal-hydraulic behavior to ensure safe and efficient operation. As advanced fuel designs are developed to support more demanding reactor operation, advanced modeling and rigorous testing are essential to optimize performance, address emerging challenges and meet regulatory requirements. This paper focuses on the testing aspect and the capabilities currently within Westinghouse to support these developments.

2.Westinghouse Sweden test loops

Westinghouse Sweden is the Westinghouse center of excellence for BWR and VVER fuel and houses five thermal hydraulic test loops, ODEN, FRIGG, BURE, FRODE and EMBLA. All are detailed and described in the sections below.

2.1 The ODEN loop

Heat transfer testing is an integral part of the design, testing and licensing of new PWR and VVER fuel products. The Columbia University’s Heat Transfer Research Facility (HTRF) used to be the primary location where nuclear fuel vendors performed Departure from Nucleate Boiling (DNB) testing. This facility was established in the 1950s and closed down in 2003. The numerous tests performed there on behalf of Westinghouse provided the licensing basis for the Westinghouse PWR fuel designs for over 30 years. Therefore, as HTRF closed, it was viewed as strategically important for Westinghouse to secure direct access to such a test facility in order to support its future PWR and VVER fuel development programs. In 2003 Westinghouse decided to construct a PWR/VVER Fuel Test Facility, named ODEN, at the existing fuel laboratory in Västerås. In this way the existing power supply, capabilities and infrastructure already in place at the Västerås FRIGG BWR test facility could be utilized. The ODEN loop utilizes directly electrically heated rods to simulate the fuel rods. In directly heated rods, the current generating power is flowing through the rod outer clad. As such, the radial power configuration is set by the individual rod resistances as all rods are connected to the same plus and minus pole. CHF is detected using up to 8 thermocouples per rod embedded in the rod below the outer clad.

The loop installation was completed in 2006 and qualification / benchmark testing versus HTRF data was completed in 2010. The qualification test and the benchmark results are reported in [1].

In addition to CHF testing, high resolution thermal mixing tests can also be performed at the ODEN loop [2]. ODEN has been in commercial operation since 2011.

2.1.1 Test loop design and instrumentation

All parameters in the ODEN loop which impact the safety-related data from testing are calibrated with traceability to Swedish national standards (RISE Technical Research Institute of Sweden, formerly SP). These include inlet and outlet temperature, flow, pressure, and power (voltage, current). For extra assurance, each of these primary measurement channels has a calibrated and redundant measurement channel.

The data acquisition system (DAS) consists of a system of multiple computers which handle the scan, monitor, display, and record functions for test section and loop measurements. The DAS can accommodate up to 288 heater rod TCs, 49 sub-channel TCs (for mixing tests), plus 128 other channels. The scanning rate is 25 Hz. Data is recorded in 25 Hz and 5 Hz modes (averages of 25 Hz data). Transient and steady state data can be remotely accessed online. CHF detection is accomplished by visual observation of the temperature vs. time behavior of the TCs contained in the heater rods. All transient TC traces are displayed on digital plots.

The main characteristics of the ODEN loop is presented in Table 1

Table 1. *The Main characteristics of the ODEN CHF loop.*

Parameter	**Value**
Maximum operating conditions	
- Power	12 MW
- Pressure	20 MPa
- Temperature	366°C
- Flow	22 kg/s
Radial configuration	Up to 6x6 square and 19 rod hex
Axial configuration	Full axial length
Heater rod type	Directly heated

A schematic of the ODEN loop layout is shown in Figure 1

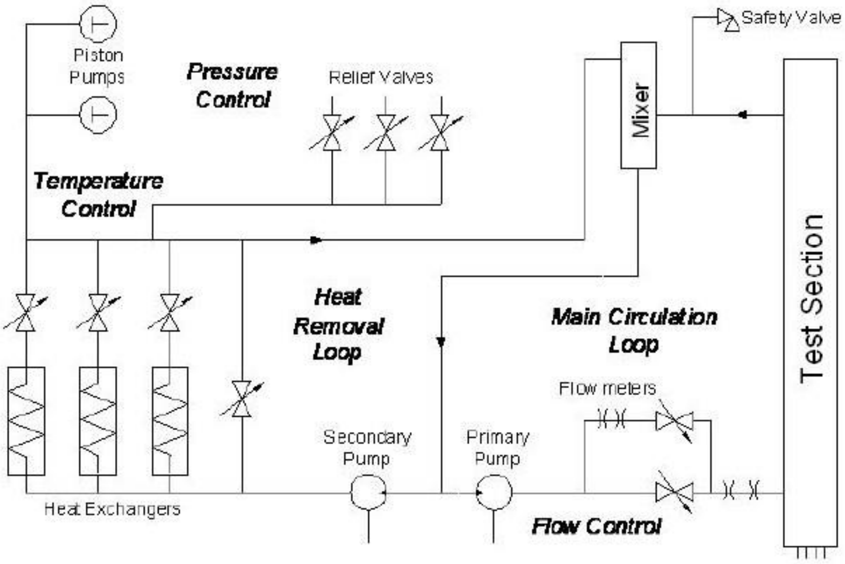

Figure 1. The ODEN loop layout.

2.2 The FRIGG loop

The Westinghouse FRIGG loop is a steam/water thermal-hydraulic test facility operating under prototypical BWR core conditions [3]. The facility has been operated since the 1960s to qualify a long series of BWR fuel designs, starting from the early 8x8 fuel lattice until the latest TRITON11 11x11 fuel design. The loop was modernized and upgraded in 1995 [4]. The control and instrumentation systems were further upgraded in 2015 in preparation to the TRITON11 test campaigns.

The FRIGG test loop is designed to cover all requirements for BWR fuel pressure drop, thermalhydraulic stability and heat transfer testing, including critical boiling transition (dryout), under a wide range of steady-state BWR operating conditions (flow, pressure, inlet temperature, power distributions). Variation in radial power distributions is achieved with the use of indirectly heated fuel rod simulators where the current heating the rods flow through filaments inside the rod, isolated from the outer clad, which allows assessment of each individual rod dryout performance, including partlength rods, under nominal and controlled (i.e. control blade insertion) operations. CHF is detected using up to 8 thermocouples per rod embedded in the rod below the outer clad. In addition to steadystate tests, realistic transient dryout experiments are also performed with rapid power and/or flow variations.

2.2.1. Test loop design and instrumentation

The FRIGG loop is designed to operate at maximum of 10 MPa and 15 MW, sufficient for full-length, full-lattice BWR fuel testing. The Westinghouse SVEA quarter-assembly can also be tested. Data collection of all relevant parameters is typically performed at 25 Hz. The test section consists of a pressure vessel, a flow channel and a fuel bundle made of indirectly electrically heated fuel rod simulators and spacer grids. Pressure sensors are connected to the flow channel at different elevation taps. A schematic of the FRIGG test loop can be found in Figure 2.

A realistic flow channel, which accurately represents the actual flow channel geometry (apart from the pressure taps), is used for testing. The same applies to the spacer grids, which are entirely without reinforcements. Use of standard components is possible in FRIGG due to the use of the indirect heater rods that eliminate the need for electrically insulating flow channel ceramics. More detailed information regarding the FRIGG loop design can be found in [3].

Rapid control of power and flow is possible to simulate typical limiting safety related BWR transients, such as mass flow rate reduction during a pump trip, rapid power increase during a pressure transient or a combination of both. The transient forcing functions are introduced from precalculations via a control computer.

The FRIGG data acquisition system consists of a main computer and a number of scanners, allowing the simultaneous collection of up to 1040 signals at 25 Hz. The data recording and control systems have been continuously upgraded to meet current standards.

Table 2. *The Main characteristics of the ODEN CHF loop.*

Parameter	Value
Maximum operating conditions	
- Power	15 MW
- Pressure	10 MPa
- Temperature	311°C
- Flow	25 kg/s
Radial configuration	Up to 11x11
Axial configuration	Full axial length
Heater rod type	Indirectly heated

The FRIGG loop layout is shown in Figure 2.

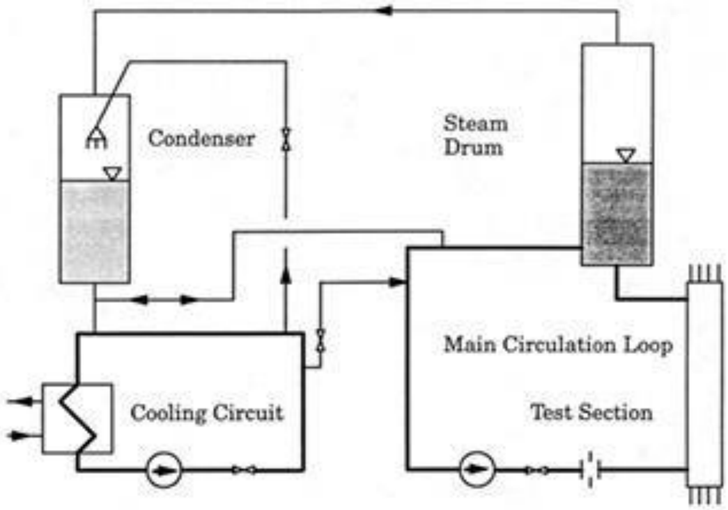

Figure 2. The FRIGG loop layout.

2.3 The BURE loop

The main objective of the BURE loop is to assess the mechanical behavior of the fuel design during operation. The BURE loop is typically run for approximatively 700 hours at typical BWR reactor conditions and at high flow, with a fully realistic fuel assembly containing natural uranium. Upon completion of the test, the fuel bundle is disassembled and thoroughly inspected for any marks related to vibration or fretting. The loop can be run both in single-phase and two-phase conditions. Two-phase condition is achieved using steam injection at the fuel inlet.

Table 3. *The Main characteristics of the BURE vibration and fretting loop.*

Parameter	**Value**
Maximum operating conditions	
- Pressure	8.5 MPa
- Temperature	300°C
- Flow	25 kg/s (including steam injection)
Radial	Full radial scale
Axial configuration	Full axial length

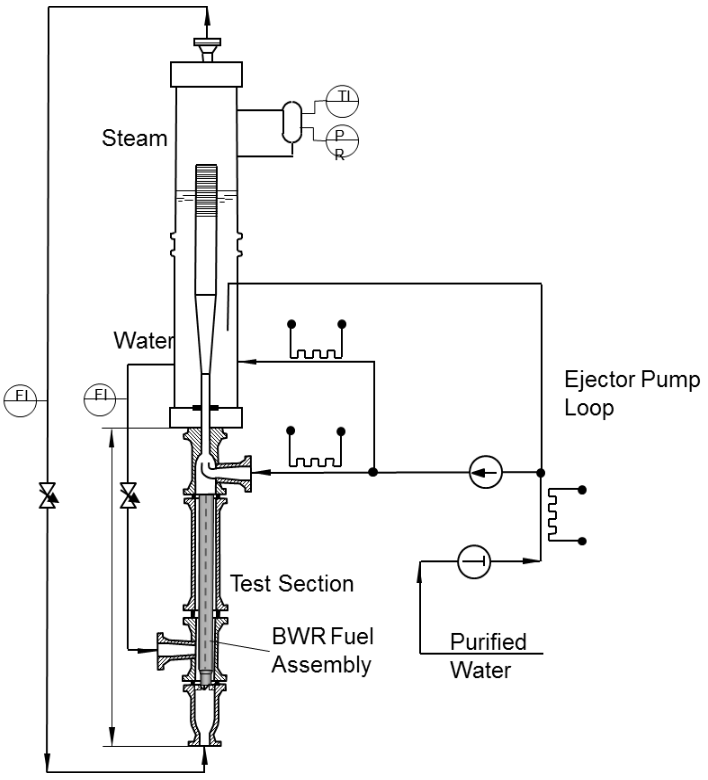

Figure 3. The BURE loop layout

2.4 The FRODE loop

The FRODE loop is a semi full-scale water thermal-hydraulic test facility. The main capabilities of the loop include the measurement of BWR axial pressure drop over various fuel components and the measurement of internal and external water bypass flow. The loop is also designed for debris filter testing and, more recently, includes hydraulic lift force measurement capabilities [5]. The test bundles typically have a realistic full-scale inlet and outlet and a shortened fuel rod section.

In the FRIGG loop, the heated length of the BWR fuel assembly is simulated in detail. However, due to the design of the fuel simulators and their need to protrude in and out of the test vessel, prototypical fuel inlet and outlet components outside the heated length cannot be considered. These are instead tested in the FRODE loop.

2.4.1. Test loop design and instrumentation

A schematic of the FRODE loop can be found in Figure 4. The loop runs at atmospheric pressure under adiabatic single-phase conditions, with temperatures up to 80°C and Reynolds number up to $8 \cdot 10^4$ (for full BWR assembly lattices). The temperature is measured with a thermocouple (T) upstream of the circulating pump (P1). The measurement uncertainty of the temperature is ±1°C.

Loop flow is measured with an orifice plate (q1) upstream the test section and a Coriolis flowmeter

(q2) downstream the test section. The total uncertainty of the flow readings is typically below 0.3 %.

Both the flow measurement using the orifice plate and pressure drop are recorded by several pressure drop transducers, with different ranges, in parallel. The data acquisition system then chooses the transducer with the optimal range for the measurement in question and stores those values in a virtual channel. This is done to have the lowest measurement uncertainty possible during the recordings. The total uncertainty of the pressure drop readings is typically below 0.5%. The data acquisition system records data with 10 Hz sampling frequency.

Table 4. *The Main characteristics of the FRODE loop.*

Parameter	Value
Maximum operating conditions	
- Pressure	0.1 MPa
- Temperature	85°C
- Flow	30 kg/s
Radial	Full radial scale
Axial configuration	Reduced axial scale

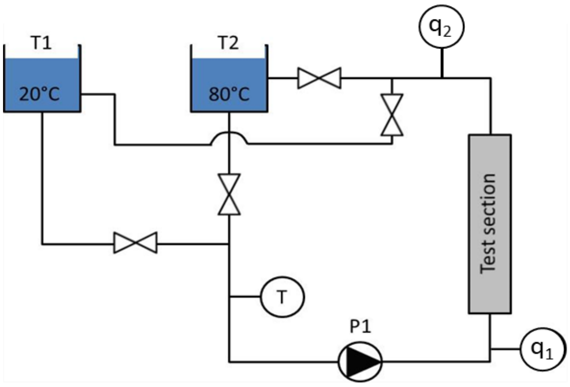

Figure 4. The FRODE loop layout.

2.5 The EMBLA loop

The EMBLA single-phase pressure drop loop was completed in the autumn of 2022. EMBLA was built with the main purpose of assessing the detailed single-phase axial pressure drop characteristics of inlet/outlet fuel components, individual spacers and bare rod friction for VVER, PWR and BWR fuel designs. Full scale realistic assemblies can be tested.

2.5.1. Test loop design and instrumentation

The EMBLA loop was designed and built to perform pressure drop tests on VVER, PWR and BWR fuel components. The loop has a design pressure of 18 bar with the main function to prevent the fluid from boiling (with margin) at high temperature. The design temperature is 160°C and is measured using a Pentronic 4-wire PT100 resistance temperature detector (RTD). The loop is heated using the excess heat generated from the pump. Stable temperature is maintained using a heat exchanger. Since the pressure and temperature is lower than for typical reactor conditions, a reactor representative Reynolds number is instead achieved by performing measurements at significantly higher flows than in the reactor. The maximum design flow of the loop is 150 kg/s. The primary flow is measured using a Emerson micro motion elite Coriolis flow meter using a micro motion 5700 field-mount transmitter.

A typical test procedure involve full flow sweeps (low to high flow) at 50°C, 100°C and 150°C where the low temperature data is mainly used for maintenance and loop consistency checks while the high temperature data is generally used for loss coefficient evaluation. After the high temperature data is taken, the loop is cooled down to 50°C and heated up again and all measurements are repeated as an additional quality check.

Up to 20 pressure differential transducers can be installed (calibrated to the expected range of measurements) to accurately characterize the pressure drop of the fuel components. To further enhance pressure drop measurement accuracy and reliability, all components are measured using flexible overlapping pressure drop spans and can thus be compared to each other enabling the operator to quickly identify potential issues with the pressure transducers.

Both full length fuel and part length fuel assemblies can be accommodated in the facility. EMBLA has been validated in [6], and [7].

2.5.1.1. Special focus on accurate flow measurement

The single most important measured parameter related to the pressure loss coefficient uncertainty is the mass flow rate. Therefore, when designing EMBLA, extra emphasis was given to produce accurate flow measurement.

Table 5. *The Main characteristics of the EMBLA pressure drop loop.*

Parameter	Value
Maximum operating conditions	
- Pressure	1.8 MPa
- Temperature	150°C
- Flow	150 kg/s
Radial	Full radial scale
Axial configuration	Full axial length

The EMBLA loop was designed with a very long straight inlet prior to the test section, ensuring fully developed inlet flow which improves data quality on measurements performed in the lower region of the fuel bundle. This can be observed in Figure 5. To further enhance the quality of the flow measurements, dual flow meters were installed. The primary flow measurement is performed using a Emerson micro motion elite Coriolis flow meter using a micro motion 5700 field-mount transmitter with very low uncertainty ($1\sigma \approx 0.1\%$) over the entire operating range while the redundant flow measurement utilizes a Emerson compact flow meter conditioning orifice plate ($1\sigma \approx 0.6\%$). In addition to the very low uncertainty of the primary flow meter, having redundant measurements gives an additional level of confidence in the measurements since any fault with either measurement would be instantly noticeable.

Figure 5. The EMBLA loop layout. Top left: Coriolis flow meter. Bottom left: Pump. Right: Overview.

3.Westinghouse US Test Loop

Westinghouse US is the Westinghouse center of excellence for PWR fuel and houses three thermal hydraulic test loops, FACTS, VIPER and VISTA. All described in the sections below.

3.1 The FACTS loop

The Fuel Assembly Compatibility Test System (FACTS) Loop was installed in Columbia in 1988 as an isothermal, single fuel assembly deionized water loop used to gather thermal hydraulic data and vibration data for fuel assemblies [8]. It consists of a test vessel, pressure housing, piping, venturi flow meter, variable frequency drive (VFD) pump, pressure regulators, valves, RTDs, differential pressure transducers and a heat exchanger. The water is heated via the pump work and the fluid temperature maintained using cooling water through a heat exchanger. The design operating limits of the system are 121°C and 1.6 MPa.

Pressure drop measurements are collected at various flowrates and loss coefficients are calculated. In addition to pressure drop data, custom built accelerometer rods measure typical rod vibration and inductive displacement transducers mounted in the test vessel walls measure overall assembly vibration. The loop uses a LabVIEW system for pressure drop data acquisition and a Brüel & Kjær Connect system for vibration data acquisition.

Table 6. *The Main characteristics of the FACTS loop.*

Parameter	**Value**
Maximum operating conditions	
- Pressure	1.6 MPa
- Temperature	121°C
- Flow	150 kg/s
Radial	Full radial scale
Axial configuration	Full axial length

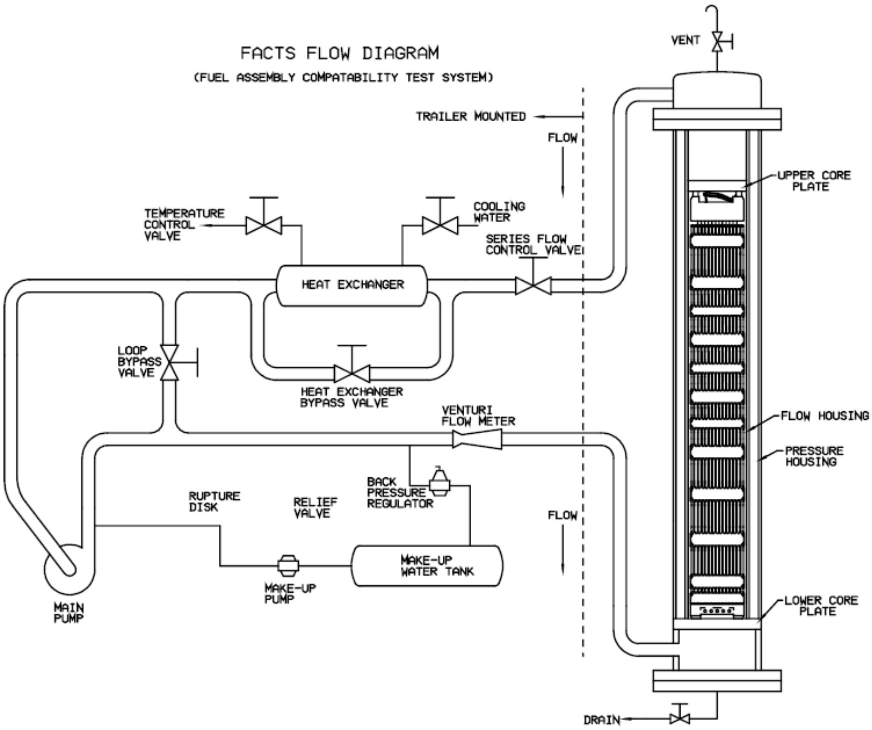

Figure 6. The FACTS loop layout

3.2 The VIPER loop

The Vibration Investigation and Pressure Drop Experimental Research (VIPER) Loop was implemented in 1999 for thermal hydraulic testing in either a single or dual fuel assembly configuration to demonstrate grid-to-rod fretting performance and measure the hydraulic resistance as well as the vibration characteristics of the fuel assemblies and fuel rods based on flow at ~500,000 Reynolds number [9].

This deionized water loop is comprised of a test vessel, piping, two variable frequency drive process pumps, an immersion heater, expansion tank, air separator tank, heat exchanger, venturi flow meter, automated and manual valves, differential pressure transducers, and RTDs. The loop can accommodate conditions of up to 203°C, 2.5 MPa, and up to 400 kg/s axial flow and 16.5 kg/s cross flow. The loop uses a PLC for control, a LabVIEW system for pressure drop data acquisition, and a Brüel & Kjær Connect system for vibration data acquisition.

***Table** 7. The Main characteristics of the VIPER loop.*

Parameter	Value
Maximum operating conditions	
- Pressure	2.5 MPa
- Temperature	203°C
- Axial flow	400 kg/s
- Cross-flow	16.5 kg/s
Radial	Full radial scale
Axial configuration	Full axial length

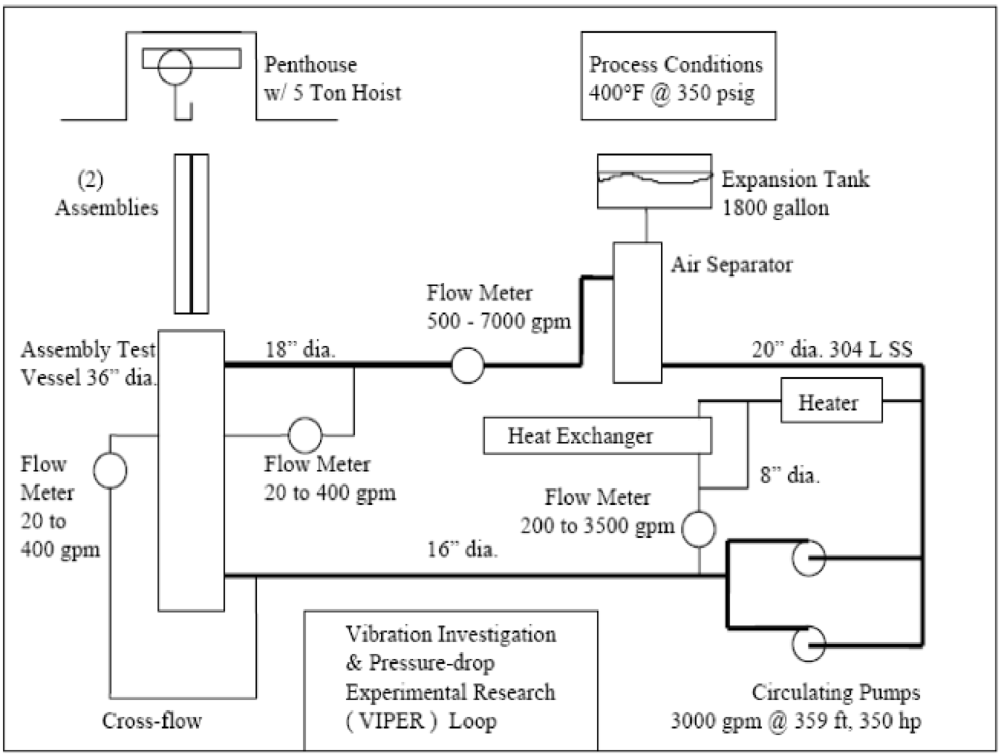

Figure 7. The VIPER loop layout.

3.3 The VISTA loop

The Vibration Investigation of Small-Scale Test Assemblies (VISTA) Loop was installed in 1999 for small-scale hydraulic testing of fuel assemblies. With the use of small-scale fuel bundles, normally of 5x5 cell grid sections and empty, sealed Zircaloy cladding rods, Westinghouse can test the hydraulic characteristics (specifically pressure drop and HFV of grid straps due to flow) of proposed changes to grid designs [9]. Since it uses a small-scale bundle and operates at low temperatures and pressures, it is often used to inexpensively acquire scoping data for proposed fuel design changes, prior to investing in FACTS or VIPER testing.

Table 8. *The Main characteristics of the VISTA loop.*

Parameter	Value
Maximum operating conditions	
- Pressure	0.6 MPa
- Temperature	27°C
- Flow	25 kg/s
Radial	Up to 5x5
Axial configuration	Reduced axial length

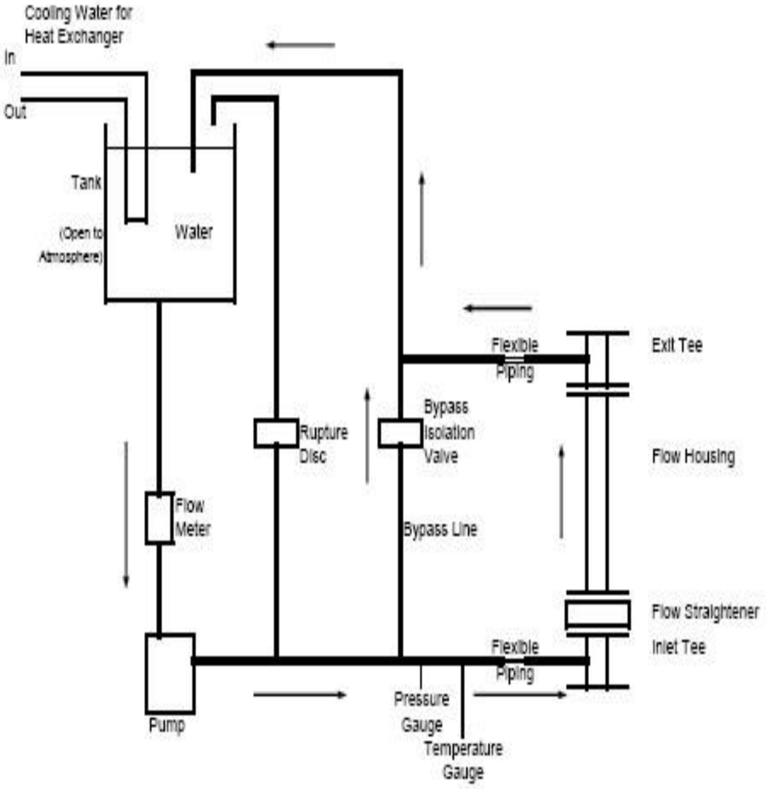

Figure 8. The VISTA loop layout.

4. Summary

Westinghouse thermal-hydraulic testing capabilities have been presented. Utilizing the different facilities presented in this paper, Westinghouse has the capability to completely thermal-hydraulically characterize all Westinghouse fuel in-house. The Westinghouse facilities are open to external testing.

References

[1] L.D. Smith, A. Halléhn, A. Mandour, D.-Y. Sheng, and H. Tejne, "Benchmarking Testing of the ODEN CHF Loop to Columbia University HTRF", 14th International Topical Meeting on Nuclear Reactor Thermal Hydraulics (NURETH-14) Toronto, Canada, 2011

[2] L.D. Smith, P. Joffre, J-M. Le Corre, F. Waldemarsson, H. Tejne, A. Halléhn,"High Resolution Thermal Mixing at Westinghouse ODEN Loop", 14th International Topical Meeting on Nuclear Reactor Thermal Hydraulics (NURETH-14) Toronto, Canada, 2011

[3] S. Andersson, L. D. Smith, A. Halléhn and D.-Y. Sheng, "Westinghouse fuel heat transfer test facilities", Nuclear Reactor Fuel Performance Conference (TopFuel 2011), Chengdu, China (2011).

[4] O. Nylund, "Upgrade of the FRIGG test loop for BWR fuel assemblies", ABB Review, **6**, ABB Atom AB (1997).

[5] F. Waldemarsson, J-M. Le Corre, S.-Ö. Lindahl, U. C. Bergmann, Y. Le Moigne, "BWR bundle lift force measurements, modelling and validation," 18th International Topical Meeting on Nuclear Reactor Thermal Hydraulics (NURETH-18), Portland, USA (2019).

[6] F. Waldemarsson, M. Andersson and R. Enlund "An overview of the EMBLA single-phase pressure drop loop", Specialist Workshop on Advanced Instrumentation and Measurement Techniques for Nuclear Reactor Thermal Hydraulics and Severe Accidents (SWINTH-2024), Dresden, Germany (2024).

[7] F. Waldemarsson, M. Dostál and L. Kroj " Pressure drop measurement comparison between the Westinghouse EMBLA loop and the ŠKODA JS KAZEX loop", Nuclear Reactor Fuel Performance Conference (TopFuel 2025), Nashville, USA (2025).

[8] R. Y. Lu, K. D. Broach, and J. J. McEvoy, "Fuel Assembly Self-Excited Vibration and Test Methodology," Proceedings from ICAPP-04, (2004)

[9] R. Y. Lu, M. E. Conner, M. L. Boone, C. L. Wilbur, and R. Marshall "Nuclear Fuel Assembly FlowInduced Vibration and Endurance Testing," Proceedings from Symposium on Flow-Induced Vibration at ASME Pressure Vessles and Piping Conference, (2001)

Analysis of Main Steam Line Break at Hot Zero Power Using ATHLET, COCOSYS and DYN3D

Nadejda Rijova*, Alexander Yordanov

[1]ENPRO Consult, Sofia

*E-mail: *nrijova@enproco.com*

Abstract. Main Steam Line Break at Hot Zero Power (MSLB at HZP) is a design basis accident for VVER-1000 reactors. This accident scenario involves a significant cooling of the affected loop and the corresponding section of the reactor core. As a result, return to power occurs in the core due to negative moderator temperature feedback. The steam released into the containment increases the pressure in it, leading to the initiation of safety signals that influence the behaviour of both the primary and the secondary circuit equipment. Consequently, the event encompasses complex thermal-hydraulic and 3D neutron kinetics phenomena that must be addressed in the analysis.

Three distinct approaches were employed in this investigation to analyse MSLB at HZP:

1. Fully coupled ATHLET-COCOSYS-DYN3D calculation: This approach integrates all three codes to provide a comprehensive simulation of the event.

2. Hybrid ATHLET-COCOSYS + DYN3D approach: This approach begins with an ATHLET-COCOSYS calculation with a point kinetics model accounting for the average coolant temperature in each of the four reactor sectors. Subsequently, the results for reactor pressure, reactor flow rate and temperatures at the reactor inlet for each of the four sectors are utilized as boundary conditions in a DYN3D calculation. This allows to determine the power of each fuel assembly, considering its position in the core, as well as its enrichment and burnup. In addition, a hot FR is modelled.

3. ATHLET-COCOSYS coupled calculation. This is the first part of the previous approach. To cover the uncertainties of the point kinetics model, hot FA and hot FR are modelled.

1. Short description of the codes and coupled code systems used in the investigation

1.1 ATHLET

The ATHLET code is being developed by the German Society for Safety of installations and Reactors (Gesellschaft für Anlagen- und Reaktorsicherheit, GRS) [1]. It is an advanced best-estimate code developed for the simulation of design basis and beyond design basis accidents (without core degradation) in light water reactors.

The one-dimensional, two-phase fluid dynamics models are based on a five-equation model supplemented by a full-range drift-flux model, including a dynamic mixture-level tracking capability. Moreover, a two-fluid model based on six conservation equations is provided. The heat conduction and heat transfer module allow a flexible simulation of fuel rods and structures. The nuclear heat generation is calculated by a point-kinetics or by a one-dimensional kinetics model. A general control simulation module is provided for a flexible modelling of the controllers and auxiliary plant systems.

The ATHLET code has been used in ENPRO since 2003. The input deck for KNPP 5 and 6 is verified and validated against operational events and via code-to-code comparison. The code was recently applied in the framework of RWFA licensing project for analysis of:

- Dynamic stability
- Anticipated operational occurrences (category 2)
- Anticipated transients without scram
- Accidents with fuel malting for evaluation of the SAMG

1.2 COCOSYS

The COCOSYS code is being developed by the German Society for Safety of installations and Reactors (Gesellschaft für Anlagen- und Reaktorsicherheit, GRS) for the simulation of all processes and conditions in the containments of PWR in the course of both design and beyond design basis accidents, including severe accidents [2]. In addition, the code is intended for the calculation of the mass and energy release of radioactive products into the environment (source term).

The COCOSYS code has been used in ENPRO since 2003. The code was recently applied in the framework of RWFA licensing project for:

- Containment analysis during LBLOCA
- Containment analysis during MSLB

1.3 ATHLET-COCOSYS

The coupled ATHLET-COCOSYS code system is being applied in ENPRO since 2010 for:

- LBLOCA for Kozloduy NPP
- MSLB for Belene NPP.

1.4 DYN3D

DYN3D is being developed in the Helmholtz-Zentrum Dresden-Rossendorf, Germany. It is a three-dimensional kinetics computer code developed for the investigation of reactivity initiated accidents in the core of thermal reactors with hexagonal and square fuel assemblies. It comprises a 3D-neutron kinetics model and a thermal-hydraulic calculation module, the connection of which is given by a parameterized dependence of the neutron group constants on the fuel temperature, moderator temperature, moderator density and boron acid concentration.

The DYN3D code has been used in ENPRO since 2002. The code was recently applied in the framework of RWFA licensing project for:

- reactivity initiated accidents
- including generation of library with diffusion and kinetics parameters in NEMTAB format using the Westinghouse code PHOENIX5

1.5 ATHLET-DYN3D

The coupling ATHLET-DYN3D is a common development of the GRS and HZDR. The validation of the system is performed in HZDR both for VVER-440 and VVER-1000 by means of operational events and code-to-code comparison [3].

The coupled ATHLET-DYN3D code system has been applied in ENPRO since 2023.

2. Analysis of MSLB

Traditionally, MSLB was analysed in ENPRO with a system thermal-hydraulic code ATHLET or RELAP with a point kinetics model. The point kinetics has proven reliable; it is widely used in the safety analyses. Nevertheless, it has certain deficiencies when it comes to analyses of reactivity-initiated accidents with unsymmetrical behavior of the reactor installation. MSLB causes significant cooling in one sector of the core related to the affected steam generator, which leads to biggest negative reactivity insertion in that sector. The traditional point kinetics method calculates the reactivity feedbacks based on coolant and fuel temperature averaged by the core. As a compromise, the ATHLET code allows for representing different sectors in the core, which are treated in the point kinetics model as different cores. This way, the power of each sector is calculated based on the coolant and fuel temperatures in it. Another conservative approach is applied in RELAP, allowing to define which coolant temperature should be used by the code for the calculation of the moderator temperature reactivity feedback.

Another deficiency of the point kinetics in view of the MSLB analysis at HZP is that the reactivity coefficients can be defined constant either for HZP or for HFP, while the event starts at 0 power and leads to return to power.

The next source of uncertainty in the MSLB analysis using the point kinetics method is the fact that it does not account for the enrichment and burning of the FAs or for the insertion of the control rods.

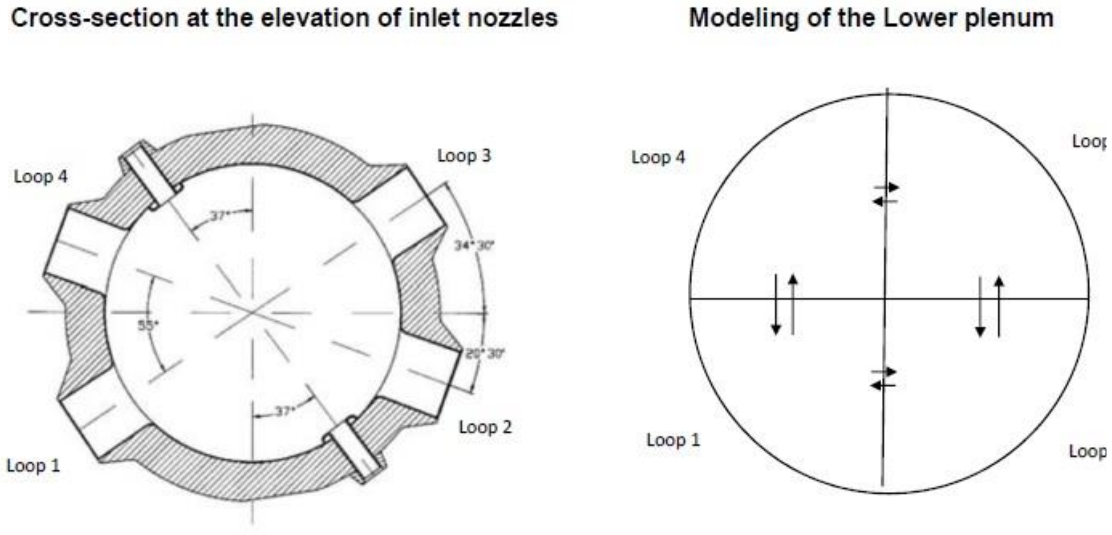
Cross-section at the elevation of inlet nozzles

Modeling of the Lower plenum

Figure 1. Coolant mixing in the lower plenum

All these deficiencies of the point kinetics justify the application of ATHLET-DYN3D coupling. In addition to this pair of codes, it was decided to use COCOSYS for the correct determination of the moment when the containment pressure reaches the set-point for the scram signal generation.

The analysis of events leading to unsymmetrical behavior of the reactor installation requires a correct modeling of the coolant mixing in the core. In the one-dimensional thermal-hydraulic codes, such as ATHLET, the mixing between the different parts of the lower plenum is modelled by means of cross-connections (Figure 1). The cross-connections are validated against KNPP 6 operational event 747 “Trip of MCP 3”.

2.1 Description of the applied approaches

In order to compare the traditional conservative approach for an evaluation of MSLB at HZP with the complex ATHLET-COCOSYS-DYN3D analysis, three different calculations have been performed:

1. ATHLET-COCOSYS-DYN3D coupling

- The TH parameters in the primary and secondary circuit calculated by ATHLET
- The core is represented by 163 core channels (Figure 2)
- The insertion of control rods is determined by ATHLET
- The containment parameters are calculated by COCOSYS
- The power of each FA calculated by DYN3D taking into account the enrichment, burnup and insertion of the control rods

A schematic representation of the parameters exchanged between the codes is given in Figure 3.

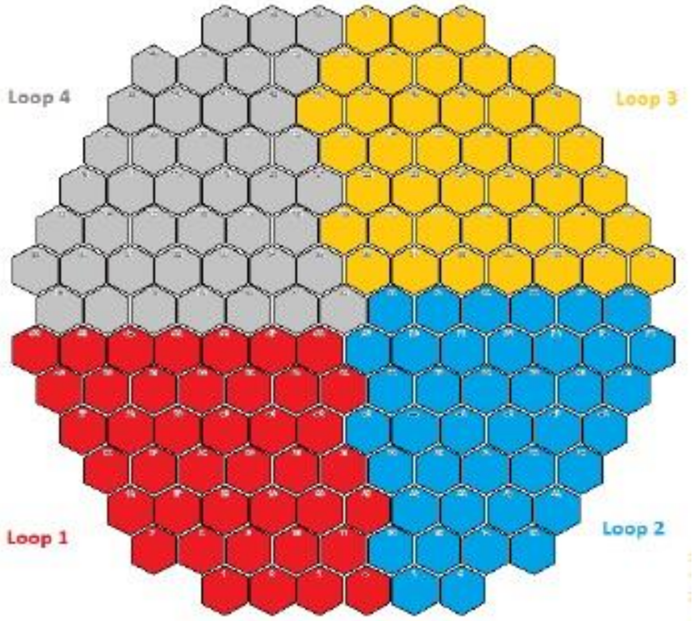

Figure 2. ATHLET nodalisation of the core (cross-section)

2. ATHLET-COCOSYS coupling + DYN3D

The analysis starts with an ATHLET-COCOSYS calculation. The following parameters are used as boundary conditions for a DYN3D calculation:

- pressure in the primary circuit
- coolant flowrate in the four sectors
- temperatures at the inlet of the four core sectors

A DYN3D calculation is performed with a hot FR modelled in the FA found to be “hottest” in the ATHLET-COCOSYS-DYN3D coupled calculation, with rod relative power = 1.57 equivalent to the maximum hot rod peaking factor Kr determined in the core design

3. ATHLET-COCOSYS coupling

The reactivity is determined separately for each part of the core, thereby accounting for the different coolant and fuel temperatures in the sectors. A hot FA is modelled with assembly relative power kq=1.34 as obtained from the ATHLET-COCOSYS-DYN3D coupled calculation. A hot FR is modelled in the hot FA with relative power Kr = 1.57 equivalent to the maximal hot rod peaking factor Kr determined in the core design.

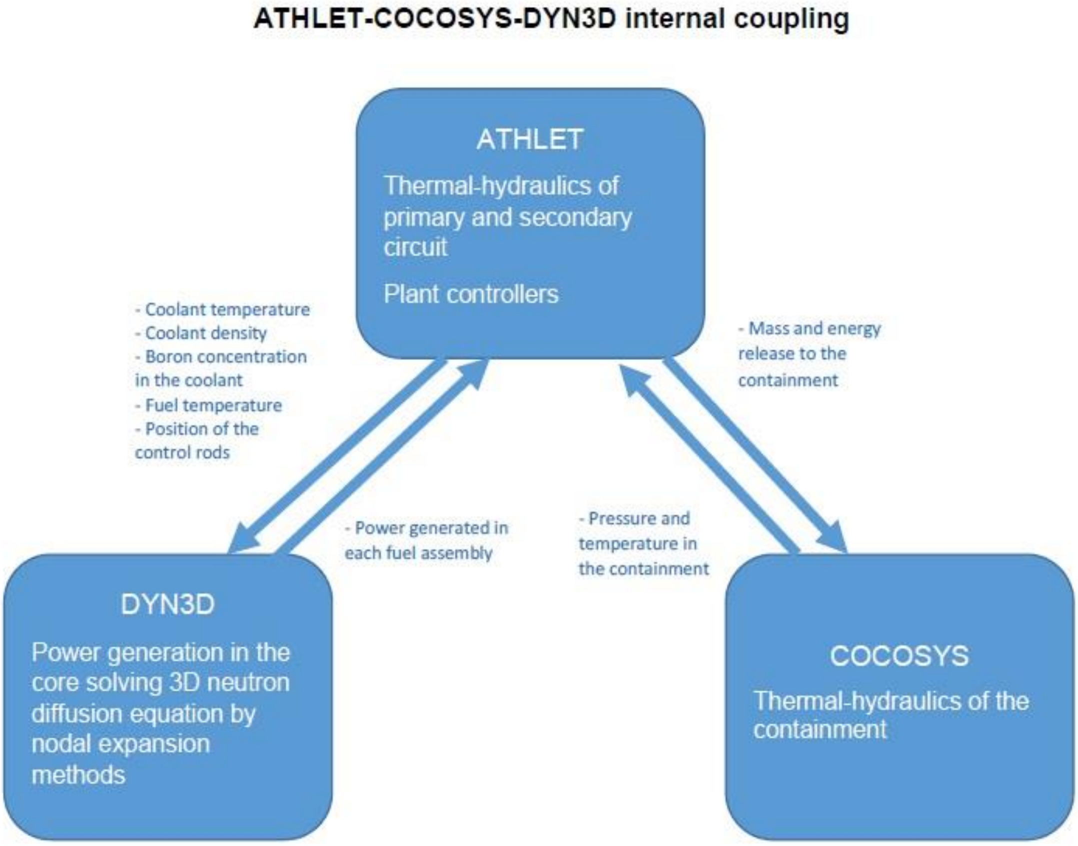

Figure 3. Parameters exchange between the codes

2.2. Comparison of the results

The results of the three approaches are described below with emphasis on the ATHLET-COCOSYS-DYN3D coupling.

Figure 4 shows the power distribution in the core at the beginning of the event and at the time of the peak power in the core. Figure 5 depicts the power distribution by sectors in time.

Figures 6, 7 and 8 present the results obtained by the three approaches. The peak value of the power calculated by the first and second approaches is similar, while the power calculated by the point kinetics is approximately 20% lower. This is due to the inability of the point kinetics model to allow for the fact that the moderator temperature reactivity coefficient becomes stronger with return to power. The conservative approach to model a hot assembly and a hot rod in it compensates for this deficiency when the acceptance criteria for the peak cladding fuel temperatures are checked.

In Figures 7 and 8, the maximal cladding and fuel temperatures for the hot rod in calculations 2 and 3 are shown with dashed lines.

The DYN3D analyses performed with boundary conditions from ATHLET allows for a correct calculation of the peak value of the reactor power.

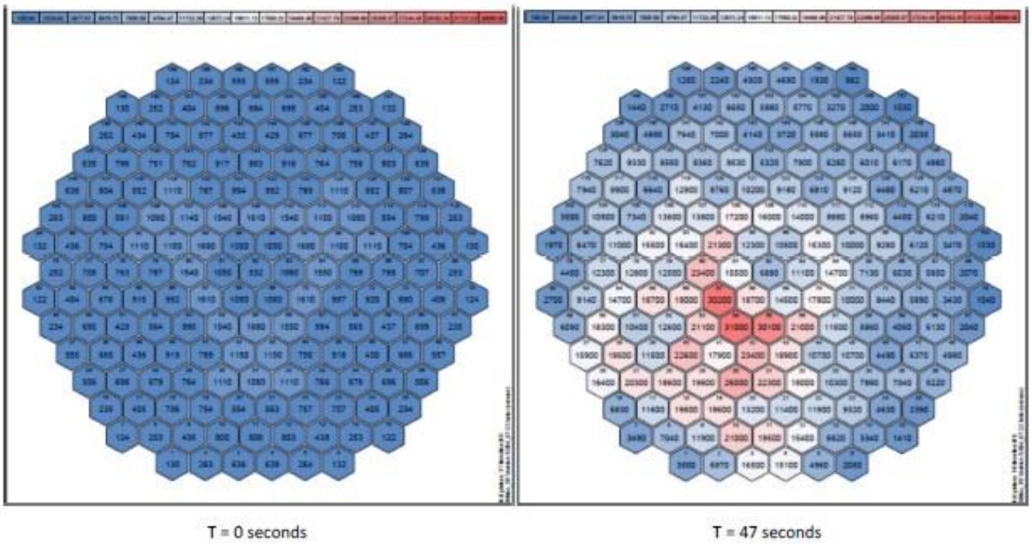

Figure 4. Power distribution in the core as determined by ATHLET-COCOSYS-DYN3D

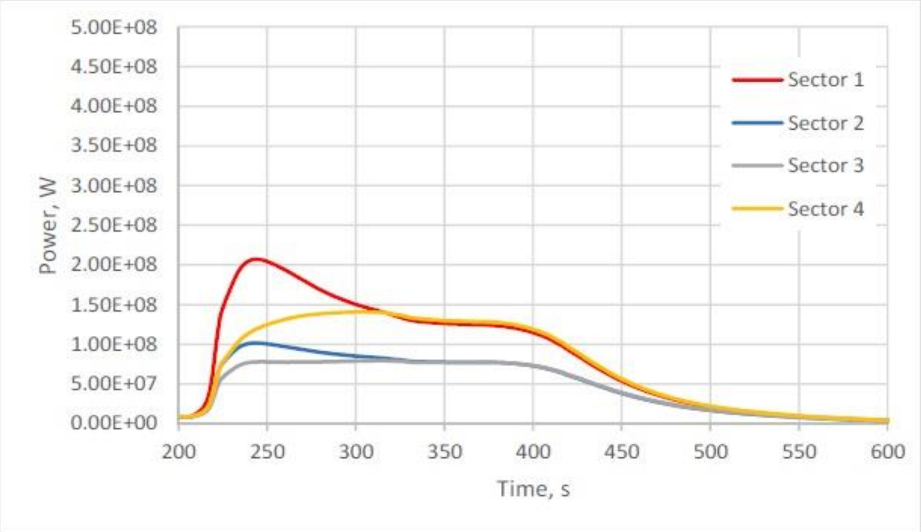

Figure 5. Power distribution in the core by sectors in time, determined by ATHLET-COCOSYS-DYN3D

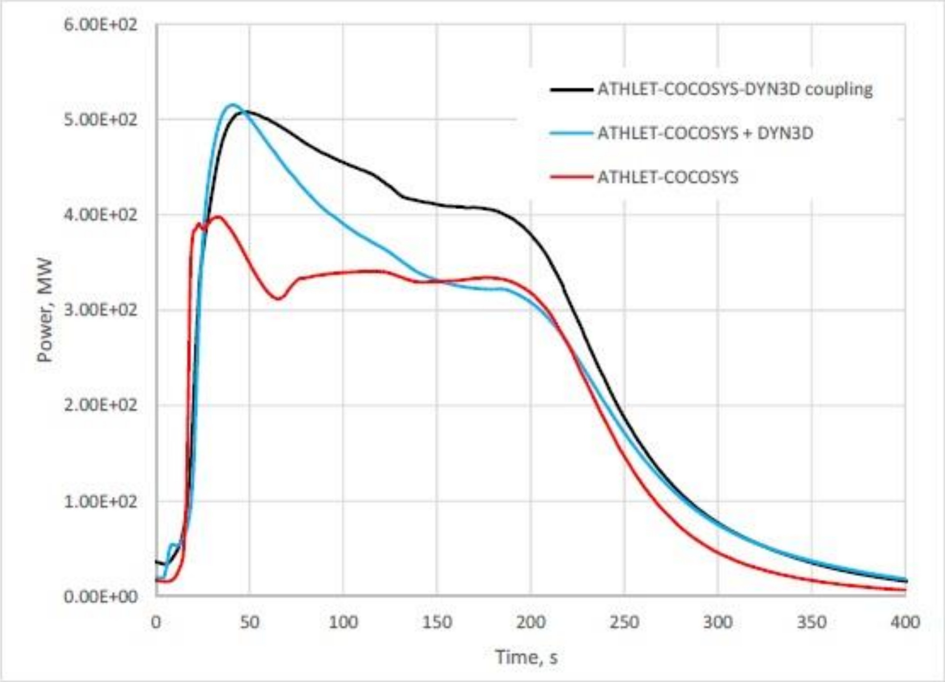

Figure 6. Core power calculated by the three approaches

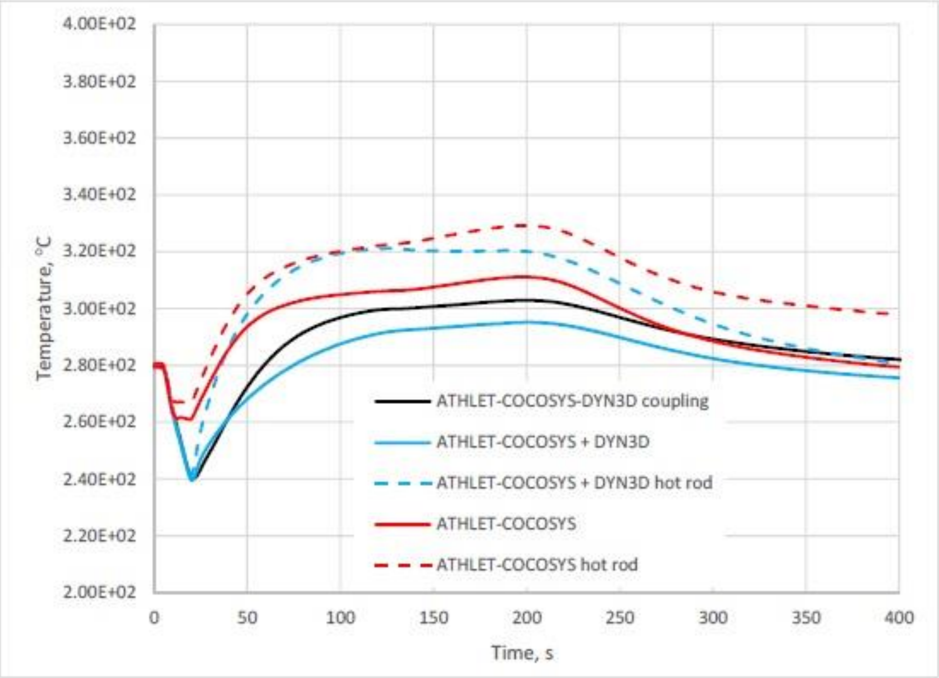

Figure 7. Maximum cladding temperature calculated by the three approaches

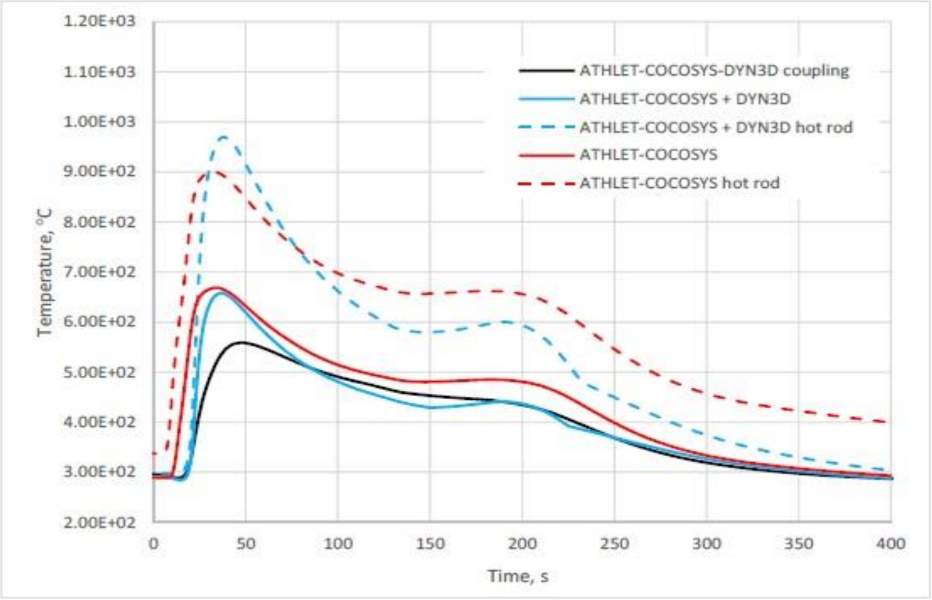

Figure 8. Maximum fuel temperature in the centre of the rod calculated by the three

Table 1. *Scenario of the event*

Event	Time, s		
	A-C-D	A-C+D	A-C
Double-ended break of the main steam line of SG1 inside the containment	0	0	0
Signal for tripping of RCP1 due to low pressure in the steam line and low ΔP over the check valve. The pump remains in operation Closing of the check valve on steam line 1	0.2	0.2	0.2
Signal for low pressure in MSL 1, high ΔTs I-II and coolant temperature in any of the hot legs above 200 °C - Actuation of ASSS - FAIV-1 starts to close	0.2	0.2	0.2
Signal for isolation of the feedwater line. Only the safety-graded valves start to close.	2.5	1.9	1.9
Signal for containment isolation	4.3	4.4	4.4
Tripping of all RCPs due to containment isolation	19.3	19.4	19.4
Maximum reactor thermal power reached	47	40	33

Table 2. *Comparison of the peak temperatures*

	Parameter	A-C-D	A-C+D	A-C
1	Peak cladding temperature, C	303	320	329
2	Peak fuel centre line temperature	559	961	899

Table 1 represents the scenario of the event.
Table 2 provides a comparison of the peek temperatures calculated by the three approaches.

3. Conclusions

1. ATHLET-COCOSYS-DYN3D coupling is a best estimate approach allowing for a realistic modelling of RIA with asymmetrical behaviour of the reactor installation.

2. The system thermal-hydraulic code with point kinetics may underestimate the power due to using constant reactivity feedbacks for the whole range of power from HZP to return to power. Applying system code and 3D kinetics code afterwards leads to correct determination of the peak power.

3. A conservative modelling approach in point kinetics is capable of compensating for the deficiencies of the method.

References

[1] H. Austregesilo and others, ATHLET 3.3.1 User's Manual, GRS-P-1 / Vol. 1 Rev. 10, 2022
[2] S. Arndt and others, COCOSYS 3.3.1 User Manual, GRS-P-3 / Vol.1, 2022
[3] Y.Kozmenkov, S.Kliem, U.Rohde, Validation and verification of the coupled neutron kinetic/thermal hydraulic system code DYN3D/ATHLET

Acknowledgements

To **Dr. Yuri Bilodid** from the Helmholtz-Zentrum Dresden-Rossendorf (HZDR) for the consultations.

To **Maksym Ieremenko** from State Scientific and Technical Center for Nuclear and Radiation Safety-Kiev (SSTC NRS) for the Max_Core software for visualization of the core parameters in the form of core maps.

LWR 2025 Proceedings, p. 87-92

Fuel Safety Analysis Capability Development in SÚRO

Katalin Kulacsy[1*]

[1]National Radiation Protection Institute, Bartoskova 1450/28, 140 00 Prague, Czech Republic

[*]E-mail: *katalin.kulacsy@suro.cz*

Abstract. The Czech Republic is undergoing a very intense period of nuclear development. Within a few years four new fuel types have been or will be licensed, two large new commercial units have been contracted and siting and preparations have started for several small modular reactors.

The Czech National Radiation Protection Institute (SÚRO) is the TSO (technical support organisation) of the regulatory body (State Office for Nuclear Safety). Its tasks consist of the assessment of licensing documentations and of performing confirmatory analyses, the latter being done by the Research and Analysis of Nuclear Safety Department. The department has a developing expertise in the fields of neutronics, thermo-hydraulics, severe accidents, structural mechanics and fuel performance. It also performs research in the frame of national and international (e.g. EU) projects.

Over the last two years fuel performance analyses in SÚRO have been put on a new footing. A new methodology is under development, covering a wider and wider range of conditions, large-scale batch analyses are being implemented, and BEPU methods are being introduced. In the paper this development is presented, including details of the methodology and some results.

1. Introduction

The Czech Republic is undergoing a very intense period of nuclear development. Within a few years four new fuel types have been or will be licensed, two large new commercial units have been contracted and siting and preparations have started for several small modular reactors.

The Czech National Radiation Protection Institute (SÚRO, a.k.a. NRPI) is the TSO (technical support organisation) of the regulatory body (State Office for Nuclear Safety, SÚJB). Its tasks consist, among others, of the assessment of licensing documentations and of performing confirmatory analyses, the latter being done by the Research and Analysis of Nuclear Safety Department. The department has a developing expertise in the fields of neutronics, thermo-hydraulics, severe accidents, structural mechanics and fuel performance. It also performs research in the frame of national and international (e.g. European Union) projects.

Over the last two years fuel performance analyses in SÚRO have been put on a new footing. A new methodology is under development, covering a wider and wider range of conditions, large-scale batch analyses are being implemented, and best estimate plus uncertainty (BEPU) methods are being introduced. In the paper this development is presented, including details of the methodology and some results.

2. Activities of the Research and Analysis of Nuclear Safety Department of SÚRO

The Czech National Radiation Protection Institute, SÚRO is a public research institute founded by the State Office for Nuclear Safety (SÚJB). It was established in 1995 as the scientific and technical support organisation to SÚJB in the field of radiation protection. What later became the Research and Analysis of Nuclear Safety Department was established outside of SÚRO and was appended to the institute in 2021, extending the role of the TSO to the field of nuclear safety. The department contributes to the work of the regulatory body by developing regulatory guidelines, assessing licensing documentation and doing confirmatory safety analyses.

The department has licenses for codes necessary for deterministic analyses, the interplay between the different fields is illustrated in Fig. 1, and follows the usual logic.

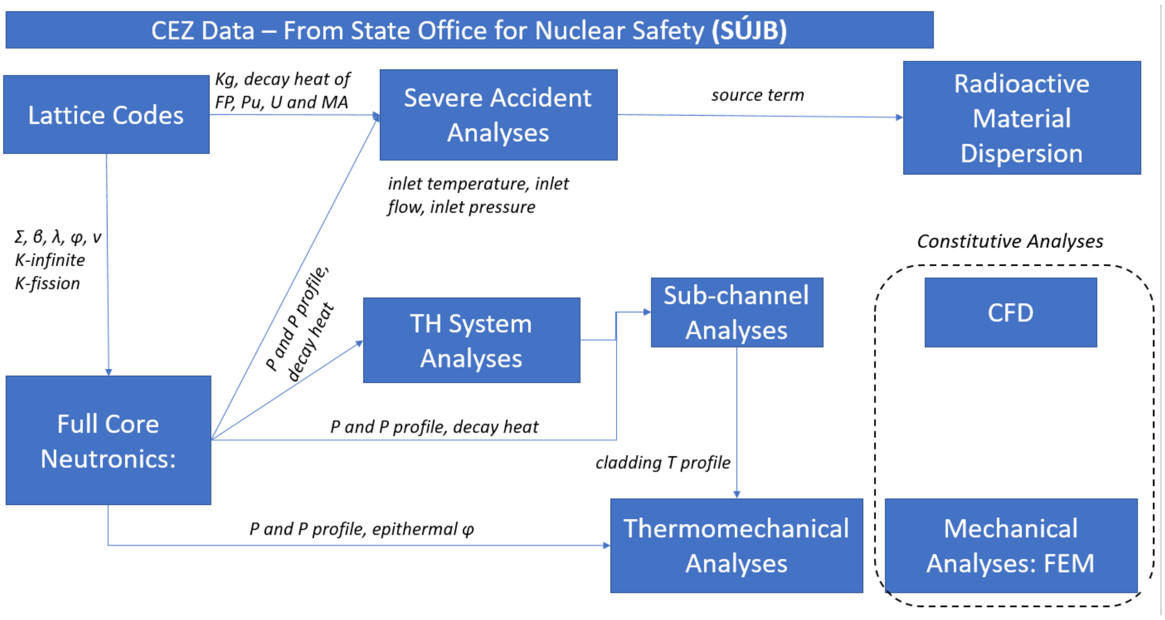

Figure 1. Interactions of codes for safety analysis

In addition to research on the national and international (e.g. EU) scene, the task of SÚRO as TSO is to perform on-demand confirmatory analyses, for which the basic data have to come from the utility, requested and passed on by the authority. This includes fabrication data, operational data and reload design. The whole subsequent independent workflow is based on these.

3. Fuel performance analysis at SÚRO

The thermo-mechanical code used in SÚRO is TRANSURANUS [1], developed by JRC Karlsruhe. The code can simulate both steady-state and transient processes, which makes it suitable to follow the entire life of a fuel rod up to an accident scenario without the need to restart it or to pass data over to a different code. Correlations for standard western claddings (Zircaloy, M5) as well as for Russian ones (E110) are included in the code. As the source code is part of the license SÚRO has, in-house development is also possible, e.g. the proprietary Westinghouse correlations for the Opt. ZIRLO cladding have been implemented in the in-house code version.

TRANSURANUS requires the typical input time series: steady-state and/or transient linear heat generation rates (LHRs), and for transients thermal-hydraulic boundary conditions. For normal operation and anticipated operational occurrences the code can calculate cladding temperatures based on the core inlet temperature and the LHR.

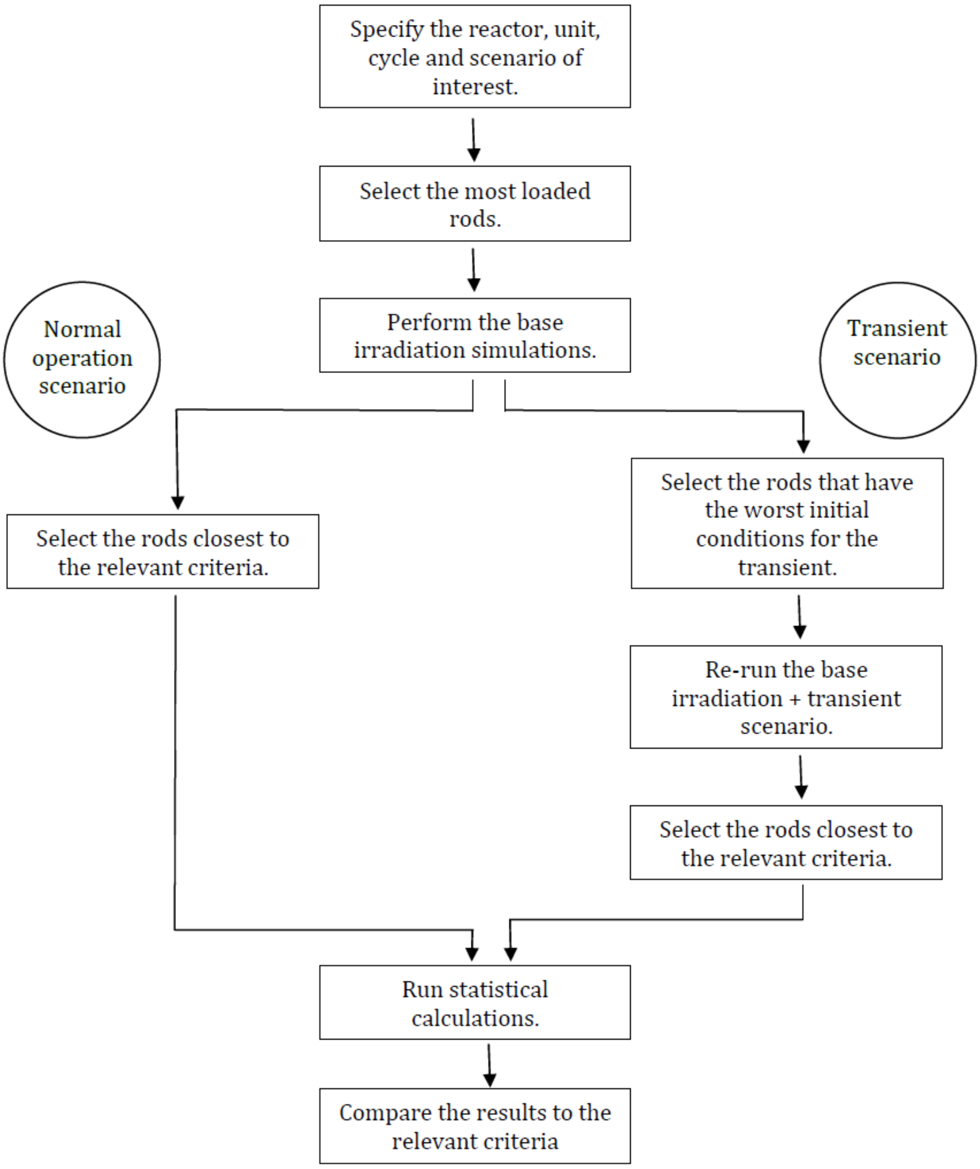

Figure 2. Methodology of the safety assessment of fuel performance

For any confirmatory analysis the first step is inevitably fuel performance analysis for normal operation. Since there are tens of thousands of rods in a core, it would be very much time and storage capacity consuming to simulate all of them, so a suitable set of enveloping rods are first selected. In each assembly and in each time step the rods with the

- highest local LHR,
- highest average LHR,
- highest change in LHR (if stresses are to be evaluated),
- highest local burnup,
- highest average burnup

are selected separately for UO_2 and UO_2+Gd_2O_3 rods, and all these rods are added to the pool of rods to be simulated. A best-estimated analysis is then performed on this conservative set of rods, which will be referred to as 'whole-core' best-estimate analysis in the following. Using the same selection process a conservative analysis can also be carried out.

If a BEPU analysis is required, first the best-estimate ‘whole-core’ analysis is performed, then the rods closest to the relevant criteria are subjected to Monte-Carlo analysis (a feature built into TRANSURANUS) to determine the uncertainties of the simulations.

For transient or accident analyses first the best-estimate ‘whole-core’ analysis is performed again, up to the moment of the transient, then the rods with the worst initial conditions for the transient are selected based on the TRANSURANUS outputs (for loss-of-coolant accident, LOCA, e.g., those with the highest internal pressure and the highest local LHR, in pre-defined burnup bins of, e.g., 3 or 5 MWd/kgU), and finally the whole history of the steady-state base irradiation and the transient is simulated for these rods. Monte Carlo runs for the rods achieving parameters closest to the acceptance criteria make the analysis complete. The procedure is summarised in Fig. 2.

The development of the programs that perform all this is in progress. At the moment steady-state ‘whole-core’ analysis can be performed for a uniform core. Developments in progress are steady-state analysis for mixed core, statistical calculations and LOCA analysis. The next big step in the near future will be 3D transient problems.

4. Illustrative results

In the following a few results of best-estimate steady-state analyses for a ‘whole’ uniform equilibrium core are presented as examples. Each graph represents the relative value of a parameter that has a design limit associated to it, with respect to the design limit. Each point represents the highest value for a given rod.

As expected, all the results are far below the limits, higher values are to be expected when adding uncertainties, and, especially, for transition cycles with mixed cores.

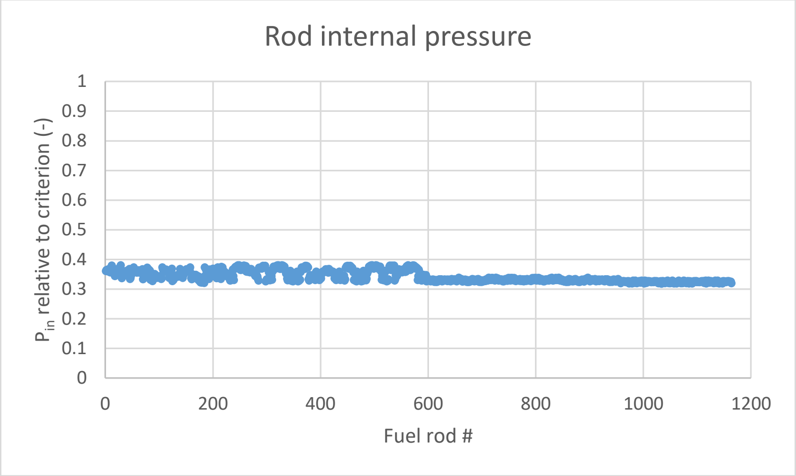

Figure 3. Rod internal pressure relative to criterion, uniform equilibrium core

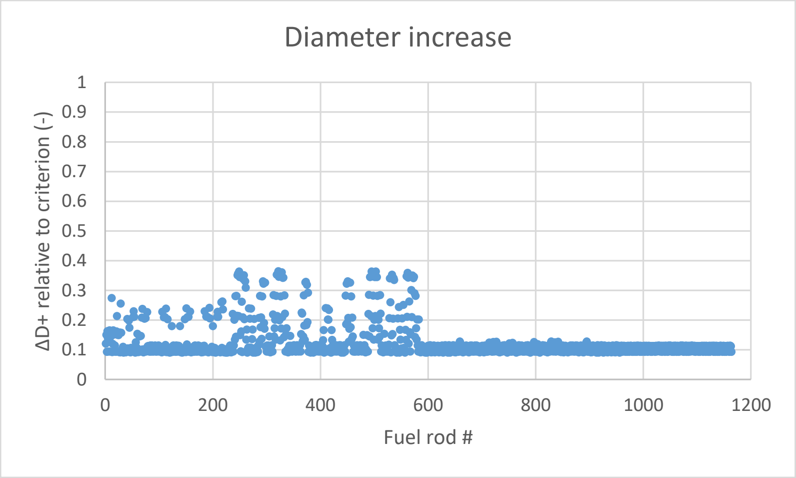

Figure 4. Rod diameter increase relative to criterion, uniform equilibrium core

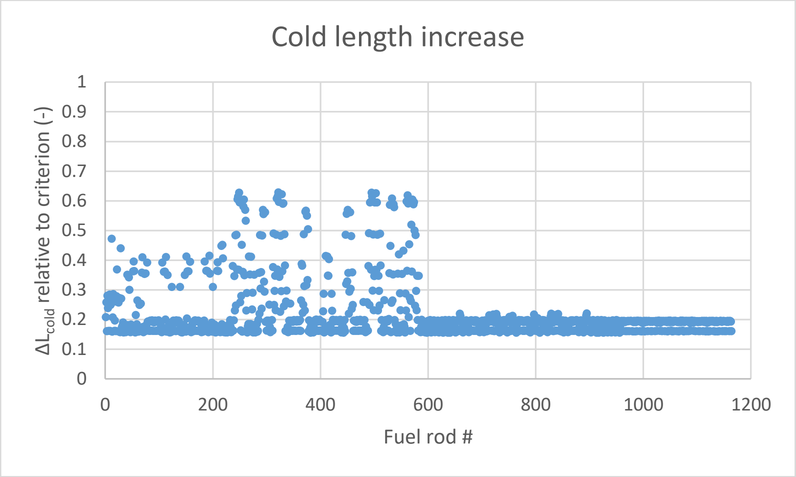

Figure 5. Cold length increase relative to criterion, uniform equilibrium core

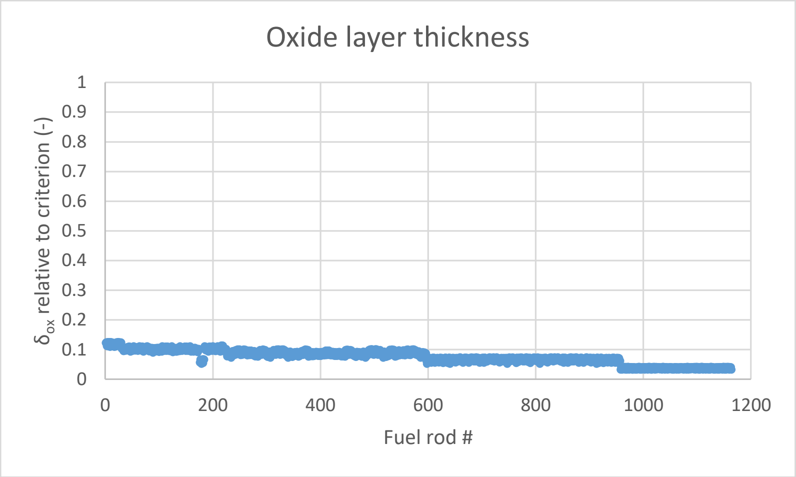

Figure 6. Oxide layer thickness relative to criterion, uniform equilibrium core

5. Recent and near-to-medium-term applications

The Research and Analysis of Nuclear Safety Department of SÚRO has recently performed confirmatory safety analyses for the transition of the Temelín Nuclear Power Plant (NPP) from 12-month to longer (18-month) cycles using the fuel TVSA-T.Mod.2 from the Russian vendor TVEL. Similar analyses are either in preparation or already ongoing for the transition to the new fuels RWFA-T (for Temelín NPP) and NOVA E-6 (for Dukovany NPP) from Westinghouse. New reactors are also envisaged and will undergo the licensing process, including confirmatory analyses: two units of APR1000 from Korea Hydro & Nuclear Power Co., Ltd. (KHNP) for the Dukovany site have been contracted, and several small modular reactor (SMR) units are considered for different sites in the Czech Republic. This will give much work to the department in the coming years.

4. Conclusions

SÚRO is in the process of developing the capabilities necessary for the full-scope confirmatory analyses in the field of fuel performance. The analyses are performed using the code TRANSURANUS. The aim is to be able to do all the safety analyses independently.

The development of fuel performance analyses follows the developments in neutronics and thermal-hydraulics. However, temporarily these input data can be provided by the licensee.

Acknowledgement

The work is financed by the State Office for Nuclear Safety.

References

[1] K. Lassmann, TRANSURANUS: a fuel rod analysis code ready for use, Journal of Nuclear Materials 188 (1992) 295.

Spent Nuclear Fuel Management of Ukrainian Nuclear Operator

Roman Glushenkov[1*]

[1]JSC "NNEGC "Energoatom"

[*]E-mail: *rs.glushenkov@gmail.com*

Abstract. The way a country manages its spent nuclear fuel is primarily determined by the type of nuclear fuel cycle it employs, which is broadly categorized into two main approaches: open (or once-through) and closed fuel cycles. There are several options for the final stage of the fuel cycle (spent fuel management):

- Spent fuel reprocessing: the process involves chemically separating reusable uranium and plutonium from spent fuel so they can be returned to the fuel cycle. The highly radioactive fission products are isolated as high-level waste, which subsequently requires long-term storage.
- Deferred solution: This approach involves storing spent fuel in temporary facilities, either at reactor sites or at centralized interim storage facilities, without immediate reprocessing or permanent disposal.
- Direct disposal: this strategy involves preparing spent fuel (after optional interim storage) for direct emplacement in deep geological repositories without prior reprocessing.

Ukraine's current spent nuclear fuel management scheme is focused on a deferred solution (interim dry storage), aiming for long-term storage within the country and reducing its historical reliance on Russia for reprocessing and storage. Key elements of Ukraine's strategy include:

Initial storage in on-site spent fuel pools (wet storage), which allows sufficient time for the fuel to cool and its residual heat and radioactivity to decay to levels safe for subsequent handling and transport. Once sufficiently cooled, the spent fuel is then transferred to a dry spent fuel storage facility.

The Centralized Spent Nuclear Fuel Storage Facility, located in the Chernobyl Exclusion Zone, which receives spent nuclear fuel from Rivne, Khmelnytskyi, and Pivdennoukrainsk NPPs.

The On-site Dry Spent Fuel Storage Facility at Zaporizhzhia NPP, which stores spent nuclear fuel generated by Zaporizhzhia NPP.

Energoatom's spent nuclear fuel management represents a significant move towards self-sufficiency and strategic independence within a challenging geopolitical environment, while laying the groundwork for eventual permanent disposal solutions.

Keywords: spent nuclear fuel management, interim dry storage, deferred solution

1. Spent nuclear fuel management

The way a country manages its spent nuclear fuel is primarily determined by the type of nuclear fuel cycle it applies, which is widely categorized into two main approaches:

- The Open fuel cycle.
- The Closed fuel cycle.

There are several strategies for the final stage of the fuel cycle (spent fuel management):

- Spent fuel reprocessing: this process involves chemically separating reusable uranium and plutonium from spent fuel so they can be returned to the fuel cycle. The highly radioactive fission products are isolated as high-level waste, which then requires long-term storage.
- Deferred solution: This approach involves storing spent fuel in temporary facilities, either at NPP sites or at centralized interim storage facilities, without immediate reprocessing or permanent disposal.
- Direct disposal: this strategy involves preparing spent fuel (after optional interim storage) for direct emplacement in deep geological repositories without prior reprocessing.

A review of global experience in the field of spent nuclear fuel management does not currently allow for an indisputable choice of a single promising strategy that would best meet the needs of any country. Many countries (see table 1) have not yet decided and continue to store spent nuclear fuel (hereinafter referred to as SNF) until a final strategy is chosen (the so-called "deferred solution").

Table 1. *Spent nuclear fuel management strategies by country.*

Country	Deferred solution	Direct disposal	Reprocessing
Belgium	+	-	+*
Slovakia	+	-	-
Czech Republic	+	-	-
Hungary	+	-	-
United Kingdom	-	+	+*
India	-	-	+*
USA	-	+	+*
Ukraine	+	-	-
Canada	-	+	-
China	-	-	+
Germany	-	+	+*
Russian Federation	-	-	+
Finland	-	+	-
France	-	-	+
Sweden	-	+	-
Japan	-	-	+

* – partial reprocessing

The solution to the problem in a particular country should largely be found in the strategies for organizing the nuclear fuel cycle, and this, in turn, depends on national priorities and the energy development program.

2. Ukrainian nuclear operator

The JSC “National nuclear energy generating company "Energoatom" (hereinafter referred to as Energoatom) is the company operating all four nuclear power plants in Ukraine (Zaporizhzhia, Rivne, South Ukrainian, and Khmelnytskyi). It is the largest producer of electricity in Ukraine and operates 15 units (13 VVER-1000 and 2 VVER-440 reactors), two hydroelectric units at the Oleksandrivska Hydroelectric Plant, and three hydroelectric units at the Tashlyk Pumped-Storage Power Plant. The company also owns the Centralized Spent Fuel Storage Facility in the Chornobyl zone.

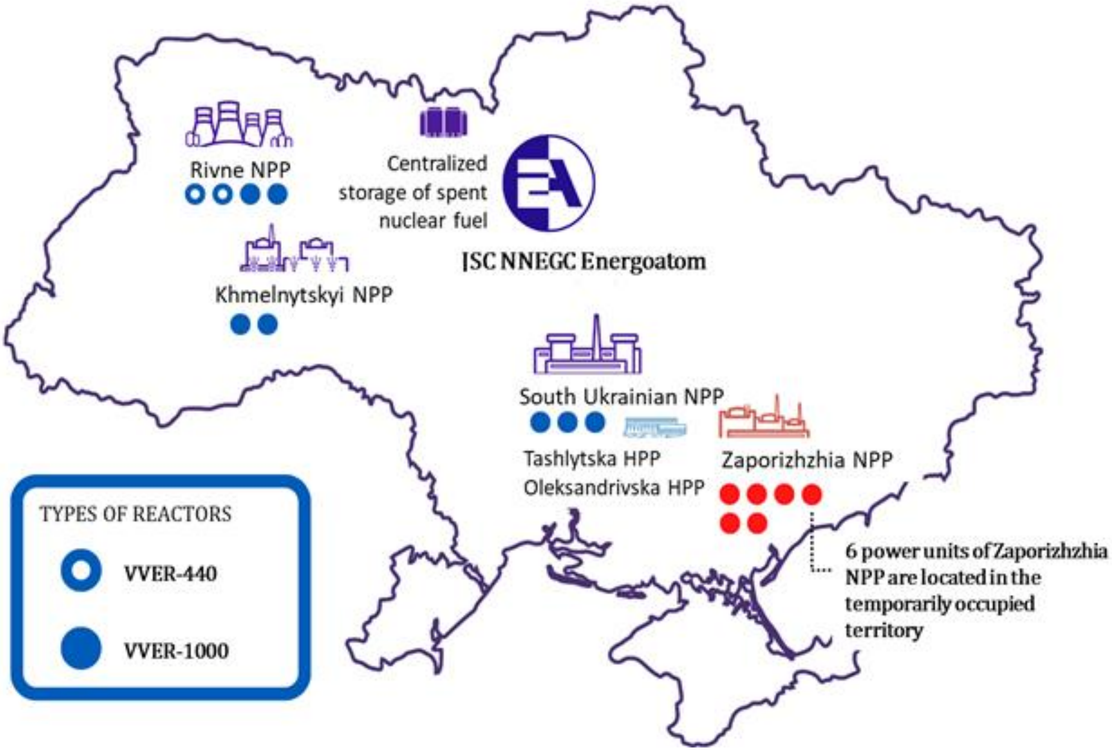

Figure 1. Energoatom’s current state

On March 4, 2022, during the Russian aggression the Zaporizhzhia NPP came under temporary occupation. The current situation is shown in figure 1.

3. Energoatom’s nuclear fuel management

Nuclear fuel management is an integral part of the technological process of electricity production. Energoatom's nuclear fuel management represents a significant move towards self-sufficiency and strategic independence from the Russian Federation historical dependence.

3.1 Historical dependence on the Russian Federation

Due to objective reasons, the Energoatom's nuclear fuel management was dependent on the Russian Federation. According to the figure 2, "front end" and "back end" were historically managed by a number of Russian companies.

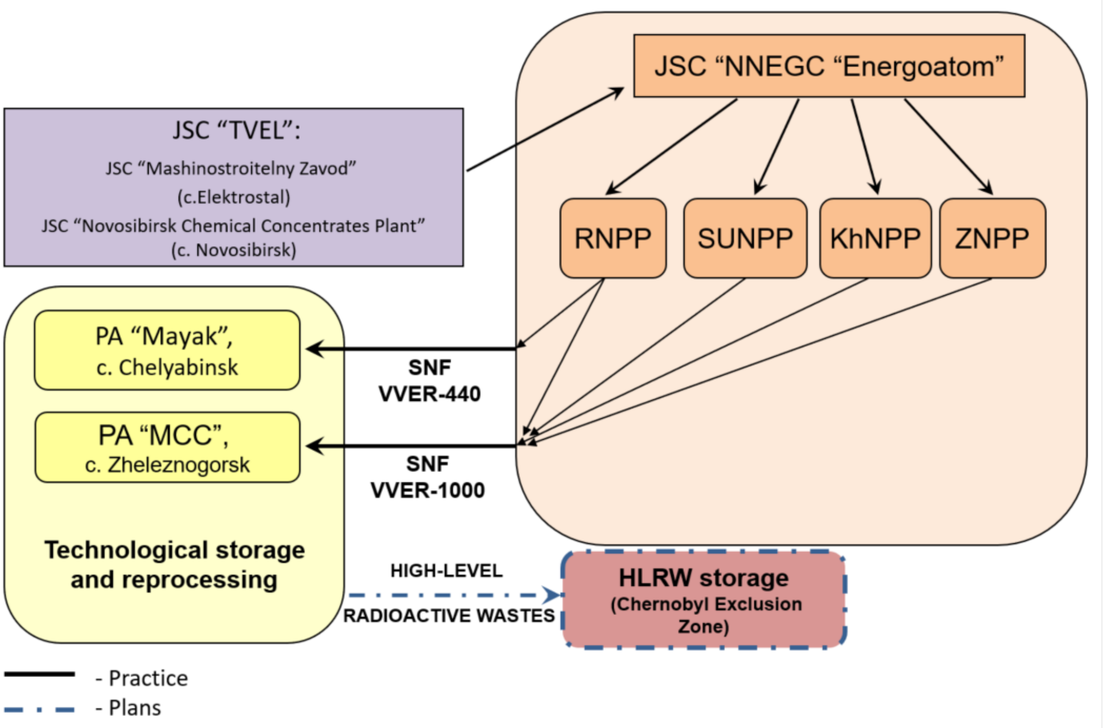

Figure 2. Retrospective Energoatom's nuclear fuel management

That is why the diversification of the fresh fuel supply project with Westinghouse was initiated and spent nuclear fuel management scheme was reoriented toward interim dry storage within the country.

3.2 Current Energoatom's nuclear fuel management

As we can see from the figure 3, Energoatom supplies nuclear fuel produced by Westinghouse for all of its units. RWFA for VVER-1000 and NOVA E-5/NOVCC for VVER-440 reactors. Energoatom's nuclear fuel management is completely independent of the Russian Federation. Also, Energoatom is a participant of the APIS project. APIS (Accelerated Program for Implementation of secure VVER fuel Supply) indicates that the European countries operating VVER reactors have an urgent need to qualify an alternative fuel supplier to secure the future power generation.

Ukraine's current spent nuclear fuel management scheme is focused on deferred solution (interim dry storage), aiming for long-term storage within the country and reducing its historical reliance on Russia for reprocessing and storage.

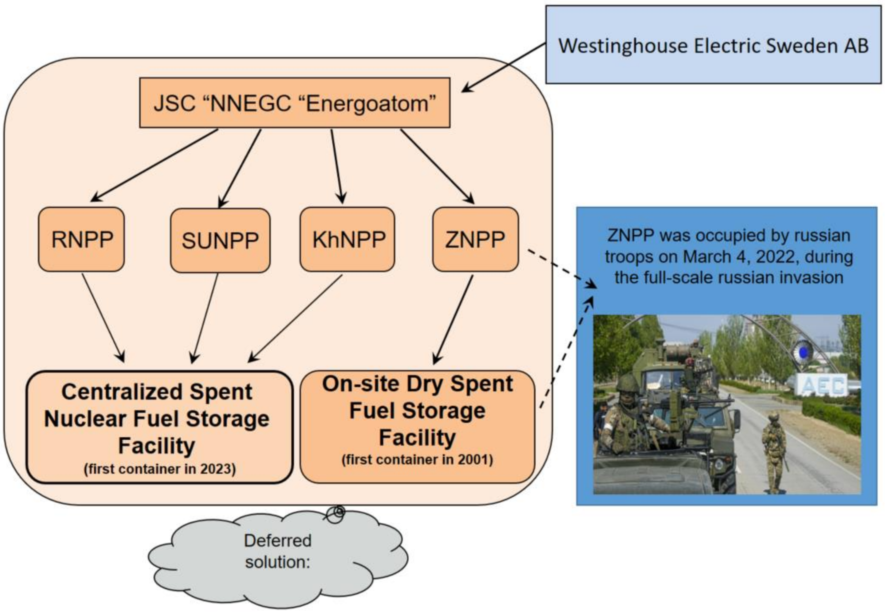

Figure 3. Energoatom's nuclear fuel management

4. Energoatom's spent nuclear fuel management

Key elements of Energoatom's SNF management include (figure 4):

- Initial storage in on-site spent fuel pools (wet storage), which allows sufficient time for the fuel to cool and its residual heat and radioactivity to decay to levels safe for subsequent handling and transport. Once sufficiently cooled, the spent fuel is then transferred to a dry spent fuel storage facility.
- The Centralized Spent Nuclear Fuel Storage Facility, located in the Chernobyl Exclusion Zone, which receives spent nuclear fuel from Rivne, Khmelnytskyi, and Pivdennoukrainsk NPPs.
- The On-site Dry Spent Fuel Storage Facility at Zaporizhzhia NPP, which stores spent nuclear fuel generated by Zaporizhzhia NPP.

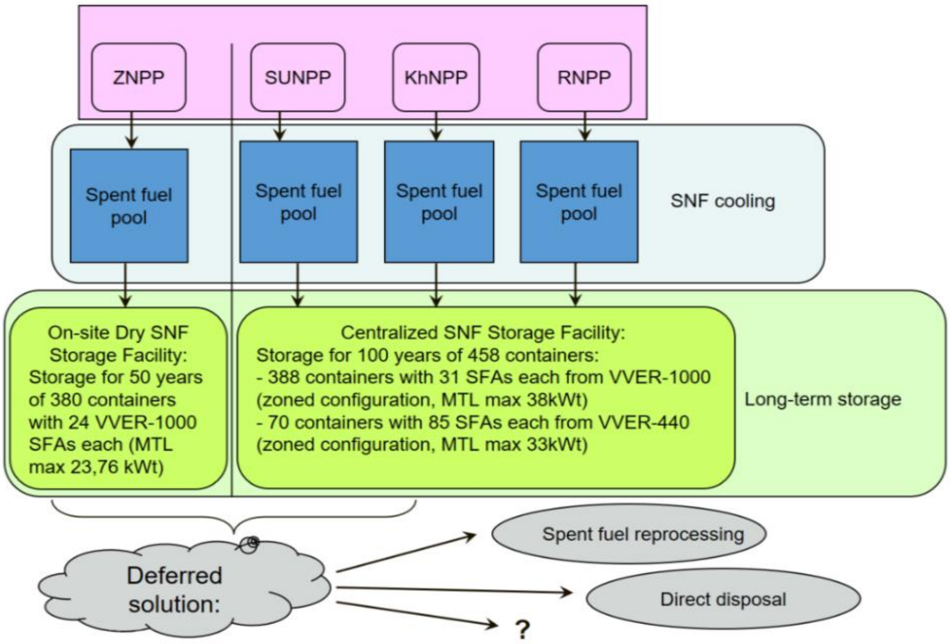

Figure 4. Key elements of Energoatom's SNF management

4.1. ZNPP On-site Dry Spent Fuel Storage Facility

The facility is located at Zaporizhzhia NPP. The design of Sierra Nuclear Corporation and Duke Engineering & Services was selected. The fuel is stored in sealed canisters (figure 5), where the VVER-1000 fuel is in an inert gas environment. The canister is placed through a reloading container inside an air-ventilated concrete container for long-term (50 years) storage.

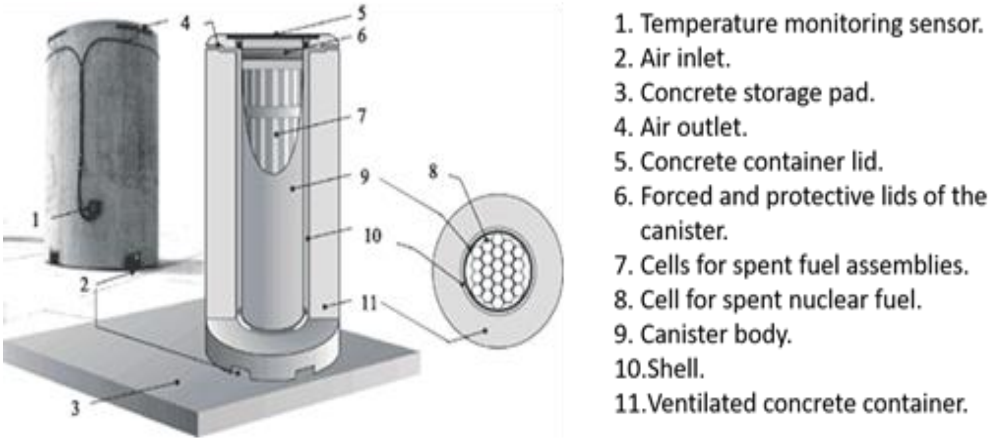

1. Temperature monitoring sensor.
2. Air inlet.
3. Concrete storage pad.
4. Air outlet.
5. Concrete container lid.
6. Forced and protective lids of the canister.
7. Cells for spent fuel assemblies.
8. Cell for spent nuclear fuel.
9. Canister body.
10. Shell.
11. Ventilated concrete container.

Figure 5. Air ventilated container with canister

Figure 6 schematically demonstrates the overall reloading process. Figure 7 demonstrates the general view of the site.

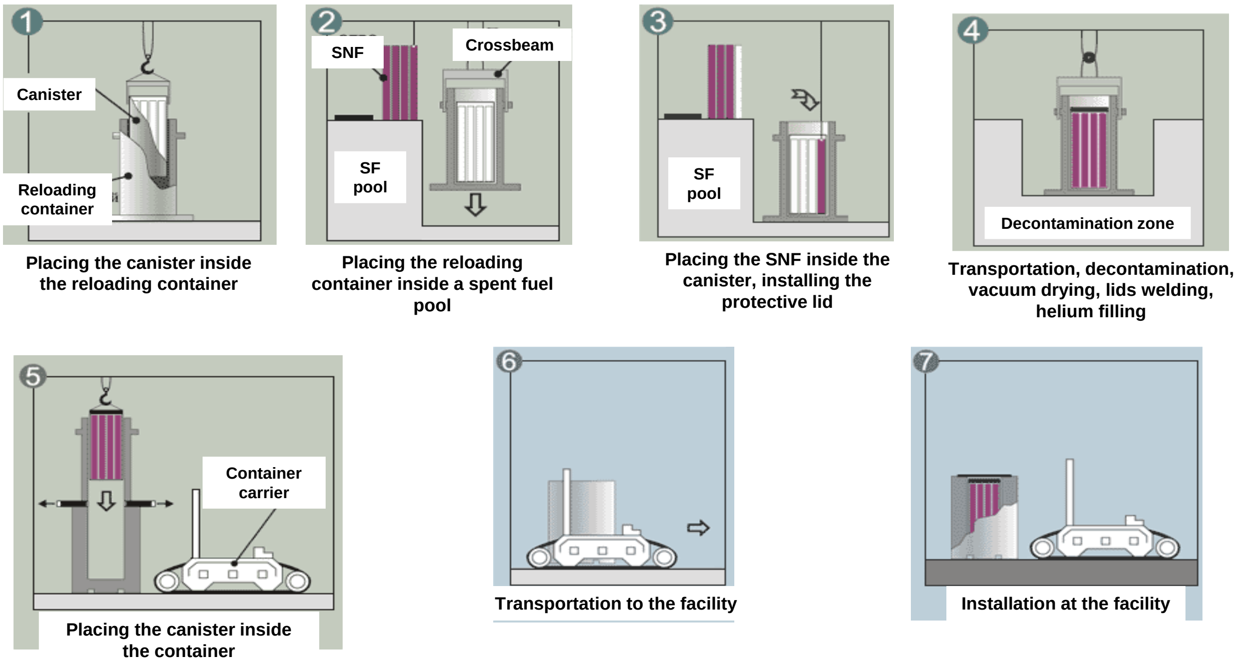

Placing the canister inside the reloading container

Placing the reloading container inside a spent fuel pool

Placing the SNF inside the canister, installing the protective lid

Transportation, decontamination, vacuum drying, lids welding, helium filling

Placing the canister inside the container

Transportation to the facility

Installation at the facility

Figure 6. Reloading process

Figure 7. General view by the site

4.2 Centralized spent nuclear fuel storage facility
The facility is located in the Chernobyl Exclusion Zone. The design of Holtec International was selected. The facility is designed for storage of VVER-1000 and VVER-440 spent nuclear fuel from three NPPs (Rivne, South Ukrainian, and Khmelnytskyi).

SNF is stored in Multi-Purpose Canisters (hereinafter referred to as MPCs) filled with an inert gas environment. MPC is placed through a HI-TRACK container inside a transportation and storage HI-

STAR container for the transportation to the facility. At the facility MPCs are reloaded to air-ventilated HI-STORM containers for long-term (100 years) storage. The overall scheme is demonstrated on the figure 8.

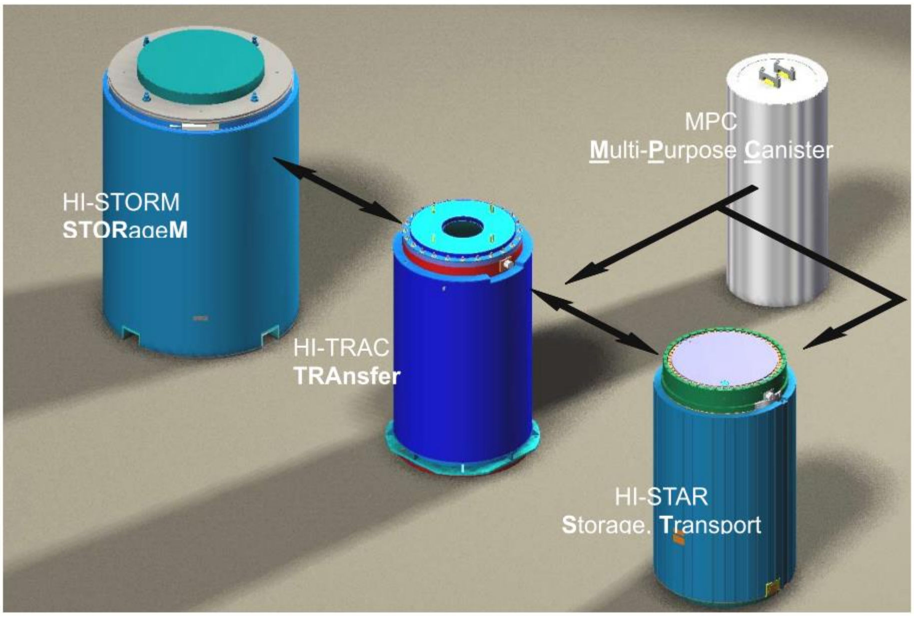

Figure 8. Operated containers

The main approach includes the following stages:

- Stage 1. The equipment transportation to and technological operations at the NPP.
- Stage 2. HI-STARs transportation to the facility by specialized railway train.
- Stage 3. Technological operation at the facility with MPCs reloading to HI-STORMs.
- Stage 4. Installation of HI-STORMs for the long-term storage.

4.2.1 Stage 1

Spent nuclear fuel (SNF) is loaded into a multi-purpose canister (MPC). Two types of MPCs are applied: MPC-31 – for 31 SFAs of VVER-1000 and MPC-85 – for 85 SFAs of VVER-440 (figure 9). Loaded MPC is hermetically sealed and dried. MPC is transferred from HI-TRACK to HI-STAR (figure 10).

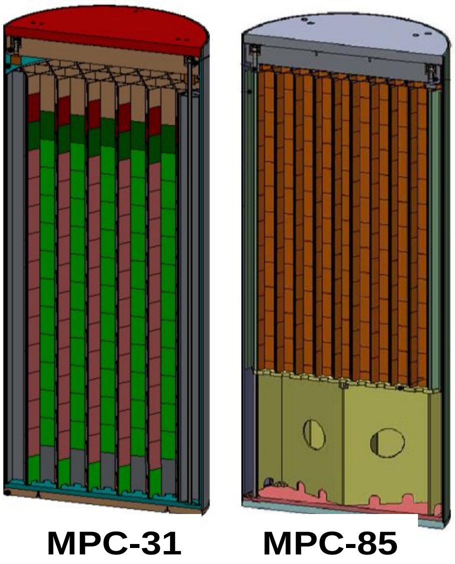

Figure 9. MPCs

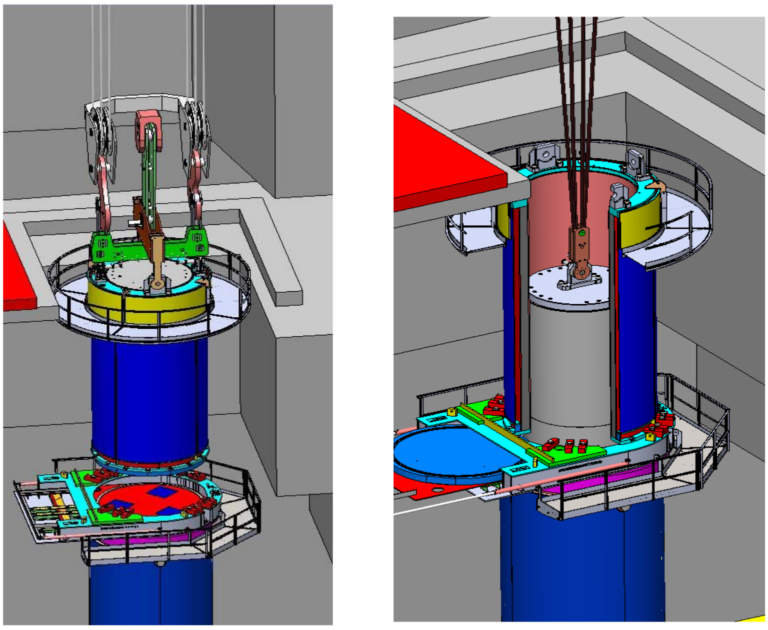

Figure 10. Loading MPC to HI-STAR through HI-TRACK

4.2.2 Stage 2

The delivery of spent nuclear fuel from NPP to the facility is carried out by rail transport. HI-STARs (figure 11) are located on special railcars (figure 12) in horizontal position.

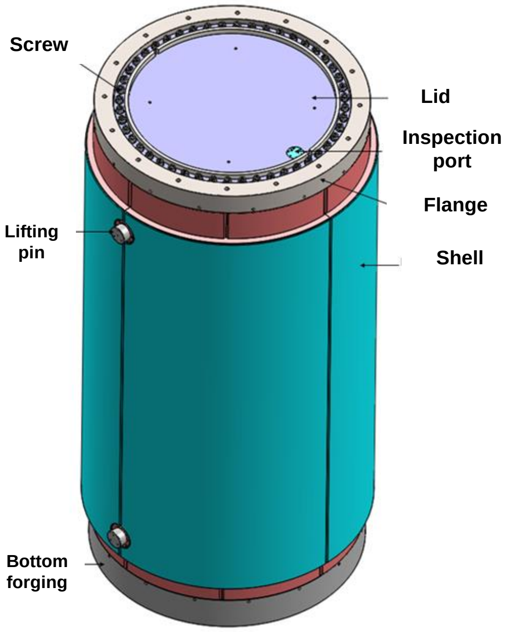

Figure 11. HI-STAR

Figure 12. HI-STAR on the rail transport

4.2.3 Stage 3

After the train arrival to the facility, the special railcar with the HI-STAR is transported to the Receiving building. In the building the HI-STAR is placed into a special node for reloading the MPC from the HI-STAR to the HI-STORM (figure 13).

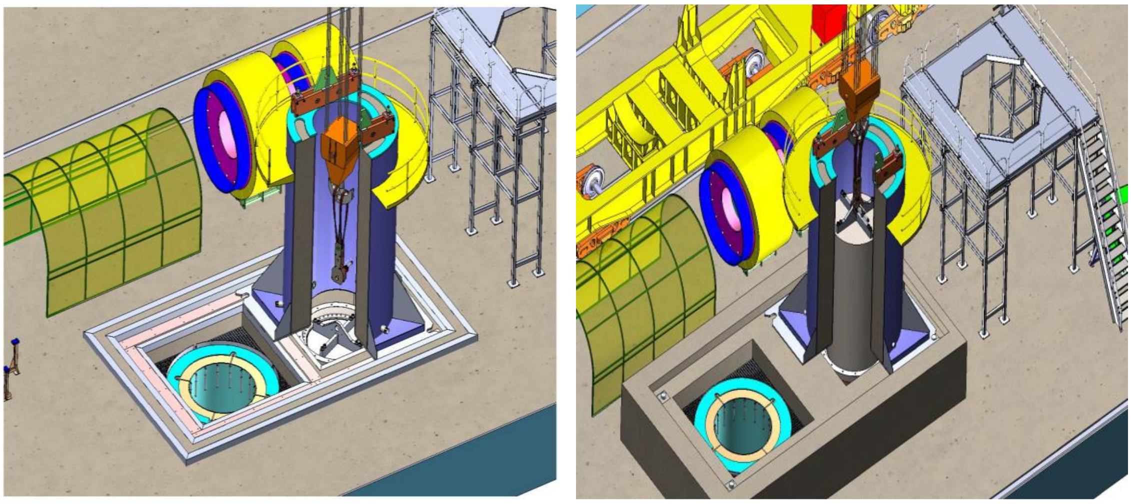

Figure 13. Special node for reloading the MPC from the HI-STAR to the HI-STORM

4.2.4 Stage 4

Installation of a HI-STORM for the long-term storage is performed with a specialized container carrier (figure 14).

Figure 14. Specialized container carrier

The container is placed on specified area at the site for the long-term storage (figure 15).

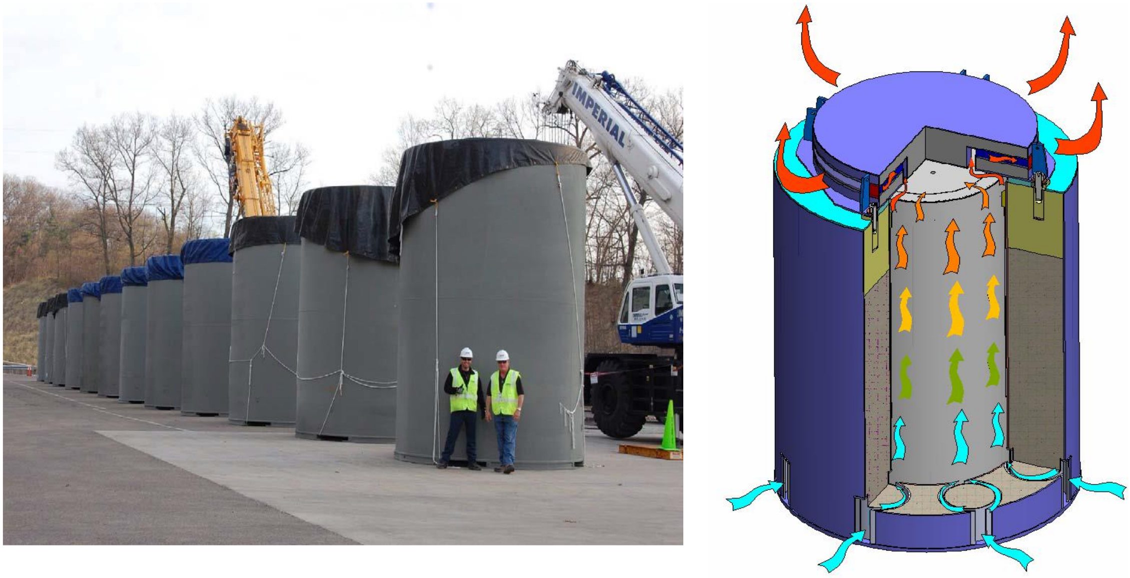

Figure 15. Long-term storage of HI-STORM

4. Conclusions

- A review of global experience in the field of spent nuclear fuel management does not currently allow for an indisputable choice of a single promising strategy that would best meet the needs of any country.
- The solution to the problem in a particular country should largely be found in the strategies for organizing the nuclear fuel cycle, and this, in turn, depends on national priorities and the energy development program.
- Ukraine's current spent nuclear fuel management strategy is focused on deferred solution (interim dry storage), aiming for long-term storage within the country and excluding its historical dependence on Russia for reprocessing and storage.
- Energoatom's spent nuclear fuel management represents a significant move towards self-sufficiency and strategic independence within a challenging geopolitical environment.

Advanced Digital Image Processing for Material Evaluation in Nuclear Applications

Ondřej Pašta[1*], Jaroslav Knotek[1], Jan Blažek[1,2] and Marcin Kopeć[1]

[1]Research Centre Řež, Hlavní 130, Řež, 250 68 Husinec, Czech Republic
[2]Institute of Information Theory and Automation of the CAS, Prague 18208, Czech Republic

[*]E-mail: *ondrej.pasta@cvrez.cz*

Abstract. The integration of Digital Image Processing (DIP) with neural networks and Artificial Intelligence (AI) has significantly transformed the way microstructures are analyzed in materials science. In nuclear applications, these technologies have become standard tools—from fuel assembly inspections to high-resolution electron microscopy—enabling the conversion of imaging data from SEM/TEM and other modalities into quantitative information across scales. At the Research Centre Řež (CVR), DIP and AI have accelerated processing, standardized workflows, and improved data reproducibility. A key example is the detection and classification of precipitates: secondary phase particles (SPP) from manufacturing and heat treatment, and radiation-induced precipitates (RIP) formed under neutron flux and diffusion. Their morphology, size, and distribution directly influence mechanical properties such as hardness, brittleness, and internal stresses. While SPP formation can be controlled by alloy composition and processing, RIP characterization is essential for Post-Irradiation Examination (PIE). DIP is equally critical for non-invasive assessment of reactor biological shielding concrete, detecting and tracking cracks, and enabling volumetric damage evaluation, with results cross-validated by conventional NDT methods like ultrasonics. For fuel inspections, DIP transforms video sequences into consistent, high-resolution images without loss of context. Overall, the developed approaches support long-term operation (LTO) strategies by enabling faster, more reliable interpretation of nuclear materials data. Beyond the nuclear sector, the methodology is transferable to domains like construction and metallurgy, where precise microstructural analysis is equally critical.

Keywords: materials science, image analysis, PIE, precipitates, shielding concrete

1. Introduction

Safe and reliable operation of nuclear power plants is a cornerstone of energy infrastructure. As reactors age, long-term operation (LTO) strategies aim to extend lifetimes from the original 30–40 years up to 60, 80, or even beyond. Achieving this requires accurate diagnostics of degradation phenomena under combined thermal, mechanical, and radiation loads. Special attention is given to biological shielding concrete, whose integrity protects personnel and systems from neutron and gamma radiation. However, long-term performance is challenged by radiation-induced volumetric expansion (RIVE) of quartz aggregates and chemical degradation driven by water radiolysis, leading to microcracking and reduced stiffness and strength.

Another critical focus includes reactor pressure vessels and internals, especially fuel cladding and assemblies. Neutron flux, thermal gradients, and mechanical stresses alter the microstructure via secondary phase particles (SPP) and radiation-induced precipitates (RIP), which strongly affect fracture toughness and hardness. Reactor conditions may involve neutron fluences exceeding 1×10^{19} n/cm², gamma doses up to hundreds of MGy, and temperatures above 90 °C.

Recent advances in DIP and AI have enabled precise, high-throughput analysis of structural changes. At CVR, these methods have been integrated into SEM/TEM imaging, fuel visual inspections, and shielding concrete studies, enhancing objectivity and reproducibility in PIE. This paper summarizes three domains: (1) fuel assembly inspections, (2) microcrack detection in shielding concrete, and (3) precipitate characterization in cladding materials. [1-9]

2. Materials and Methods

The presented results are based on experiments and inspections at CVR, where DIP and AI tools have been deployed across nuclear research fields. Analyzed materials included fuel assemblies, claddings, shielding concrete, and irradiated structural alloys. Automated workflows were implemented in Python and MATLAB using OpenCV, scikit-image, and TensorFlow for image labeling, neural network training, and batch processing of terabyte-scale datasets. Results were cross-validated with conventional methods (ultrasonics, profilometry). For concrete, crack parameters were correlated with mechanical properties such as compressive strength, Young's modulus, and porosity. [10-12]

2.1 Shielding Concrete: RIVE and Cracking

Specimens reflected historical VVER-type shielding concrete compositions emphasizing quartz aggregates prone to RIVE. Cracks were evaluated under controlled thermal and radiation conditions using high-resolution imaging and DIP, enabling quantification of crack initiation, propagation, and deformation fields in 2D and 3D. [5] The samples that were investigated within this work are presented in Figure 1.

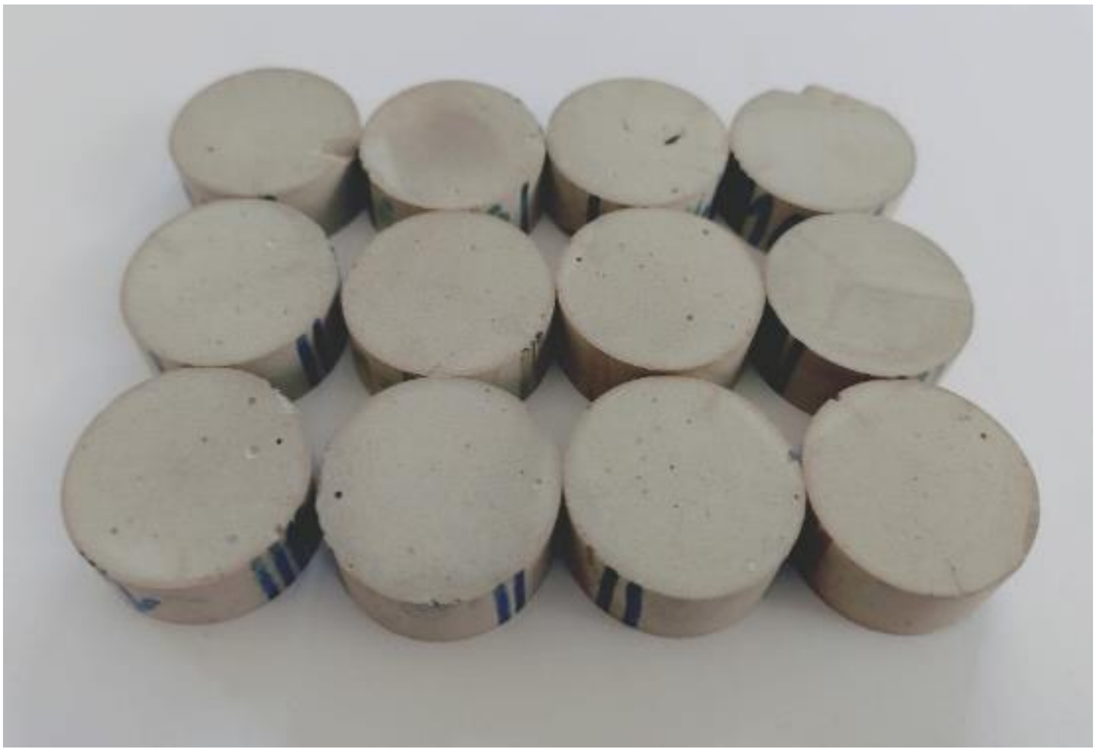

Figure 1. Concrete shielding samples.

2.2 Fuel Cladding: Microstructural Evolution

Irradiation-induced microstructural changes in cladding alloys were assessed using SEM/TEM imaging. DIP algorithms performed image segmentation and particle analysis, extracting morphology, size, and spatial distribution of precipitates. Workflows included contrast enhancement, noise filtering, thresholding, and segmentation using neural networks trained on annotated datasets. [6-7]

2.3 Fuel Assemblies: Geometric Verification

Fuel rod deformations—bowing, twisting, axial growth—were analyzed from hot cell video sequences. Frames were stabilized, denoised, and assembled into continuous composites at ~0.2 mm spatial resolution, enabling cycle-to-cycle dimensional tracking. For creep evaluation, small cladding specimens were imprinted with reference grids (e.g., Vertex) and optically tracked before and after irradiation to quantify deformation under LTO-relevant stresses. [8,13-16]

3. Results

During operation, fuel rods experience deformation from thermal loads, hydraulic forces, and irradiation-induced swelling.[17] Manual inspections are subjective and limited in resolution.[18] DIP enables automated, high-resolution reconstruction, achieving sub-millimeter accuracy in geometric tracking. [19-22] Frames are stabilized, denoised, and stitched, while CNN-based detection tracks anomalies over time. These methods are routinely applied at CVŘ to support licensing, design optimization, and PIE.

For post-irradiation evaluation, images are pre-processed before nanoindentation grid analysis. Low-frequency background variations are suppressed via grayscale morphological erosion, scratches smaller than indents are removed using morphological opening, and thresholding isolates high-intensity regions. Connected components are identified and modeled with Delaunay triangulation, followed by filtering based on grid regularity rules to remove false edges and nodes. Missing indents are reconstructed by interpolation where possible; otherwise, manual review is required.

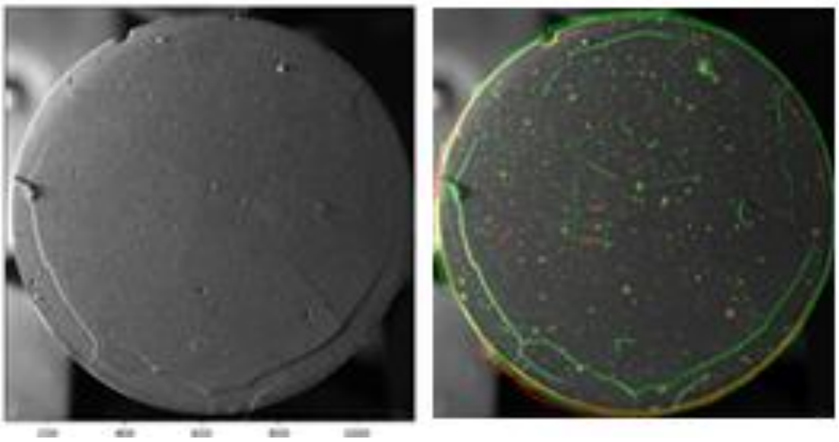

Figure 2. Original registered image (left) and processed outputs of crack, pores, and scratches detection in the binary system (right).

Crack detection in concrete often requires expert interpretation. A manually annotated dataset of ~100 frames, labeled independently by three experts, was created for cross-validation, model training, and validation of automated tools. Extracted crack parameters include count, length, width, perimeter, and maximum extent, enabling quantitative assessment of damage severity. Results showed a strong correlation with ultrasonic and acoustic NDT data. The graphical output from data processing is visible in Figure 2.

Maintaining the microstructural stability of fuel cladding is essential for its mechanical performance. At CVR, DIP-assisted analysis of SEM/TEM images enabled detailed quantification of SPPs and RIPs, including particle size, shape, and spacing, which were statistically assessed.

Three datasets were used in the evaluation. The main dataset was a labeled test set for quantitative model assessment. Two auxiliary datasets—a portion of unreliable training data and a set of unlabeled data—were used only for visual validation. For each dataset image, a folder was created with: the input image (Img.png), raw model predictions (Prediction_continuous.png), a CSV of particle properties (Precipitates.csv), an overlay visualization (Plot_visualized.png), and a histogram of particle sizes in micrometers or pixels (Histogram_[µm/px].png). The inputs and outputs can be seen in Figure 3.

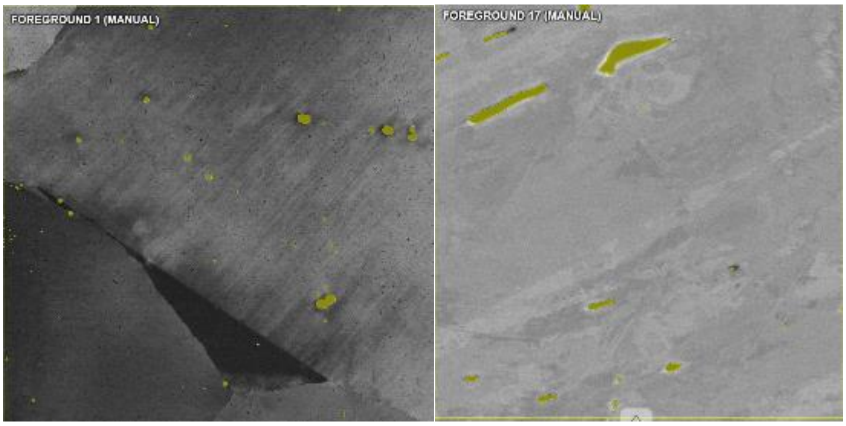

Figure 3. Automatic evaluation of precipitates using an algorithm.

Model performance was based on the labeled test set, with predictions thresholded at 0.5 and averaged across all images. Hyperparameter tuning produced similar outcomes across settings, and the three best (by F1 score) are shown in Table 1.

Table 1 - Summarizes precision, recall, and F1 scores for three top-performing model configurations.

Configuration	Precision	Recall	F1 Score
I	0,8231	0,9400	0,8611
II	0,8560	0,9131	0,4935
III	0,7509	0,8705	0,8000

All three achieved F1 scores above 0.81. Configuration I gave the best balance of precision and recall. Configuration II maximized precision, while III reached the highest recall but with slightly lower precision.

Removing poorly labeled training data improved results by 1–2 F1 points, confirming that discarding low-quality labels enhances predictive reliability. A further experiment compared human labelers with the model. Using the average labeler judgment as ground truth, discrepancies highlighted the model's precision. Results, combining F1 and IoU, were derived from five challenging photo-samples evaluated in one uninterrupted session to ensure consistency. The outputs are presented in Table 2.

Table 2 - Compares model performance with min/max labeler scores across five challenging samples.

Configuration	IoU			F1		
	Min	Max	Model	Min	Max	Model
1	0,8231	0,9400	0,8611	0,9143	0,9677	0,7781
2	0,8560	0,9131	0,4935	0,8172	0,9620	0,7253
3	0,7509	0,8705	0,8000	0,6905	0,9818	0,5184
4	0,3371	0,7454	0,5727	0,1680	0,8663	0,3667
5	0,8293	0,9554	0,9383	0,9620	1,0000	0,8320

4. Conclusions

Integrating DIP and AI into nuclear materials research has transformed diagnostics at CVR. Across fuel inspections, shielding concrete assessments, and cladding microstructure analysis, these methods improved data quality, reduced human bias, and accelerated inspection cycles. Automated workflows, advanced segmentation, and machine learning enabled efficient processing of large imaging datasets with high accuracy. Beyond nuclear applications, the principles are transferable to civil engineering, aerospace, and metallurgy. Future development aims at greater automation, multimodal data fusion, and scaling toward near-real-time applications.

Acknowledgements:
We acknowledge the state support of the Technology Agency of the Czech Republic within the National Competence Centre Programme II, project TN02000012 „Center of Advanced Nuclear Technology II“.

The presented results were obtained using the CICRR infrastructure, which is financially supported by the Ministry of Education, Youth and Sports - project LM2023041.

References

[1] J.T. Busby et al., “Materials Degradation in Light Water Reactors: Life After 60?”, Oak Ridge National Laboratory, 2008.
http://doi.org/10.2172/938766

[2] L.J. Bond, “Moving Beyond NDE to Proactive Management of Materials Degradation,” in Proc. ASME Pressure Vessels and Piping Conf. (PVP), 2010.
http://doi.org/10.1115/PVP2010-26174

[3] T.S. Byun et al., “Degradation of impact toughness in cast stainless steels during long-term thermal aging,” J. Nucl. Mater., vol. 540, p. 152524, 2020.
http://doi.org/10.1016/j.jnucmat.2020.152524

[4] O.Y. Chernousenko, T.V. Nikulenkova, A.H. Nikulenkov, “Milestones of Implementation of Ageing Management for NPP Components,” Bull. NTU “KhPI”. Ser.: Power & Heat Eng. Proc. Equip., vol. 9(1181), pp. 85–89, 2016.
http://doi.org/10.20998/2078-774X.2016.09.12

[5] Z. He; H. Sun; L. Yu, “Video-based inspection system for nuclear fuel rod deformation measurement,” Nucl. Eng. Des., vol. 372, p. 110038, 2020.
http://doi.org/10.1016/j.nucengdes.2020.110038

[6] H.M. Wang et al., “Application of deep learning in visual inspection of nuclear components,” Ann. Nucl. Energy, vol. 145, p. 107540, 2020. http://doi.org/10.1016/j.anucene.2020.107540

[7] K. Maruyama; Touda; T. Kimura, “Radiation-induced volumetric expansion of concrete and its effect on microstructure,” Cem. Concr. Res., vol. 123, p. 105766, 2019. http://doi.org/10.1016/j.cemconres.2019.105766

[8] ICIC – International Committee on Irradiated Concrete. [Online]. Available: https://icic2023.ornl.gov [Accessed: Sep. 24, 2025].

[9] T. Motta; A. Couet; R.J. Comstock, “Corrosion of zirconium alloys used for nuclear fuel cladding,” Annu. Rev. Mater. Res., vol. 45, pp. 311–343, 2015. http://doi.org/10.1146/annurev-matsci-070214-020951

[10] Kim; S. Park; J. Lee, “Deep learning-based segmentation and classification of microstructural features in irradiated alloys,” J. Nucl. Mater., vol. 542, p. 152507, 2020. http://doi.org/10.1016/j.jnucmat.2020.152507

[11] G. Van Rossum; F.L. Drake, Python 3 Reference Manual, CreateSpace, 2009.

[12] M. Abadi et al., TensorFlow: Large-Scale Machine Learning on Heterogeneous Systems, 2015. arXiv:1603.04467

[13] K.M. Paaren et al., “Fuel Performance Analysis of FFTF MFF-3 and -5 Fuel Pins Using BISON with PIE Data,” Energies, vol. 16, no. 6, p. 2735, 2023. http://doi.org/10.3390/en16062735

[14] A. Leenaers et al., “Post-irradiation examination of AlFeNi cladded U_3Si_2 fuel plates irradiated under severe conditions,” J. Nucl. Mater., vol. 377, no. 1, pp. 152–162, 2008. http://doi.org/10.1016/j.jnucmat.2008.01.013

[15] A. Laufer, “Post Irradiation Examination of Fuel,” in Materials Under Extreme Conditions, Springer, 2023. https://doi.org/10.1007/978-981-99-0949-0_6

[16] P. Zhang; M.-Z. Ran, “Destructive Post-Irradiation Examination of Irradiated Fuel Rod,” Nucl. Instrum. Methods B,Jul.2005.[39. 113-116]

[17] J.-W. Cho; Y. Choi; K. Jeong; J.-C. Shin, “Measurement of nuclear fuel rod deformation using an image processing technique,” Nucl. Eng. Technol., vol. 43, no. 2, pp. 133–139, 2011. http://doi.org/10.5516/NET.2011.43.2.133

[18] F. Shadmehri; S.V. Hoa, “Digital Image Correlation Applications in Composite Automated Manufacturing, Inspection, and Testing,” Appl. Sci., vol. 9, no. 13, p. 2719, 2019. http://doi.org/10.3390/app9132719

[19] P. Murray; G. West; K. Law et al., “Automated in-core image generation from video to aid visual inspection of nuclear power plant cores,” Nucl. Eng. Des., vol. 300, pp. 57–66, 2016. http://doi.org/10.1016/j.nucengdes.2015.11.037

[20] M. Devereux; P. Murray; G. West; S. Buckley-Mellor; G. Cocks; C. Lynch; A. Fletcher, “Automated analysis of AGR fuel channel inspection videos,” presented at [Conf. 6th EDF-Energy Nuclear Graphite Conference], Kendal, UK, Oct. 2018. [Online].Available:[https://pure.strath.ac.uk/ws/portalfiles/portal/87986003/Devereux_etal_EDF_2018_Automated_analysis_of_AGR_fuel_channel_inspection.pdf] [Accessed: Sep. 24, 2025]

[21] D. Plašienka et al., “Measurement of nuclear fuel assembly’s bow from visual inspection’s video record,” Nucl. Eng. Technol., vol. 55, no. 4, pp. 1485–1494,2023. http://doi.org/10.1016/j.net.2022.12.033

[22] J. Knotek; J. Blažek; M. Kopeć, “Simulating Nuclear Fuel Inspections: Enhancing Reliability through Synthetic Data,” Nucl. Eng. Technol., vol. 57, no. 8, 2025. http://doi.org/10.1016/j.net.2025.103571

MAIN SPONSOR:

framatome

ORGANIZED BY:

50 ИЯИЯЕ

1972 INRNE

SUPPORTED BY:

Westinghouse

KOZLODUY NPP

Studsvik